2018

Preparation Of Active And Stable High-Surface Area Catalysts By Atomic Layer Deposition

Tzia Ming Onn
University of Pennsylvania, tziaming@gmail.com

Preparation Of Active And Stable High-Surface Area Catalysts By Atomic Layer Deposition

Abstract
Deactivation of catalytic functional oxides through the loss of surface area is a major concern. The conventional approach to maintain high-surface area of these materials is to incorporate the functional components onto a support which is less susceptible to sintering. Conventional impregnation tends to introduce large crystallites and often does not increase the surface area of the functional component. To address this issue, ALD was used in this work to engineer materials on the surface of interest.

ALD has been used to form uniform oxides in a layer-by-layer manner with excellent compositional control. However, since ALD was developed in the semi-conductor industry to produce relatively thick films on a flat surface, the design criteria are very different from what is required for catalytic applications. First, the rapid cycling with high-velocity carrier gases that are commonly used in semiconductor fabrications will create diffusion limitations in porous structures. Second, when carrier gases are used, most reagents pass through the reactor without being incorporated into the sample. This is prohibitively expensive for catalytic applications. In this thesis, a static ALD system which avoids these issues was developed for preparing catalysts in two primary areas: (a) high-surface area active supports with excellent thermal stability, and (b) stabilization of precious metals.

The first area involved fabricating thin films of Fe2O3, CeO2, CeZrO4, and LaFeO3 on porous Al2O3. These high-surface area films were shown to be uniform and they exhibited excellent thermal stability up to 1273 K when used as supports for Pd in methane and CO oxidation. With compositional control by ALD, CeZrO4 and LaFeO3, complex oxides would otherwise require complex synthesis or high temperature treatments, were easily fabricated at moderate conditions.

The second area involved stabilizing metal particles by thin films of LaFeO3 and ZrO2 prepared by ALD. Pd supported on LaFeO3 is of interests as it is the classical example of a “smart” catalyst capable of redispersing metal particles following redox cycling conditions. The LaFeO3 catalysts were shown to exhibit properties expect for smart catalysts. Overcoating thin films of ZrO2 on Pd to improve its thermal stability was also demonstrated.

Degree Type
Dissertation

Degree Name
Doctor of Philosophy (PhD)

Graduate Group
Chemical and Biomolecular Engineering

First Advisor
Raymond J. Gorte

Keywords
Atomic Layer Deposition, High-Surface Area Support, Methane Oxidation, Palladium Catalysts, Thermal Stability, Water Gas Shift Reaction

Subject Categories
Chemical Engineering

PREPARATION OF ACTIVE AND STABLE HIGH-SURFACE AREA CATALYSTS BY ATOMIC LAYER DEPOSITION

Tzia Ming Onn

A DISSERTATION

in Chemical and Biomolecular Engineering

Presented to the Faculties of the University of Pennsylvania

in Partial Fulfillment of the Requirements for the

Degree of Doctor of Philosophy

2018

Supervisor of Dissertation

_____

Raymond J. Gorte, Professor of Chemical and Biomolecular Engineering

Graduate Group Chairperson

_____

John C. Crocker, Professor of Chemical and Biomolecular Engineering

Dissertation Committee

John M. Vohs, Professor of Chemical and Biomolecular Engineering

Daeyeon Lee, Professor of Chemical and Biomolecular Engineering

Vivek Shenoy, Professor of Material Science and Engineering

PREPARATION OF ACTIVE AND STABLE

HIGH-SURFACE AREA CATALYSTS

BY ATOMIC LAYER DEPOSITION

DEDICATION

This work is dedicated to my family and friends.

Thank you for always being there to support me.

Special gratitude and a million thanks to Ray for his guidance and unconditional support.

ACKNOWLEDGMENT

My most sincere thanks to my thesis advisor and mentor, Ray, for his unconditional support, guidance, and encouragement throughout my years pursuing my Ph.D. No words can express how grateful I am. I want to acknowledge my thesis committee, Prof. John Vohs, Prof. Daeyeon Lee, and Prof. Vivek Shenoy for their support and guidance. Not forgetting my collaborators, George, Paolo, Shuyi, and Sheng, many thanks for your time and being there for discussions.

I would also like to thank all the students that I had the pleasure of working with during the past five years, in particular Xinyu Mao, Joonbaek Jang, Xia Ye, Meghavi, and Yu-Chieh. To my friends and colleagues, your presence and support made my experience at the University of Pennsylvania more enjoyable and more meaningful. I also wish to offer my sincere gratitude to the following:

- Lisandra for being an amazing teacher and being patient with me while guiding me through my first few months in the lab.
- Jyo Lyn, Brad, Chen and Sang for upholding our tradition to get meals in Sky Café every semester.
- Yu-Hao, Cong Wang, Chao Lin, Matteo Monai, and Morteza for taking your time and being there for discussions and company when working late nights or grabbing meals after work.

- Shankar, Amy and Iva for keeping me grounded and lending your support. Thanks for your company for meals in Sitar and other places.
- Penn Badminton Club for all the weekend competitions and wonderful memories.

I want to acknowledge the financial support for this project, which was provided by the U.S. Department of Energy, Office of Basic Energy Sciences (DE-FG02-13ER16380).

Finally, my deepest gratitude must go to my family. This thesis is dedicated to them. Without their support and love, I would not have made it here.

ABSTRACT

PREPARATION OF ACTIVE AND STABLE HIGH-SURFACE AREA CATALYSTS BY ATOMIC LAYER DEPOSITION

Tzia Ming Onn

Raymond J. Gorte

Deactivation of catalytic functional oxides through the loss of surface area is a major concern. The conventional approach to maintain high-surface area of these materials is to incorporate the functional components onto a support which is less susceptible to sintering. Conventional impregnation tends to introduce large crystallites and often does not increase the surface area of the functional component. To address this issue, ALD was used in this work to engineer materials on the surface of interest.

ALD has been used to form uniform oxides in a layer-by-layer manner with excellent compositional control. However, since ALD was developed in the semi-conductor industry to produce relatively thick films on a flat surface, the design criteria are very different from what is required for catalytic applications. First, the rapid cycling with

high-velocity carrier gases that are commonly used in semiconductor fabrications will create diffusion limitations in porous structures. Second, when carrier gases are used, most reagents pass through the reactor without being incorporated into the sample. This is prohibitively expensive for catalytic applications. In this thesis, a static ALD system which avoids these issues was developed for preparing catalysts in two primary areas: (a) high-surface area active supports with excellent thermal stability, and (b) stabilization of precious metals.

The first area involved fabricating thin films of Fe_2O_3, CeO_2, $CeZrO_4$, and $LaFeO_3$ on porous Al_2O_3. These high-surface area films were shown to be uniform and they exhibited excellent thermal stability up to 1273 K when used as supports for Pd in methane and CO oxidation. With compositional control by ALD, $CeZrO_4$ and $LaFeO_3$, complex oxides would otherwise require complex synthesis or high temperature treatments, were easily fabricated at moderate conditions.

The second area involved stabilizing metal particles by thin films of $LaFeO_3$ and ZrO_2 prepared by ALD. Pd supported on $LaFeO_3$ is of interests as it is the classical example of a "smart" catalyst capable of redispersing metal particles following redox cycling conditions. The $LaFeO_3$ catalysts were shown to exhibit properties expect for smart catalysts. Overcoating thin films of ZrO_2 on Pd to improve its thermal stability was also demonstrated.

TABLE OF CONTENTS

LIST OF TABLES

LIST OF ILLUSTRATIONS

CHAPTER 1. INTRODUCTION

1.1 Motivation

The use of catalysts in industrial processes is widespread, and its global economic contribution is estimated to be worth around USD 30 trillion, as of 2017 [1]. Because the reaction rates and selectivities over a given catalyst can dramatically affect the economics and energy efficiency of the catalytic process, there has been a continuing research effort over the years to come up with increasingly better materials. For many of these processes, the catalysts used are heterogeneous complex solids. They are typically multicomponent, consisting of catalytically active components and promoters deposited onto a support material that provides high surface areas. The catalytically active components usually consist of more than one component, such as in the case of alloy or bimetallic compound. The role of the promoters, on the other hand, varies immensely depending on the type of reactions.

For example, promoters such as ceria (CeO_2) can enhance oxygen storage capacity (OSC) in automotive, three-way catalysts [2-5] due to its ability to undergo cycles of reduction and oxidation. Another example is the enhancement of the thermal stability of active components such as the case of lanthanum ferrite ($LaFeO_3$) and precious metals as ‘smart catalysts’ in automotive applications [6-8]. When these functional oxides are added by conventional impregnation of metal salt solution to supports such as alumina and zirconia, they tend to form larger crystallites so that the actual active surface area may not be greatly enhanced, and more importantly, it introduces difficulties in that the supported metals may not be in close contact with these promoters.

Ceria is a critical component in many commercial catalysts, as demonstrated in a recent comprehensive review [9]. Two important examples include the use of ceria-based materials as oxidation catalysts in Diesel particulate filters [10] and the use of ceria in the form of ceria-zirconia solid-solutions as Oxygen-Storage Capacitors (OSC) in automotive three-way catalysts [2-5]. The critical property of ceria that makes it useful in these and other catalytic applications is the relative ease with which it undergoes facile oxidation and reduction. This, together with the fact that reduced ceria can be oxidized by steam or CO_2 [11] and then transfer oxygen to transition metals such as Pd with which it is in contact make it a promoter of hydrocarbon oxidation [12,13], water-gas-shift (WGS) reaction [14,15], steam reforming [16,17], and more.

Unfortunately, the stability of ceria is a problem [18]. Under harsh redox cycling conditions, ceria sinters and loses significant surface area, which subsequently leads to a rapid reduction to the oxygen storage and release properties. Hydrothermal aging and the resulting increase in ceria crystallinity has been shown to change the thermodynamics of CeO_2 reduction, increasing the magnitude of the heat of oxidation by as much as 50% [19]. In three-way catalysts, the redox properties of ceria are stabilized by addition of zirconia to form ceria-zirconia solid solution. They maintain their reducibility properties even after harsh redox cycling although it should be noted that after standard operations in a vehicle, ceria-zirconia mixed oxides typically have very low specific surface areas of only 2 m^2/g [20].

Another example where promoters are used to enhance catalytic properties is the so-called “smart catalysts” developed by Daihatsu [6-8]. Aging of Pd-based catalysts is

primarily due to loss of Pd surface area via metallic sintering, which becomes severe above the PdO decomposition temperature. Researchers at Daihatsu reported that Pd can become part of the perovskite under oxidizing conditions (e.g. $LaFe_{0.95}Pd_{0.05}O_3$), then "ex-solve" out of the bulk under reducing conditions, allowing the metal to be redispersed. Since the time of their reports, the ex-solution process has been observed with many other metals and other perovskites [21-23].

Unfortunately, the redispersion process appears to have limited effectiveness in practical applications. Most perovskite-structured oxides have much lower specific surface areas of around 5 m^2/g compared to the oxides most commonly used as catalyst supports. The low surface area comes from the fact that the perovskites exist as relatively large crystallites, particularly after exposure to the high temperatures needed to form the perovskite structure or those experienced in use. This has important consequences. First, there is limited area available for the dispersed metal particles at the surface of the perovskite since the surface area of the metal catalyst cannot be higher than the area of the support. Second, the diffusion of metal cations within the perovskite lattice is slow and the diffusion distance will be much less than the crystallite size.

To address these issues while taking advantage of the promotional effects between the promoters and the active components, it is therefore critical to engineer catalysts on an atomic level.

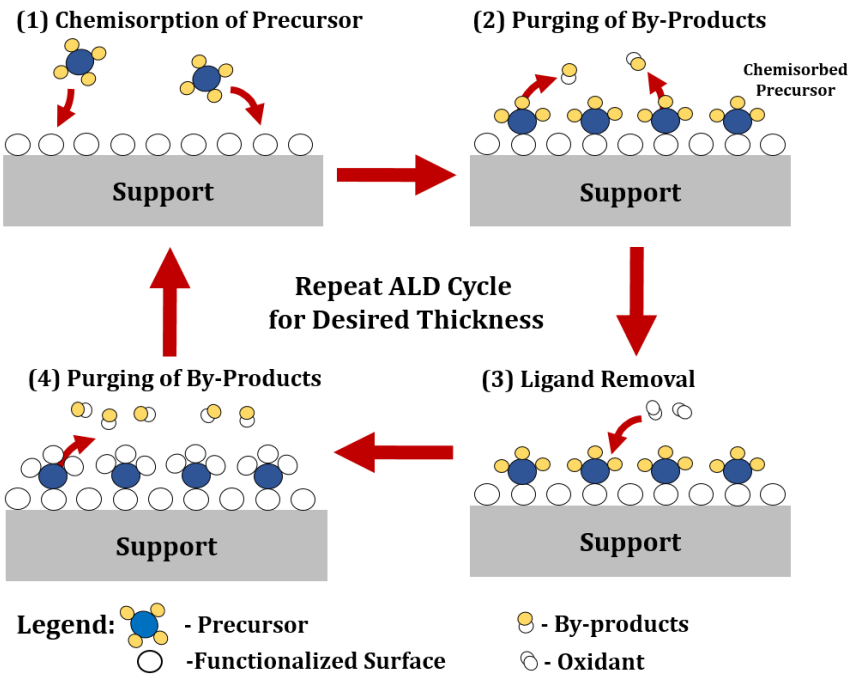

FIG. 1.1. Schematic of one ALD cycle. (a) Chemisorption of precursor molecules on the surface, (b) Purging of the unreacted precursor molecules and reacted by-products, (c) introduction of ligand removal reactants, which react with the chemisorbed precursor molecules to regenerate sites for the next ALD cycle, and (d) purging of the excess reactants and the by-products.

1.2 Atomic Layer Deposition

As of today, there are various nanotechnology tools that have allowed materials to be designed to be in close proximity to take advantage of promotional effects. One of the most interesting tools is Atomic Layer Deposition (ALD). ALD is a vapor deposition technique, commonly used in the semi-conductor industry, that relies on a cycle of steps to prepare thin films in a layer-by-layer manner. The general principles of ALD is illustrated in Figure 1.1. The surface being modified is first allowed to react with a gaseous organometallic molecule, after which the ligands of the adsorbed molecular precursor are removed in a separate step.

The presence of the ligands on the adsorbed precursors prevent additional reaction on the surface and limit the growth of the film to no more than one monolayer for each cycle. This is followed by the ligand removal step, and the cycle of precursor exposure and ligand removal can be repeated to grow films of any desired thicknesses. This layer-by-layer addition of materials with a sub-monolayer growth provides excellent control in preparing nanocomposite with well-defined structure and composition. Another advantage of ALD is that the precursors are available for much of the periodic table owing to its development in the semiconductor industry. However, there are serious issues with the current designs and approaches as they are largely catered to semiconductors and may not be suitable for preparing catalyst samples. This will be discussed extensively below.

1.3 Issues of Conventional ALD Approach for Catalyst Preparation

The designs and approaches of ALD over the past decades have been largely developed for the semiconductor industry in order to grow films on flat samples with low surface areas of around 1 m^2/g [24,25]. Diffusion of the precursor molecules onto the surface occurs rapidly for the desired film thickness usually around 2 nm to 20 nm [24,25]. There may be pillared structures on the surface in some cases; but the aspect ratio of these structures, the ratio of the channel depth to width, is rarely greater than 100. For an ALD film growth rate of 0.04 nm/cycle, even a 10-nm film would require 250 cycles. To make this process cost effective to meet the demands of the fast pace semi-conductor industry, ALD equipment is designed to carry out each step as rapidly as possible. This is accomplished using a flow ALD reactor system, with the precursors and ligand-removal

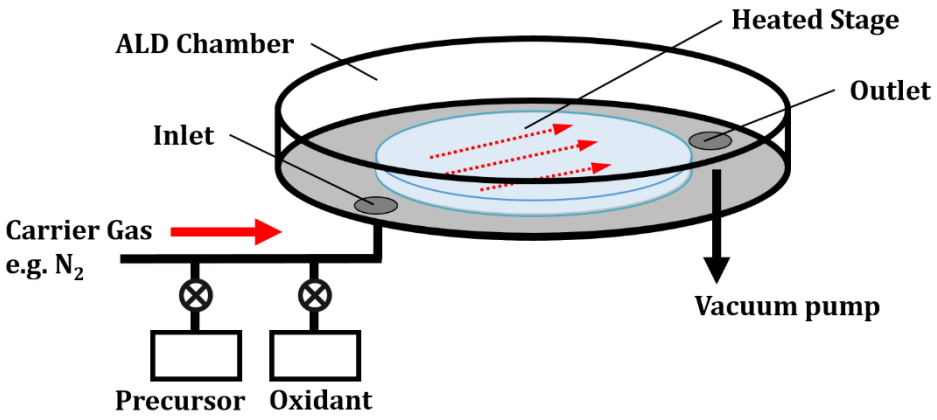

FIG. 1.2. Simplified schematic of a typical research-grade viscous flow ALD reactor designed for coating flat samples (e.g. Si wafers). The red dotted arrows indicate the direction of gas flow across the sample.

reagents being transported into and out of the deposition chamber via a carrier gas (Figure 1.2). The flow rates of the carrier gas are around 100 to 200 mL/min, corresponding to linear gas velocities of 2.5 to 10 m/s across the substrate [26,27]. The precursor and ligand-removal reagents are introduced into the carrier stream as short pulses, typically of 0.5 sec duration, and passed over the sample by convection. Due to the high flow velocities, back mixing is negligible. Each ALD cycle typically lasts 2 s so the total length of time to deposit 10-nm film would take approximately 500 s.

Unlike flat samples in semiconductor devices, the film thickness deposited into the pore structures has a major impact on the specific surface area of the catalysts. Films around 10-nm would result in nanopores being clogged and a significant decrease in specific surface area simply due to the addition of materials (10-nm film on a 100 m^2/g equates to ~400 wt.%. gain of material assuming the film is uniform and dense with 5 g/cm^3). In order to determine a relevant film thickness for application in catalysis, we will first consider the

deposition of 1-nm film of material on a 1-gram Al_2O_3 support with BET surface area of 200 m^2/g and a reasonable 20 nm average pore size. Assuming that the material deposited has a density of 5 g/cm^3 (e.g. Fe_2O_3 has a density of 5.24 g/cm^3) and it uniformly coats the support, the 1-nm film corresponds to a weight gain of approximately 50 wt.% of the added material. Even if the pore sizes were not affected by the added material, the specific surface area (surface area/mass of material) would be decreased by half. Although this calculated change in specific surface area ($100 m^2/g$) is still acceptable, it is critical that the thickness of the film deposited on the porous support be limited to 0.3 to 1.5 nm.

While this flow ALD reactor allows for rapid cycling, it has several limitations for preparation of thin films on catalysts materials. The first issue is associated with the rapid cycling of materials in a flow ALD reactor. In catalyst preparation, it is important not to lose a significant amount of the precursor materials. This is obvious based on the above calculation of the film weight loading if one intends to prepare 1-2 nm of material on a high-surface area support. With a carrier gas, most of the reagents may pass through the reactor without fully adsorbing into the porous sample. This leads to wastage of precious precursor molecules although for the semiconductor industry, the cost of the precursors may not be an issue as the cost of production is steep. Since the main costs of the precursor molecules stems from the high cost of the organic ligands, it is necessary to make full use of the precursor in the sample itself for catalyst preparation.

The second issue is the diffusion limitation of precursor molecules into the catalysts. Conventional catalysts comprise of catalytically active components deposited on porous powders, such as alumina, silica, zeolites, etc., which has surface areas of around

100 m^2/g to 500 m^2/g. The aspect ratio of these pores is significantly larger than that found with even the deepest channels in semiconductor devices. For example, even a thin catalyst bed would likely be 100 μm thick and have pores that are 50 nm in diameter, resulting in an aspect ratio of 2000. The use of a carrier gas presents severe diffusion limitations into the high-aspect-ratio pore structures. Diffusion of the precursor molecules and ligand-removal reagents into and out of long pores will be challenging, and it may be further hindered by the formation of by-products as the reagents react with the sample surface along the porous network. This can lead to gradients in the film deposition along the support surface, even when surface reactions are rapid [28,29].

To address the issues, a reactor design or process worth considering is that of an ALD static system, which utilizes precursor materials with minimal waste and avoids issues related to diffusion limitations. The process for a static ALD system differs from a flow reactor system in that the sample inside the reactor is exposed to non-flowing (i.e. static precursors). Inert gases can be introduced to clean the system after exposure to the reactants to remove any sticky by-products but they must be vacuum evacuated following completion. For porous samples, the use of a static ALD system addresses the issues associated with diffusion of the precursor molecules into the pores by avoiding the use of a carrier gas and increasing the static precursor exposure time. This approach will be discussed extensively in the following section.

1.4 Considerations of ALD Principles in Catalyst Preparation

In principle, a complete ALD cycle consists of four distinct steps: (1) adsorption of the gaseous precursor onto the surface of the substrate, (2) purging the excess precursor and its by-products from the sample, (3) introduction of a gaseous reactant to remove ligands and to regenerate sites, and (4) purging out the excess reactants and its by-products. These steps have been illustrated in a pore structure in Figure 1.3 and are most thoroughly documented for the Al_2O_3 ALD system, using trimethyl aluminum (TMA) as the precursor and water vapor as the reagent for removing the ligands [30]. The TMA-water process is often regarded as the ideal ALD process, since the surface reactions shown in Figure 1.1 are self-terminating, both TMA and water are highly reactive, both TMA and water have high vapor pressures at deposition conditions (i.e. there is little tendency for them to form physisorbed, condensed films on the surface.), and the gaseous reaction product (methane) is inert [30]. Other ALD systems may rely on different precursor chemistries as they have different ligands such as halides, β-diketonates, alkyls, and cyclopentadienyls bound to the metal atom [30,31]. While the precise reaction mechanisms are specific to the respective individual system and the properties of the substrate to be coated, the general principles governing the deposition are often considered to be similar [30,32]. The individual steps of the ALD process will be discussed below in consideration of depositing thin films on porous samples with illustration of ALD in a pore structure as shown in Figure 1.3.

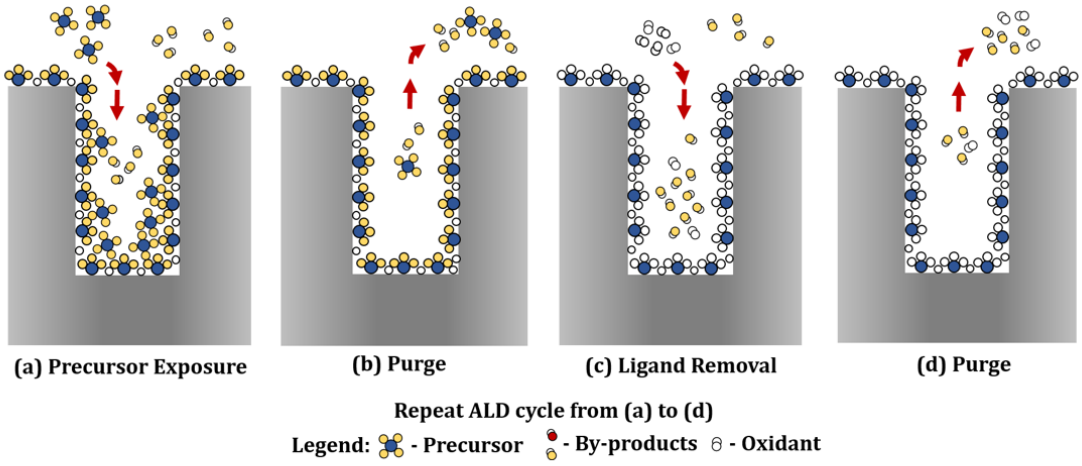

FIG. 1.3. Schematic of one ALD cycle in a pore structure. (a) Exposure of precursor molecules into the pore structure and adsorption onto the surface, (b) complete purging of the gaseous species from the pore structure, (c) introduction of ligand removal reactants, which react with the chemisorbed precursor molecules to regenerate sites for the next ALD cycle, and (d) purging of the gaseous species.

1.4.1 Adsorption of the gaseous precursor onto the surface of the substrate

The first step, the exposure of the vapor-phase precursor to the surface of the substrate, requires that the precursor molecules adsorb onto the substrate. Although the adsorption step preferably involves loss of a ligand and formation of a chemical bond, physically adsorbed species may be acceptable for some ALD systems on flat surfaces so long as the single-layer physisorbed species interacts with the surface more strongly than the precursor molecules interact with a condensed film [33]. The advantage to using physisorbed species is that the coverage of adsorbed precursors will be higher, leading to a higher growth rate [33]. This is acceptable in the semiconductor industry to keep up with the cost of production rate. Uniformity based on physisorbed precursors can be achieved using a flow ALD reactor system on flat samples with short times between pulses, typically 0.1 s; however, for ALD on porous materials, these conditions leading to physisorbed

monolayers and multilayers will likely lead to uneven growth of materials in different parts of the surface.

When ALD is carried out on flat substrates, such as silicon wafers, the use of a carrier gas allows the transport of precursors and reactants to be delivered rapidly from the gas stream onto the substrate surface. It has shown success in coating high-aspect ratio structures with straight pores and uniform films have been successfully demonstrated on the surface of trenches with aspect ratios of ~100 etched into silicon [34]. However, the use of a carrier gas poses a serious problem when performing ALD on high-surface-area catalyst support. The rapid convective transport of precursors in the carrier gas flow strongly impede the diffusion of species into the porous samples. This leads to several problems. First, the outermost surface of the sample bed will be exposed to precursor fluxes several orders of magnitude larger than interior surfaces [35]. Without considering the convective transport in this scenario, the precursor molecules have to diffuse past the already-saturated part near the top of the pores before they can reach the unsaturated, deeper parts of the sample. In a realistic ALD process, diffusion of precursor into the pores could also be hindered by counter diffusion of the carrier gas and the presence of products formed by chemisorption. In order to achieve precursor penetration throughout the high surface area material, longer exposure times or multiple exposures are necessary. In one study, precursor exposure times of almost 2 hours were required to saturate just 0.2 grams of SiO_2 powder with a specific surface area of 506 m^2/g in a fixed-bed reactor. The entire ALD cycle (consisting of the precursor exposure step, the first purge step, the oxidant exposure step, and the second purge step) lasted 8 hours [36].

ALD can be made practical for depositing materials on large amounts of porous samples with the right approach. Using concepts from Kinetic Theory of Gases, Longrie *et al*. described the adsorption of the precursors onto a bed of particles for a static ALD system [29]. They considered the flux of precursor molecules through the top surface of a bed of particles and calculated the time required to saturate the bed. Their analysis showed that the time required to saturate the surface was given by Equation 1:

$$\frac{t}{kT} = \frac{3}{4}\frac{\pi S}{r_c^2\,\Delta P}\sqrt{\frac{M}{2\pi RT}}\,l_c^2 \qquad (\textbf{Equation 1.1})$$

In this equation, r_c is the radius of the particles or pores, S is the number of sites per surface area, l_c is the length (or depth) of the bed, M is the molecular weight of the precursor, and ΔP is the dosing pressure of the precursor. This analysis takes into account that, during precursor exposure, the gas must adsorb from the top of the bed, saturate those particles first, and can only then progress deeper into the pores. In their analysis, Longrie, *et al*. point out that the adsorption time could be hundreds of hours if the experimental parameters are not chosen properly. Fortunately, the equation provides criteria for minimizing the required exposure times. Especially important, the diffusion length needs to be kept short. This can be accomplished by forming the powders into thin wafers rather than having a free-standing bed of powder. Alternatively, Longrie *et al.* has shown in a different publication that ALD can be performed on high-surface area materials using a home-built static ALD system [35]. Increasing the pressure of the precursor also can significantly decrease the required

exposure time. In some cases, development of new, highly volatile precursors may be necessary [37].

In addition to affecting the exposure time, high-surface-area samples also require considerably larger amounts of the precursor. Required precursor amounts for a single ALD exposure can be estimated by assuming a 100 m^2/g powder with an adsorption site density of ~10^{18} sites/m^2 [38]. To coat 1 gram of such powder, the amount of precursor required for a uniform monolayer coverage is ~10^{-4} moles (corresponding to 14 mg TMA or 87 mg $Ce(TMHD)_4$). This is a nontrivial amount especially when we consider the wastage of materials from a flow ALD system.

1.4.2 Purging the excess precursor and reaction by-products from the sample

After the exposure step, excess precursor molecules and by-products from the substrate must be removed by purging. This is considered the longest step in the ALD cycle [26,27]. To increase the production rate of wafers in the semiconductor industry, flow ALD systems with carrier gas are used to flush gas-phase and physisorbed molecules from the sample [26]. This is not trivial for a porous sample since the excess precursor molecules and by-products in the pores must diffuse to the exterior of the pore while in the presence of the carrier gas molecules. Diffusion of the excess precursors out of a porous sample will be described by similar processes and a similar set of equations as outlined above for precursor exposure, but with several additional complications.

First, for very small pores, the saturation pressure of the precursor could be lowered due to capillarity which leads to condensation locally in the sample. This reduces the

driving force for diffusion of the precursor out of the bed. That driving force in Equation 1) is ΔP, the difference between the partial pressure in the pores and the partial pressure in the carrier-gas purge. A second additional complication is that desorption rates in porous materials are much slower than rates from flat samples when the desorbing species can re-adsorb on other parts of the sample. Even when purging using an infinitely high carrier-gas flow rate, the effective desorption rate from the pores will be given by Equation 2 [39]:

$$k_{\text{eff}} = \frac{\pi^2 D}{S k_a l_c^2} k_{\text{d}} \quad (\textbf{Equation 1.2})$$

In this equation, D is the diffusivity of the precursor, S is again the surface area of the substrate, and k_a is the adsorption rate constant. In the derivation of this equation, which was developed to describe desorption from porous materials into a vacuum, it was shown that the ratio of the effective desorption rate constant, k_{eff}, to the intrinsic desorption rate constant, k_{d}, can easily be less than 10^{-6}, implying that purging a porous sample of excess precursor molecules can be slow.

Obviously, when the purging step is incomplete, physisorbed precursor molecules may remain within the pore. Introducing the next reactant will lead to reaction of these condensed species, one consequence being the formation of non-uniform films. Reaction of a condensed phase of the precursor can also lead to films that are not conformal or films that may be porous.

1.4.3 Gaseous reactant to remove ligands and to regenerate sites

After purging, the active sites on the surface of the substrate must be regenerated through the removal of the ligands on the chemisorbed precursor molecules. There are standard methods for removing the ligands that work quite well for flat samples, usually through substitution of the ligands or complete combustion [31]. For example, we have already discussed reaction of the adsorbed precursor for TMA with H_2O to remove the remaining methyl groups. For combustion of the ligands, it is common to use oxidizers such as H_2O_2 or O_3 [30]. However, ligand removal on porous samples is considerably more difficult, in part because there are more precursor ligands to remove. For many ligands, O_2 is not an effective oxidizer at ALD temperatures (typically between 423 to 523 K).

For O_3 and H_2O_2, transport issues are often a problem. While the principles behind transport of O_3 and H_2O_2 are similar to those discussed earlier for precursor adsorption step [35]; there is the added issue that these reactive species have limited lifetimes and are typically present in small concentrations. For example, the half-life of ozone in air at 523 K is only 1.5 s and is much lower in the presence of catalytic materials [40]. If time required for the reactant to diffuse into the sample is long, this is obviously a problem. The maximum concentration of ozone reported in a typical industrial ozone generator is also only ~20% under pure O_2 flow. This leads to issues of dilution and additional diffusion limitations. In general, H_2O is not an effective oxidant for complete removal of ligands as evident in systems such as TMA/H_2O, tris(dimethylamido)-tin/H_2O, and diethylzinc/H_2O. Incomplete removal of the ligands will almost certainly influence the growth behavior for subsequent ALD cycles [41].

Two interesting alternatives for ALD in porous materials are NO_2 [42] and oxygen plasmas [43,44]. NO_2 is a strong oxidant that can be produced in high concentrations, and this technology has been used by Johnson Matthey to perform low-temperature oxidation of soot in automotive application that would normally require oxidation at 873 K [45]. NO_2 has been successfully demonstrated to remove ligands from a chemisorbed precursor, $La(thd)_3$ (thd = 2,2,6,6-Tetramethyl- 3,5-heptanedionate), on Al_2O_3 at less than 573 K [42]. O_2 plasmas are also good oxidizers and can be generated *in-situ* using a radio-frequency generator. Partial removal of coke from zeolite catalysts at low temperatures was demonstrated already in the 1980s using an oxygen plasma [46]. Recent advances in the technique have seen oxygen plasmas generated at atmospheric pressures, with complete removal of coke from Pt-Sn/Al_2O_3 catalysts and H-ZSM-5 catalysts at near room temperature [43,44].

1.4.4 Purging the excess reactants and reaction by-products.

The ALD cycle is completed with the purging of the by-products and the excess ligand removal reactants. Since each ALD cycle is irreversible and involves reactions at saturation, the amount of material deposited per area should be the same on flat or complex substrates, provided that sufficient precursors chemisorb on the entirety of the surface, complete purging is achieved, and the ligands are successfully removed regardless of reactor design.

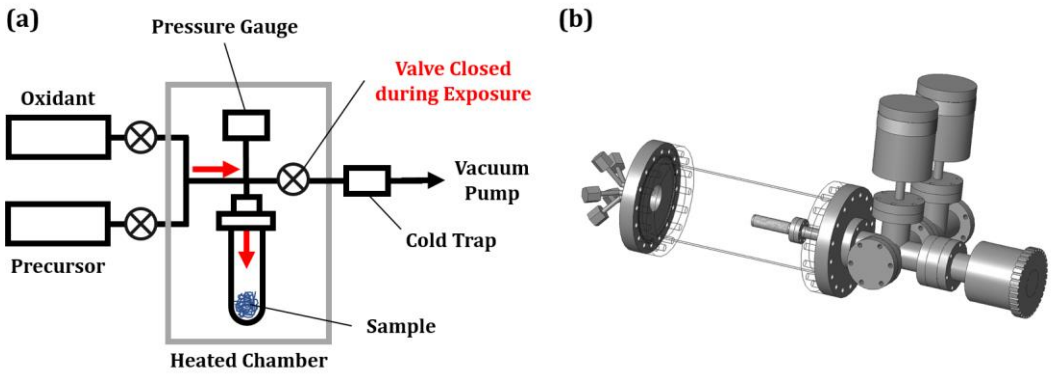

FIG. 1.4. Schematic diagram of (a) a static ALD setup and (b) a rotary reactor ALD setup [29], designed for static reactant exposure without a carrier gas.

1.5 ALD Reactor Design for Catalyst Preparation

The principles behind ALD are the same for flat samples as well as catalyst samples. However, the use of a carrier gas as depicted in Figure 1.2 is not suitable for depositing materials on high-surface area samples. Therefore, the *static reactor*, shown schematically in Figure 1.4(a), is the setup worth considering. The term "static" is used here to refer to the fact that the sample inside the reactor is exposed to non-flowing (i.e. static) precursors without a carrier gas. The reactor itself can be rotating or the particles inside the reactor can be agitated in various other ways [29,47,48]. To date, the most notable static ALD reactor system reported is the rotary ALD reactor system shown in Figure 1.4(b) [29]. It has been successful in the ALD of W and Al_2O_3 on large batches of porous samples [29,47,48] although simple static reactors without any moving parts have also successfully been used to coat samples [36].

In a static reactor, the sample is held in a sealed vessel that can be vacuum evacuated to a baseline pressure of 0.001 Torr without the presence of a carrier gas. This

avoids any diffusion issues discussed earlier. Exposure to the precursor is performed in the same way that any adsorption would be performed and the purge cycles would be performed by simply evacuating the sample. A purge gas may still be used in between precursor exposure steps, although it is not required. Compared to flow reactors, such as the one shown in Figure 1.2, where a significant portion of the precursor passes the substrate unreacted, making the coating of samples requiring large reactant exposures impractical, precursor utilization in static reactors can reach very high levels.

1.6 Objective: Catalyst Design by ALD

The catalytic properties of metal-based heterogeneous catalysts rely on interactions between precious metals and oxides, supported on porous powders with surface areas around 100 m^2/g or more. With ALD, strategies for better catalyst design to maximize the contact between the two components can be easily achieved. This thesis will focus on two important areas: (a) preparation of high-surface area films with excellent thermal stability and the (b) stabilization of precious metals and metal oxides by thin films prepared by ALD. The motivation for the individual work will be discussed extensively in their respective chapters but the general goal is to prevent sintering or agglomeration of materials due to high temperature operations and to the effects of poisons. Obviously, this is a serious issue as the cost of precious metals are in the order of USD 50,000 per kilogram (as of 2017), and the availability of these precious metals and rare-earths are becoming increasingly limited. This thesis will show that it is possible to design and prepare catalytically active materials with excellent thermal stability up to 1173 K by ALD.

1.6.1 High-Surface-Area, Functional Oxides

Many functional oxides, such as ceria-zirconia mixed oxides and lanthanum ferrite perovskites, typically have surface areas of around 5 m^2/g following preparation or operation conditions [6,20]. It is desirable to maximize the surface area in order to improve catalytic performance, while providing a better stability of the functional oxide. These two conditions are commonly fulfilled by dispersing the functional oxide on large surface area inert support, typically through impregnation methods. However, the conventional wet impregnation method disperses the oxides as large crystallites, partially covering the inert support. ALD can circumvent this problem by uniformly depositing a thin film of the oxide of interest onto the support. An important key to this strategy is the growth rate of the film on a sub monolayer basis per ALD cycle, which allows thickness of the film to be precisely controlled. As discussed earlier, practical applications require a thickness of 1-2 nm to ensure reasonable specific surface area for catalytic applications. Another key component is the thermal stability of these films. Materials such as CeO_2 and Fe_2O_3 prepared by ALD have been widely studied on flat substrates, and these film structures have been shown to withstand calcination in air up to 1073 K although the reason behind their improved stability remains unclear. Therefore, this strategy of preparing high-surface area metal oxides will be pursued, and to the best of our knowledge, there are no literatures available that have investigated the preparation of materials via this route. Oxides such as Fe_2O_3, CeO_2, $CeZrO_4$ mixed oxides and $LaFeO_3$ perovskites deposited by ALD on porous Al_2O_3-based supports will be investigated.

1.6.2 Stabilization of Precious Metals and Metal Oxides by ALD

Coarsening of precious metals in high temperature applications is a major concern. The concept of self-regenerating or "smart" catalysts was first developed by Daihatsu to mitigate this problem. Their process involves redispersing large Pd particles by incorporating them into the $LaFeO_3$ support under oxidizing conditions and then exsolving them as small metal particles under reducing conditions. Unfortunately, the redispersion process does not appear to work in practice because the surface areas of the perovskite supports are too low and the diffusion lengths for the metal ions within the bulk perovskite too short. One strategy to address this issue is the use of ALD to prepare Pd supported on thin films of $LaFeO_3$ to improve the diffusion kinetics of the Pd.

ALD can also be used to stabilize metal particles by forming a metal oxide around the metal particles to prevent sintering. Similar strategies have been reported, such as a layer-by-layer solution-based approach and core-shell approach to stabilize metal particles [49,50], but ALD seems to have the advantage due to its versatility and better control with many similar studies having been reported [31]. A noteworthy example is the use of Al_2O_3 thin film to stabilize Pd particles and prevent coking though it is important to note that Al_2O_3 is an inert oxide [51]. It is critical that the coverage of the metal nanoparticles with thin layers of oxides must prevent sintering while not compromising the accessibility of the active site. This strategy will be used to investigate the thermal stability of Pd particles after ZrO_2 thin film is deposited by ALD over the metal particles to form a semi 'core-shell' structure. An extension to this work is to investigate the effects of ZrO_2 film over oxide supports such as CeO_2. CeO_2 loses surface areas after harsh redox cycling conditions,

and surface ceria is sensitive to poisoning by SO_2 and CO. Thin film of ZrO_2 will be used to coat the surface of CeO_2 to improve its thermal stability and resistance to surface poisoning.

1.7 References

1. Ma, Z.; Zaera, F., *Encyclopedia of Inorganic and Bioinorganic Chemistry* **2014**.

2. Di Monte, R.; Kašpar, J., *Top. Catal.* **2004,** *28*, 47-57.

3. Morikawa, A.; Suzuki, T.; Kanazawa, T.; Kikuta, K.; Suda, A.; Shinjo, H., *Appl. Catal. B.* **2008,** *78*, 210-221.

4. Gorte, R. J., *AIChE J.* **2010,** *56*, 1126-1135.

5. Gandhi H, Graham GW, McCabe RW., *J Catal.* 2003, 216, 433-442.

6. Nishihata, Y.; Mizuki, J.; Akao, T.; Tanaka, H.; Uenishi, M.; Kimura, M.; Okamoto, T.; Hamada, N., *Nature* **2002,** *418*, 164-167.

7. Tanaka, H. *Catal. Surv. Asia* **2005,** *9*, 63-74.

8. Tanaka, H.; Uenishi, M.; Taniguchi, M.; Tan, I.; Narita, K.; Kimura, M.; Kaneko, K.; Nishihata, Y.; Mizuki, J. I. *Catal. Today* **2006,** *117*, 321-328.

9. Montini, T.; Melchionna, M.; Monai, M.; Fornasiero, P., *Chemical Rev.* **2016,** *116*, 5987-6041.

10. Fino, D.; Bensaid, S.; Piumetti, M.; Russo, N., *Appl. Catal. A.* **2016,** *509*, 75-96.

11. Sharma, S.; Hilaire, S.; Vohs, J.; Gorte, R.; Jen, H.-W., *J. Catal.* **2000,** *190*, 199-204.

12. Heck, R. M.; Farrauto, R. J., *Appl. Catal. A.* **2001,** *221*, 443-457.4

13. Bueno-Lopez, A.; Krishna, K.; Makkee, M.; Moulijn, J. A., *Catal. Lett.* **2005,** *99*, 203-205.

14. Bunluesin, T.; Gorte, R.; Graham, G., *Appl. Catal. B.* **1998,** *15*, 107-114.

15. Hilaire, S.; Wang, X.; Luo, T.; Gorte, R.; Wagner, J., *Appl. Catal. A.* **2001,** *215*, 271-278.

16. Wang, X.; Gorte, R., *Appl. Catal. A.* **2002,** *224*, 209-218.

17. Duarte, R.; Safonova, O.; Krumeich, F.; Makosch, M.; van Bokhoven, J. A., *ACS Catal.* **2013,** *3*, 1956-1964.

18. Trovarelli, A., *Catalysis by ceria and related materials*. *World Sci.*: 2002; Vol. 2.

19. Zhou, G.; Shah, P. R.; Montini, T.; Fornasiero, P.; Gorte, R. J., *Surf. Sci.* **2007,** *601*, 2512-2519.

20. He, B. J.-J.; Wang, C.-X.; Zheng, T.-T.; Zhao, Y.-K., *Johns. Matthey Technol. Rev.* **2016,** *60*, 196-203.

21. Adijanto, L.; Padmanabhan, V. B.; Küngas, R.; Gorte, R. J.; Vohs, J. M. *J. Mater. Chem.* **2012,** *22*, 11396-11402.

22. Tian, C.; Zhu, X.; Abney, C. W.; Liu, X.; Foo, G. S.; Wu, Z.; Li, M.; Meyer III, H. M.; Brown, S.; Mahurin, S. M. *ACS Catal.* **2017,** *7*, 3388-3393.

23. Kwon, O.; Sengodan, S.; Kim, K.; Kim, G.; Jeong, H. Y.; Shin, J.; Ju, Y.-W.; Han, J. W.; Kim, G. *Nat. Commun.* **2017,** *8*, ncomms15967.

24. Haukka, S., *ECS Trans.* **2007,** *3*, 15-26

25. Raaijmakers, I. J., *ECS Trans.* **2011,** *41*, 3-17.

26. Elam, J.; Groner, M.; George, S., *Rev. Sci. Instrum.* **2002,** *73*, 2981-2987.

27. Elers, K. E.; Blomberg, T.; Peussa, M.; Aitchison, B.; Haukka, S.; Marcus, S., *Chem. Vap. Depos.* **2006,** *12*, 13-24.

28. Elam, J.; Routkevitch, D.; Mardilovich, P.; George, S., *Chem. Mater. 2003***,** 15, 3507-3517.

29. Longrie, D.; Deduytsche, D.; Detavernier, C., *J. of Vac. Sci. & Technol. A: Vac. Surf. and Film***. 2014,** *32*, 010802.

30. Puurunen, R. L., *J. Appl. Phys*. **2005,** *97*, 9.

31. Miikkulainen, V.; Leskelä, M.; Ritala, M.; Puurunen, R. L., *J. Appl. Phys* **2013,** *113*, 2.

32. Haukka, S.; Kytökivi, A.; Lakomaa, E.; Lehtovirta, U.; Lindblad, M.; Lujala, V.; Suntola, T., *Stud. Surf. Sci. Catal.* **1995,** *91*, 957-966.

33. Ylilammi, M., *Thin Solid Films* **1996,** *279*, 124-130

34. Schindler, P.; Logar, M.; Provine, J.; Prinz, F. B., *Langmuir* **2015,** *31*, 5057-5062.

35. Detavernier, C.; Dendooven, J.; Sree, S. P.; Ludwig, K. F.; Martens, J. A., *Chem. Soc. Rev.* **2011,** *40*, 5242-5253.

36. Strempel, V.; Naumann d'Alnoncourt, R.; Driess, M.; Rosowski, F., *Rev. Sci. Instrum.* **2017,** *88*, 074102.

37. Kucheyev, S.; Biener, J.; Baumann, T.; Wang, Y.; Hamza, A.; Li, Z.; Lee, D.; Gordon, R., *Langmuir* **2008,** *24*, 943-948.

38. Lin, C.; Mao, X.; Onn, T. M.; Jang, J.; Gorte, R. J., *Inorganics* **2017,** *5* (4), 65.

39. Demmin, R.; Gorte, R., *J. Catal.* **1984,** *90*, 32-39.

40. Hutchings, G.; Copperthwaite, R.; Themistocleous, T.; Foulds, G.; Bielovitch, A.; Loots, B.; Nowitz, G.; Van Eck, P., *Appl. Catal.* **1987,** *34*, 153-161.

41. Mackus, A. J.; Kim, W.-H.; Bent, S. F., *J. Chem. Phys.* **2017,** *146*, 052802.

42. Rahmanipour, M.; Cheng, Y.; Onn, T. M.; Donazzi, A.; Vohs, J. M.; Gorte, R. J., *J. Electrochem. Soc.* **2017,** *164*, F879-F884.

43. Hafez, N.; Fathi, S.; Shokri, B.; Hosseini, S. I., *Appl. Catal. A* **2015,** *493*, 8-16.

44. Jia, L.; Farouha, A.; Pinard, L.; Hedan, S.; Comparot, J.-D.; Dufour, A.; Tayeb, K. B.; Vezin, H.; Batiot-Dupeyrat, C., *Appl. Catal. B* **2017,** *219*, 82-91.

45. Stanmore, B. R.; Brilhac, J.-F.; Gilot, P., *Carbon* **2001,** *39*, 2247-2268.

46. Bibby, D.; Milestone, N.; Patterson, J.; Aldridge, L., *J. Catal.* **1986,** *97*, 493-502.

47. McCormick, J.; Cloutier, B.; Weimer, A.; George, S., *J. Vac. Sci. & Technol. A: Vac. Surf. Films.* **2007,** *25*, 67-74.

48. Cavanagh, A. S.; Wilson, C. A.; Weimer, A. W.; George, S. M., *Nanotechnology* **2009,** *20*, 255602.

49. Héroguel, F.; Le Monnier, B. P.; Brown, K. S.; Siu, J. C.; Luterbacher, J. S., *Appl. Catal. B: Environ.* **2017,** *218*, 643-649.

50. Cargnello, M.; Jaen, J. J. D.; Garrido, J. C. H.; Bakhmutsky, K.; Montini, T.; Gamez, J. J. C.; Gorte, R. J.; Fornasiero, *P. Science*, **2012**, 337, 713-717.

51. Lu, J.; Fu, B.; Kung, M. C.; Xiao, G.; Elam, J. W.; Kung, H. H.; Stair, P. C. *Science* **2012**, 335, 1205-1208.

CHAPTER 2. EXPERIMENTAL METHODS

2.1 Atomic Layer Deposition Setup and Deposition Conditions

2.1.1 Atomic Layer Deposition Design and Setup

The issues associated with a commercial flow ALD reactor mentioned in the previous chapter must be addressed to ensure proper ALD can be carried out on high-surface area supports. Two examples involve attempts to deposit MnO and Fe_2O_3 with a commercial flow ALD reactor that were carried out on high-surface area SiO_2 (200 m^2/g) and Al_2O_3 (40 m^2/g), respectively [1,2]. The weight gained on the samples following multiple cycles of ALD reported for both were around 0.05-wt.% per cycle (approximately 20 ALD cycles would be needed to deposit 1-wt.% of material), which corresponds to ~ 5 x 10^{-3} Å per cycle, a value that is almost two orders of magnitude lower than what had been reported on flat samples [3,4]. It is most likely that the rapid convective transport of the precursors in the carrier gas have impeded the diffusion of species into the porous networks of the sample and that the weight gained is simply due to deposition on the exterior of the sample.

In order to resolve these problems, ALD was carried out in a home-built static deposition system. The system consists of three heated chambers, one for the catalyst sample and two for the organometallic precursors, which could be evacuated to ~10^{-3} Torr using a rotary vane vacuum pump. The entire setup is kept warm in its individual heated box to allow separate temperature control. As the temperature for each box may vary between 323 K to 573 K, high-temperature stainless steel bellows sealed valves (***Swagelok***

Part No: *SS-4UW-V51*) were used to separate the chambers from each other. The lines are kept warm via heating tapes with a different set of high-temperature valves (***Swagelok Part No:*** *SS-4H-VCR*) separating the chambers from both the vacuum pump and an oxidation source. It is important to keep the system warm to avoid condensation of the precursor molecules along the lines. A schematic of the home-built deposition system is shown in Figure 2.1.

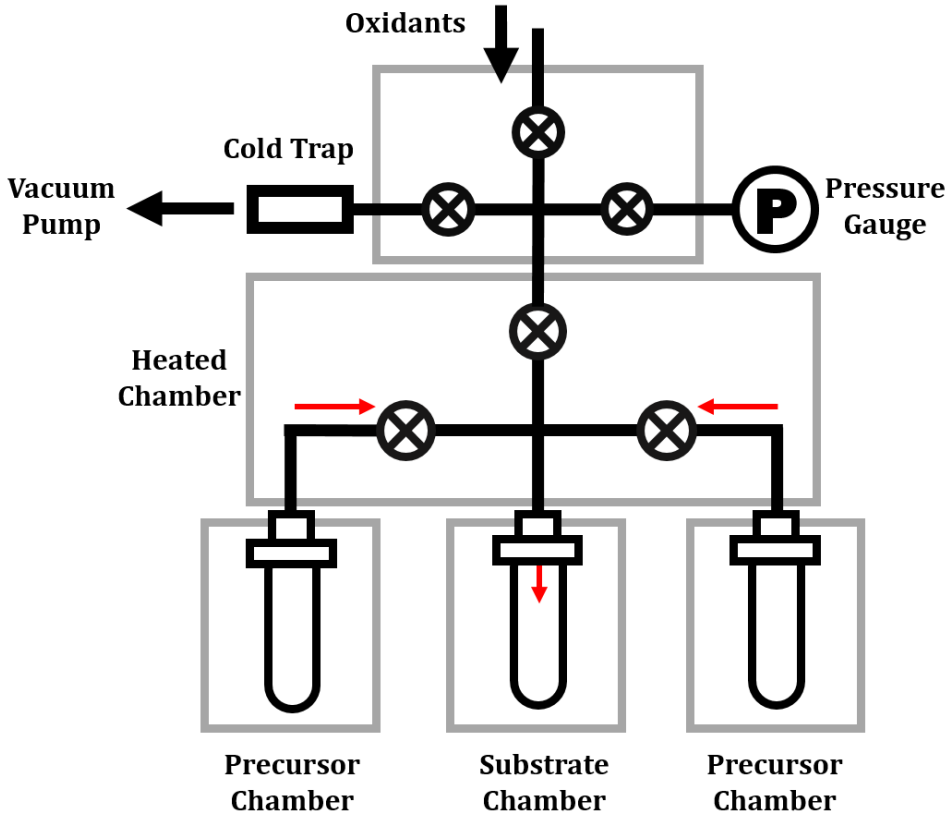

FIG. 2.1. A schematic of a home-built ALD static system. The chambers are kept warm by heated boxes with temperature control. A rotary vane vacuum pump evacuates the system to approximately 10^{-3} to 10^{-2} Torr. A cold trap is set up to prevent excess organometallic precursors from damaging the mechanical pump during normal operation.

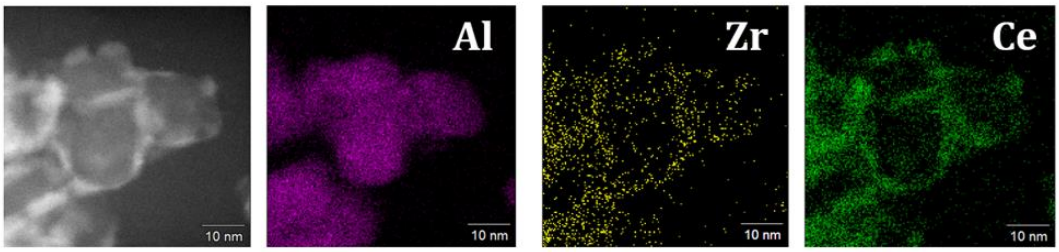

FIG. 2.2. A TEM representative of a sample prepared by ALD from the home-built ALD system. The sample had approximately 43.5-wt.% of ceria-zirconia, which corresponded to a calculated value of 1-nm film on a 130 m^2/g Al_2O_3 support. After every 5 ALD cycle, the sample was calcined at 673 K in a muffle furnace to ensure the ligands were removed.

In a typical experiment, the precursor and the catalyst sample were first sealed and vacuum evacuated to pressures of around 10^{-3} to 10^{-2} Torr. The valves connecting the sample and precursor are then closed before the chambers are heated to their respective temperatures. The deposition and precursor temperatures are dependent on the ligands attached to the organometallic precursors. It is important that the precursor is heated to provide enough vapor pressure, typically ~ 5 Torr or more, while avoiding the decomposition of the precursor molecules which leads into chemical vapor deposition behavior. Additionally, it is equally important to avoid deposition temperatures that are too low as it could lead to condensation. With adequate vapor pressure, the vapor is then allowed to flow into the evacuated sample chamber. The exposure of the vapor to the sample is typically held for 300 s or more to ensure complete surface reaction. Multiple exposures of the vapor may be introduced to saturate the surface if a large amount of sample is used. The sample chamber is then evacuated and exposed to an oxidant, typically ~ 100 Torr, for 300 s or more to remove the organic ligands. After again evacuating the sample, the procedure is repeated as often as desired. A TEM representative image of a sample prepared by ALD from the home-built ALD system is shown in Figure 2.2.

Exposure of the precursor vapor was carried out routinely by opening and closing the valves followed by evacuation. To regenerate sites for the ALD cycle to continue, there were variations in removing the ligands during the oxidation step. For example, ligands such as 2,2,6,6-tetramethyl-3,5-heptadionate could not be oxidized with oxygen or water at deposition temperatures. To ensure that the ligands were completely removed after each deposition cycles, the sample had to be removed and oxidized in a muffle furnace in the presence of air at temperatures of around 673 K. Characterization by TEM indicates that this mild temperature treatment did not affect the quality of the film formed as shown in Figure 2.2.

2.1.2 In-Situ Oxygen Plasma Generator

Another option to remove the ligand for the ALD cycle to proceed was the use of oxygen plasma generated *in-situ* the sample chamber. Inspired by glass cleaning technology used in the semiconductor industry, the setup for the home-built plasma generator is shown in Figure 2.3. The apparatus consists of a handheld tesla coil, which generates 10 kV, and a copper wire coiled around the sample tube. Under vacuum evacuation ($P \sim 10^{-3}$ to 10^{-2} Torr), the tesla coil is turned on and O_2 is slowly introduced into the sample chamber. Under moderate pressures (~ 10 Torr), the high voltage is still able to generate oxygen plasma as shown in Figure 2.3. Increasing the pressure will cause electric arcs to form, and this may interrupt with the circuits of the setup.

2.1.3 NO_2 Generator

NO_x is another potential ligand removal reagent with a high vapor pressure, which can regenerate sites on porous materials for ALD reactions to continue. NO_x oxidation technology was developed by Johnson Matthey as a means to remove soot at lower temperatures as soot only combusts at around 873 K [5]. To generate adequate vapor pressure of NO_x, a simple chemical reaction is considered:

$$2Pb(NO_3)_2\ (s) \xrightarrow{\Delta} 2PbO\ (s) + 4NO_2\ (g) + O_2\ (g)$$

It is convenient to introduce lead(II) nitrate into a chamber in the ALD setup and thermally decompose the Pb salt to form NO_2 gas. This use of NO_2 has been successfully demonstrated to remove ligands from a chemisorbed precursor, $La(TMHD)_3$, on Al_2O_3 at around 573 K [6].

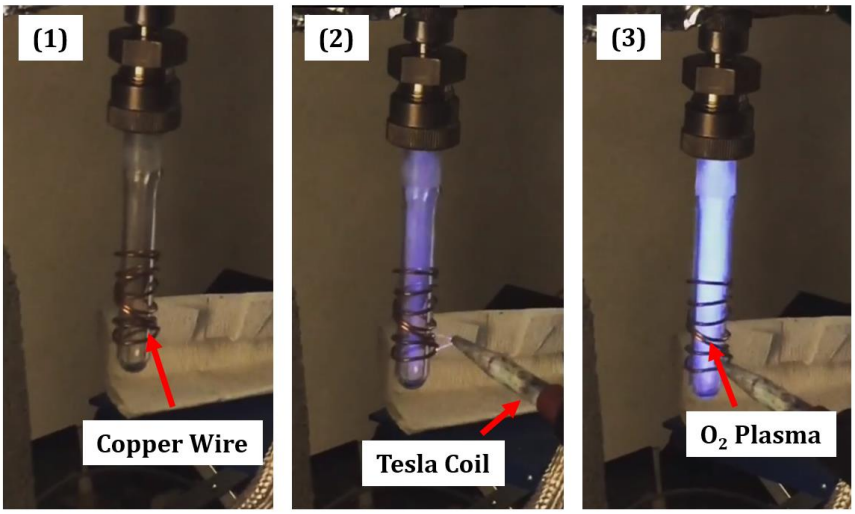

FIG. 2.3. The plasma generator component fitted onto the home-built static ALD reactor system. A copper wire is coiled around the quartz tube, which holds the porous sample. The entire setup is grounded, while the tesla coil delivers 10 kV.

2.2 Catalyst and Support Preparation

2.2.1 Preparation of Pd Catalysts

The catalysts used in all the experiments contain 1-wt.% loading of Pd supported on various materials such as γ-Al_2O_3, CeO_2, ZrO_2, Fe_2O_3, $MgAl_2O_4$, $CeZrO_4$, and ALD-modified supports. The 1-wt.% Pd was added to these supports by incipient wetness using aqueous solutions of tetraaminepalladium(II) nitrate (Sigma Aldrich), followed by drying overnight at 333 K and calcination at 773 K in air for 6 h to remove any organics and nitrates. 1-wt.% Pd on bulk $LaFeO_3$ support was prepared by the citrate sol-gel method or the Pechini method [7]. Lanthanum nitrate hexahydrate (99%, Sigma Aldrich), iron(III) nitrate nonahydrate (>98% purity, Sigma Aldrich), and aqueous solutions of tetraaminepalladium(II) nitrate were first dissolved in the appropriate ratio in distilled water. Citric acid was then added to the aqueous mixture such that the ratio of the metal ions to citric acid is 1:1. The final aqueous solution was then heated until the formation of a viscous gel was observed. The gel was dried and crushed into fine powder before it was heated to 1173 K in a muffle furnace for 6 h. The same procedure, without the use of the Pd nitrate, was carried out to prepare bulk $LaFeO_3$.

2.2.1 Preparation of Support Materials

The support, γ-Al_2O_3 (Strem Chemicals, Inc), used in the present study had been stabilized by calcining in air to 1173 K for 24 h. The BET surface area of the Al_2O_3 after this pretreatment is around 130 m^2/g. CeO_2 powder was prepared by precipitating an aqueous solution of cerium (III) nitrate hexahydrate (10 g, $Ce(NO_3)_3 \cdot 6H_2O$, Sigma

Aldrich) with excess ammonium hydroxide (NH_4OH, Fisher Scientific) while stirring. The precipitate was then filtered and dried at 333 K overnight before heating in air at 673 K for 6 h. ZrO_2 and Fe_2O_3 powders were prepared in a similar way with their respective aqueous solutions, which are zirconium (IV) oxynitrate hydrate (10 g, $ZrO(NO_3)_2 \cdot xH_2O$, degree of hydration for fresh bottle ~ 6, Sigma Aldrich) and iron (III) nitrate nonahydrate (10 g, $Fe(NO_3)_3 \cdot 9H_2O$, Sigma Aldrich). $CeZrO_4$ powder was prepared by precipitating an equimolar, aqueous mixture of $Ce(NO_3)_3 \cdot 6H_2O$ (Sigma Aldrich) and $ZrO(NO_3)_2 \cdot xH_2O$ (Sigma Aldrich, degree of hydration of fresh bottle ~ 6) with excess ammonium hydroxide (NH_4OH, Fisher Scientific). The aqueous mixture was titrated at a rate of 5 ml/min into a solution of ammonium hydroxide, with stirring, followed by calcination to 773 K for 6 h.

$MgAl_2O_4$ spinel support was prepared by precipitating an aqueous mixture of magnesium nitrate hexahydrate (Sigma Aldrich) and aluminum nitrate nonahydrate (Sigma Aldrich) with ammonium bicarbonate solution. Mg nitrate and Al nitrate were first dissolved in 400 mL of distilled water in a 1:2 molar ratio, and the aqueous mixture was then titrated at a rate of 5 ml/min onto an ammonium bicarbonate solution (600 mL, 1.5 M, pH 11.5) at 323 K under stirring condition. Note: ammonium hydroxide (NH_4OH, Fisher Scientific) solution may be added to the solution to adjust the pH to 11.5. The resulting precipitate was then filtered, rinsed with distilled water, and dried in the oven for 2 h. To stabilize the support and to ensure the formation of the $MgAl_2O_4$ spinel, the dried precipitate was then heated to 1173 K in a muffle furnace for 6 h. In order to remove any excess MgO or Al_2O_3 which may have formed, concentrated HNO_3 (10 mL, Fischer) was added to the solid mixture for 1 h after the high-temperature calcination treatment. The

resulting suspension was then filtered, rinsed with distilled water, and dried for 2 h. The dried precipitate was then heated to 773 K for 1 h to remove any nitrates.

2.3 Flow Reactor Setups with Mass Spectrometer and Gas Chromatographs

Two flow reactor setups were built to examine the catalytic and thermodynamic properties of the materials in the present study. The first reactor setup comprises of a 0.25-inch, quartz, tubular reactor attached to a gas chromatograph (GC, SRI-8610C), which is equipped with a Hayesep Q column and a TCD detector. A digital flowmeter equipped with flow controllers (MKS Mass Flo) controls the volumetric flow rate of the gases (CO, O_2, CH_4, H_2O, and H_2) entering the reactor. Helium (He) gas is used as a carrier gas for all the experiments. In a typical experiment, the catalyst (~100 mg) is loaded into the reactor to give a bed length of about 0.5 cm to 0.8 cm, between two layers of granular quartz, used both for preventing displacement of the catalyst powder and pre-heating the reagents. The reactor is then heated by a Ceramic Radiant Cylinder heater, and the temperature of the catalyst is measured with a K-type thermocouple inserted inside the reactor and touching the catalytic bed. The Gas Hourly Space Velocity for all the experiments were maintained between 72,000 to 100,000 mL g^{-1} h^{-1}.

Information regarding a material's equilibrium oxidation isotherms can be obtained by flow titration, which could be achieved by a 0.25-inch, quartz, tubular flow reactor attached to an online quadrupole mass spectrometer (SRS RGA 100). A digital flowmeter equipped with flow controllers (MKS Mass Flo) controls the volumetric flow rate of the gases (CO, O_2, CH_4, H_2O, and H_2), and the introduction of gases into the reactor is

controlled by computer-controlled solenoid valves. A leak valve separates the reactor from the mass spectrometer as the mass spectrometer must be attached to a high-vacuum chamber, which is vacuum evacuated by a diffusion pump (Varian M6) and a rotary vane pump, to function. The schematic of the reactor setup is shown in Figure 2.4. In a typical flow titration experiment, the oxidation state of the catalyst is measured by determining the amount of oxygen required to completely re-oxidize the sample after it has been equilibrated at a given P_{O_2}. The P_{O_2} is typically established by equilibrium with H_2 oxidation:

$$\mathrm{P}_{O_2}^{½} = \mathrm{K}_{equi}^{-1} \frac{\mathrm{P}_{H_2O}}{\mathrm{P}_{H_2}} \quad (\textbf{Equation 2.1})$$

Therefore, it is fixed by passing a mixture of H_2 and H_2O over the sample at a specified H_2O: H_2 ratio. Flowing air (21% O_2 and 79% N_2) is then passed over the sample, and the composition of the effluent gas was determined using a quadrupole mass spectrometer. The amount of oxygen required to re-oxidize the sample was obtained by integrating the difference between the N_2 and O_2 signals.

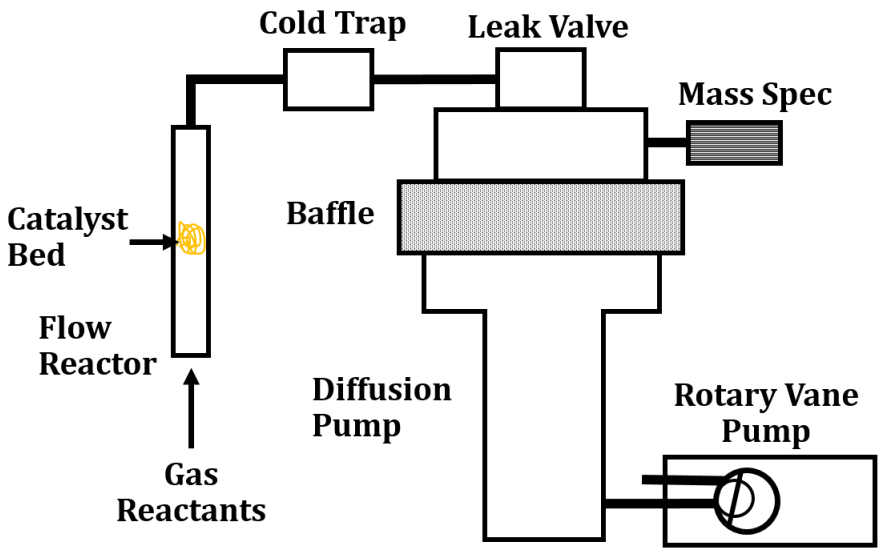

FIG. 2.4. A schematic of a home-built flow titration setup. The effluent gas is analyzed by an online quadrupole mass spectrometer reactor. The diffusion pump evacuates the chamber holding the mass spectrometer to 10^{-10} Torr.

2.4 Coulometric Titration Setup

As the H_2-H_2O ratio can only be controlled over a limited range in flow titration, coulometric titration can be used to verify the flow-titration data and to extend the range of P_{O_2} equilibrium measurements. In coulometric titration, a sample is inserted into a YSZ (yttria-stabilized zirconia) tube that had Ag electrodes painted on both inside and outside. The YSZ tube is then placed in a horizontal Ceramic Radiant Cylinder furnace and then heated to the temperature of interest. During the temperature ramp, a mixture of 5% O_2, 10% H_2O, and 85% Ar was allowed to flow over the sample at a flow rate of 110 ml/min in order to ensure that the sample was completely oxidized at the start of the measurements. The ends of the YSZ tube were then sealed with a closed end Cajon fittings. Specified

amounts of oxygen were then electrochemically pumped from the inside of the YSZ tube by applying a current across the electrodes using a Gamry instruments potentiostat. After allowing the system to come to equilibrium with the electrodes at open circuit, the equilibrium P_{O_2} was calculated from the Nernst equation and the open circuit potential. The schematic for this setup is shown in Figure 2.5.

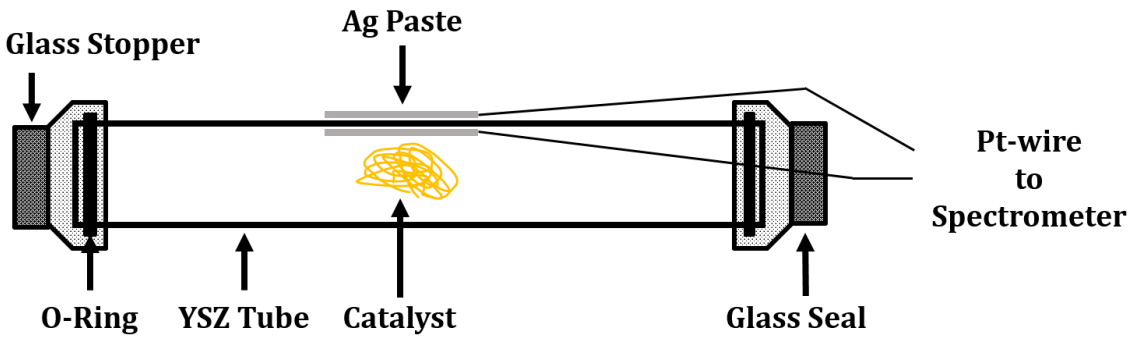

FIG. 2.5. A schematic of a coulometric titration setup used to measure thermodynamic properties of a catalyst sample. The entire setup is placed in a horizontal Ceramic Radiant Cylinder furnace and heated to the temperature of interest. Ag electrodes are used to measure the potential difference. The dense YSZ tube is sealed with a Viton O-ring so leaks can be neglected.

This technique measures the sample composition as a function of $p(O_2)$ for the oxides and provides redox isotherms of the oxides as a function of oxygen fugacity from equilibrium constants. For example, for a given redox reaction,

$$MO_x + O_2 \leftrightarrow MO_{x+2}$$

$$K_{eq} = \frac{a_{MO_{x+2}}}{a_{MO_x} * P(O_2)} = P(O_2)^{-1} \ (\textbf{Equation 2.2})$$

where M is a metal, the equilibrium constant is a function only of the oxygen fugacity

since the activity of solids is equal to 1. The differential Gibbs free energy of the oxidation reaction can then be calculated using:

$$\Delta G = RT\ln\left(K_{eq}\right) \quad (\textbf{Equation 2.3})$$

2.5 Catalyst Characterization

2.5.1 BET Surface Area Measurement

In the present study, sample surface areas were determined from BET isotherms using N_2 or Kr adsorption at 78 K. In this procedure, the sample was first heated to 423 K for 10 min while under vacuum evacuation to remove any moisture from the sample. Liquid nitrogen was then used to cool the sample to 78 K. The surface area can be calculated from the volume of adsorbed N_2 or Kr gas required to form a monolayer, as estimated using the BET measurements and the size of the Kr and N_2 molecule.

2.5.2 CO Chemisorption

Metal dispersions were determined volumetrically using CO adsorption uptakes at room temperature on the reduced catalysts. In this procedure, the samples were first oxidized in 200 Torr O_2 at 673 K and reduced in 200 Torr H_2 at 423 K before measuring CO uptakes. Dispersions were calculated assuming one CO is uptake by one Pd particle for all Pd-based catalysts.

2.5.3 X-Ray Diffraction (XRD)

X-Ray Diffraction (XRD) patterns were recorded on a Rigaku Smartlab diffractometer equipped with a Cu Kα source (λ = 0.15416 nm). Powder samples were

placed on a glazed glass slide and wetted with acetone to hold the samples intact. The scans were performed between 2θ range of 20˚ to 60˚, with a sampling interval of 0.02˚ and a scan speed of 2˚/min. For some of the samples, a small amount of graphite was physically mixed with the oxides to act as a reference.

2.5.4 Inductively Coupled Plasma (ICP)

The elemental compositions of the samples were measured by Inductively Coupled Plasma-Optical Emission spectrometry (ICP-OES) performed on a Spectro Genesis spectrometer with a concentric nebulizer. For the ICP-OES measurement, each sample (~50 mg) was dissolved in a 5-mL solution of Aqua Regia overnight. The solutions were then diluted with a 10 wt.%. HNO_3 solution to the appropriate concentration before the ICP analysis.

2.5.5 Fourier Transform Infrared (FTIR)

Fourier Transform Infrared (FTIR) spectra were collected on a Mattson Galaxy FTIR with a diffuse-reflectance attachment (Collector II^{TM}) purchased from Spectra-Tech Inc. Spectra were typically collected at 2 to 4 cm^{-1} resolution. For some samples, the intensities of the spectral features were normalized by making the background peaks between 700 cm^{-1} and 1000 cm^{-1} be identical for all cases.

2.5.6 Transmission Electron Microscopy (TEM)

Ex-situ scanning transmission electron microscopy (STEM) was carried out at the University of California – Irvine on powder specimens that had been sonicated in methanol

and dropped onto carbon support films on copper TEM grids (Ted Pella, Inc.). Specimens were examined with a JEOL 3100R05 electron microscope with double spherical aberration-correctors operated at 300 kV in scanning mode.

In-situ TEM was performed on a fresh ALD powder specimen under 150 Torr of O_2 at elevated temperature with an electron transparent gas cell. Specimens were examined with a JEOL 3100R05 electron microscope with double spherical aberration-correctors operated at 300 kV in scanning mode. The microscope is equipped with a horizontal ultra-thin Window JEOL SDD X-ray detector capable of detecting elements with Z > 5 and Gatan #965 Quantum Imaging Filter (GIF) for electron energy loss spectroscopy.

2.5.7 Raman Spectroscopy

Raman spectra were recorded with an Invia Renishaw micro spectrometer equipped with He−Ne laser at 532 nm. Raman measurements were carried out with a laser power of 1 mW at the sample and a collection time of 20 s. At least 5 spectra per sample were recorded in order to check the uniformity of the materials.

2.5.8 X-ray Photoelectron Spectroscopy (XPS)

X-ray photoelectron spectroscopy (XPS) was carried out in an ultra-high vacuum system with a base pressure of $1x10^{-8}$ Pa equipped with a dual Mg/Al X-ray source (SPECS XR50), an ion gun (Omicron ISE 10) and an electron/ion energy analyzer (SPECS Phoibos 150). Pd(3d), Ce(3d), Zr(3d), O(1s) and C(1s) levels were probed using an excitation energy of $h\upsilon$=1486.6 eV (Al K-α). Binding energies are reported after correction for charging using adventitious C(1s) as a reference.

2.5.9 Extended X-Ray Absorption Fine Structure(EXAFS) and X-ray Absorption Near Edge Structure (XANES)

Pd K-edge EXAFS and XANES data were measured on the SAMBA beamline at the Synchrotron SOLEIL (Gif sur Yvette, France). Spectra were collected by measuring the K_α fluorescence line with a 36 pixels Germanium detector (Canberra), while transmission data was simultaneously recorded with ionization chambers (IC-SPEC, FMB-Oxford) for the sample and a Pd foil. Harmonic rejection has been accomplished by using two Pd coated mirrors, two different setups have been used, one for Pd (2 mrad) and one for Fe (6 mrad) K edges. Data analysis has been performed with the code Horae combined with Feff8.4.

2.5.10 CO-O_2 Pulse Experiments

The reducibility of metals and metal oxides were determined by transient-pulse experiments using a similar flow reactor system equipped with the online quadrupole mass spectrometer described above. Reactant gases were passed over 200-mg samples in a 1/4 -inch quartz tube. The total flow rate with He as the carrier gas was kept constant at 25 mL/min, while the concentrations of the reactive component (either CO or O_2) was chosen to be 10% of the total gas stream. Integration of the partial pressures as a function of time allowed accurate determination of the amounts of CO_2 formed during a CO pulse. Prior to taking the pulse data, the samples were first calcined in 10% O_2 at 673 K for 15 min. This treatment was followed by reduction in 10% CO at 673 K for 10 min and then re-oxidation in 10% O_2 for an additional 15 min.

2.6 References

1. Yang, N.; Yoo, J. S.; Schumann, J.; Bothra, P.; Singh, J. A.; Valle, E.; Abild-Pedersen, F.; Nørskov, J. K.; Bent, S. F., *ACS Catal.* **2017,** *7*, 5746-5757.

2. Hu, Q.; Wang, S.; Gao, Z.; Li, Y.; Zhang, Q.; Xiang, Q.; Qin, Y., *Appl. Catal. B.* **2017,** *218*, 591-599.

3. Martinson, A. B.; DeVries, M. J.; Libera, J. A.; Christensen, S. T.; Hupp, J. T.; Pellin, M. J.; Elam, J. W., *J. Phys. Chem. C.* **2011,** *115*, 4333-4339.

4. Burton, B.; Fabreguette, F.; George, S., *Thin Solid Films* **2009,** *517* (19), 5658-5665.

5. He, B. J.-J.; Wang, C.-X.; Zheng, T.-T.; Zhao, Y.-K., *Johns. Matthey Technol. Rev.* **2016,** *60*, 196-203.

6. Rahmanipour, M.; Cheng, Y.; Onn, T. M.; Donazzi, A.; Vohs, J. M.; Gorte, R. J., *J. Electrochem. Soc.* **2017,** *164*, F879-F884.

7. Gosavi, P. V.; Biniwale, R. B. *Mater. Chem. Phys.* **2010,** *119*, 324-329.

CHAPTER 3. ATOMIC LAYER DEPOSITION OF IRON OXIDE ON HIGH SURFACE AREA ALUMINA BY A STATIC ALD REACTOR

Summary:

Initial work with our home-built static ALD system demonstrated that it was possible to deposit thin iron oxide film on a 130-m^2/g γ-Al_2O_3 for use as a catalyst support. Measurements of the sample mass, surface area, and pore-size distribution as a function of the number of ALD cycles suggested that the iron oxide grew as a dense, conformal film. Surface area measurements suggested that it was critical to maintain the thickness of the film between 0.3 to 1.5-nm to avoid issues associated with pore blockages. While films with 20 ALD cycles (20Fe_2O_3-Al_2O_3, 0.25 g Fe_2O_3/g Al_2O_3) were difficult to distinguish by HAADF STEM, EDS mapping indicated the Al_2O_3 was uniformly coated. Raman Spectroscopy showed the films were in the form of Fe_2O_3; but XRD measurements on samples with as many as 100 ALD cycles (100Fe_2O_3-Al_2O_3, 0.84 g Fe_2O_3/g Al_2O_3) showed no evidence for crystalline iron-oxide phases, even after calcination at 1073 K. Specific rates for the water-gas-shift (WGS) reaction on the ALD-coated samples were significantly lower than those on bulk Fe_2O_3. However, addition of 1-wt% Pd to Fe_2O_3/Al_2O_3 supports prepared by ALD exhibited specific rates that were much higher than that observed when 1-wt% Pd was added to Fe_2O_3/Al_2O_3 prepared by conventional impregnation of iron salts, suggesting uniform contact between the Pd and FeO_x phases on samples prepared by ALD.

[*This chapter was published as a research paper in the Applied Catalysis A: General, 534 (2017) 70-77. Copyright: 2017, Elsevier.*]

3.1 Introduction

As mentioned in Chapter 1, reducible oxides are of great interest as both promoters for catalysts and as catalysts themselves. An important example of this is ceria-zirconia mixed oxides, which are used as the oxygen-storage component in automotive, three-way catalysts [1,2]. Another interesting example is iron oxide, which is used as a high-temperature, water-gas-shift (WGS) catalyst, either by itself or together with a metal promoter, such as Cu [3,4], Ru [5,6], or Pd [7]. A major problem with these and other reducible oxides is that their surfaces areas tend to be low and to decrease with time. Commercial iron-oxide, WGS catalysts may have initial surface areas between 30 and 100 m^2/g because of added Cr_2O_3 and Al_2O_3 but loss of iron-oxide surface area is a major cause for deactivation [8]. Furthermore, although chromia is effective for stabilizing iron oxide catalysts, chromia toxicity is a cause for concern during catalyst manufacture and handling, so that there would be benefits to avoiding its use [8].

A common strategy for achieving high surface areas with functional oxides is to disperse them on a more stable support, such as alumina or zirconia [9,10]. When these functional oxides are added by conventional impregnation, they tend to form larger crystallites, so that the actual active surface area may not be greatly enhanced. In ALD, layers of oxides can be deposited uniformly on the supports. However, concerns with the conventional ALD approach have been strongly expressed in Chapter 1 as diffusion issues may arise. With high-surface area supports, it must also be noted that the practical film thickness cannot be greater than 1 or 2-nm. For example, the Fe_2O_3 loading corresponding to a 1-nm film with bulk properties on a 100 m^2/g substrate would be 0.52 g Fe_2O_3/g of

substrate (~ 33 wt.% Fe_2O_3). Even if decreases in pore size or blockage of pore entrances were not an issue, the added mass of the sample would significantly decrease the specific surface area of the catalyst (100/1.52 = 66 m^2/g).

In the present work, we investigated the formation of iron-oxide films on alumina by ALD using a home-built static ALD system. The results indicate that it is possible to prepare high-surface-area metal oxide on a porous support but it is important to maintain film thicknesses between 0.3 to 1.5-nm to prevent blockages of the pore entrances. Examination of the catalytic properties indicate that promotion of these films with Pd can provide very high WGS activities compared to conventional materials.

3.2 Experimental Methods

The high-surface-area, Fe_2O_3 films were prepared by Atomic Layer Deposition (ALD) using a home-built apparatus described in Chapter 2. Ferrocene ($Fe(Cp)_2$, Sigma Aldrich) was chosen to be the organometallic precursor due to its high vapor pressure and thermal stability. The deposition conditions were adopted with slight modification from past successful studies on flat surfaces [11]. The $Fe(Cp)_2$ precursor was heated to 393 K to produce a $Fe(Cp)_2$ vapor pressure of about 5 to 10 Torr. During the deposition cycle, the $Fe(Cp)_2$ vapor was introduced to the evacuated sample chamber, which contained approximately 0.5-g Al_2O_3. The alumina substrate was exposed to the precursor vapor at 623 K for 300 s to ensure that reaction with the surface was complete. After evacuation, the alumina substrate was oxidized by exposing it to 200 Torr of O_2 for 300 to 600 s.

The alumina substrate used in this study was a γ-Al_2O_3 (Strem Chemicals, Inc.), stabilized by calcining in air to 1173 K for 24 h. Bulk Fe_2O_3 powder was prepared via precipitation with excess NH_4OH (Fisher Scientific) as described in Chapter 2. For comparison to Fe_2O_3(ALD)-Al_2O_3 samples prepared by ALD, Fe_2O_3(IMP)/Al_2O_3 samples were prepared by impregnation of $Fe(NO_3)_3$•$9H_2O$ of similar weight loading into the same alumina substrate, followed by calcination to 673 K for 6 h to remove all nitrates. Catalysts containing 1-wt% Pd were synthesized by incipient wetness using aqueous solutions of tetraamine-palladium(II) nitrate (Sigma Aldrich).

To characterize film growth during ALD, we measured the sample weights and BET surface areas as a function of the number of ALD cycles. XRD, STEM, and Raman spectroscopy were also used to characterize the ALD-prepared sample. The catalytic properties of Pd-supported on the ALD-prepared sample were probed using Pd dispersion measurements and steady-state water-gas-shift reaction measurements. Reaction rates were measured in the flow reactor equipped with a gas chromatograph. The setup is described in Chapter 2, The partial pressures of CO and H_2O were both at 25 Torr (3.3-vol.%). The total flow rate of He was kept at 60 mL/min. Before testing, each sample was activated by heating the catalysts to 673 K in the reaction mixture before cooling back to the desired reaction temperature. The mass of catalyst used in every rate measurement was 0.10 g, and differential conversions were maintained in all cases. Transient, pulse experiments were performed using equipment and procedure described in Chapter 2.

3.3 Results

3.3.1. Characterization of Fe_2O_3 films by ALD on Al_2O_3

The growth of the Fe_2O_3 film was first characterized by measuring the changes in the mass and BET surface area of samples as a function of the number of $Fe(Cp)_2$-O_2 ALD cycles, with the mass increase shown in Figure 3.1(a) and the surface areas reported in Figure 3.1(b). The mass of the iron-oxide films increased with the number of cycles for N < 50, but the growth rate decreased at higher coverages. To ensure that the added mass was due to Fe_2O_3, the composition of the samples was verified by ICP-OES. Assuming that Fe_2O_3 forms a dense, uniform film with bulk density in the low coverage regime, the initial weight gain per cycle corresponded to a growth rate of 0.016 nm/cycle. This value is similar to that reported in the literature for the growth rate of Fe_2O_3 using $Fe(Cp)_2$ on flat surfaces [12]. After 100 cycles, the $Fe(Cp)_2$ uptakes dropped to near zero, implying that we were not able to grow Fe_2O_3 films beyond that point.

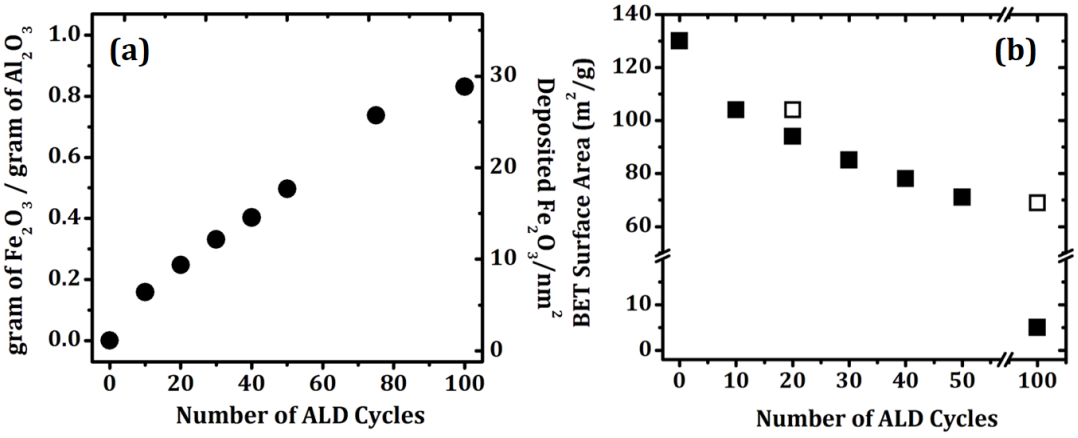

FIG. 3.1. (a) Mass change and (b) BET surface area as a function of the number of Fe_2O_3 ALD cycles on γ-Al_2O_3 after calcination to 773 K. The surface areas in the two open symbols were measured after calcining the samples to 1073 K.

Figure 3.1(b) demonstrates that the surface area of the sample decreased in a regular manner with the number of ALD cycles. Initially, most of the loss in specific surface area was due to the increase in sample mass. For example, after 20 ALD cycles, the mass increase was roughly 0.25 g Fe_2O_3/g Al_2O_3 and the specific surface area decreased from 130 m^2/g to 93 m^2/g. The mass increase alone would change the specific surface area to 104 m^2/g (130 m^2/1.25 g) and the additional decrease is likely due to a decrease in average pore radius. However, after 100 cycles, the same point at which $Fe(Cp)_2$ uptakes stopped, there was a dramatic decrease in specific surface area to 3 m^2/g. Since the entire pore volume cannot have been filled with Fe_2O_3, the entrance to the nanopores must have been blocked after 100 cycles, making any internal volume inaccessible to either N_2 or $Fe(Cp)_2$. That this was the case was further demonstrated by the fact that calcination of this sample in air to 1073 K restored the surface area from 3 m^2/g to 70 m^2/g. Apparently, high-temperature treatment caused some sintering which opened these smaller pores. It is interesting to notice that high-temperature calcination of the $20Fe_2O_3$-Al_2O_3 sample had only small effect on the surface area, increasing from 93 to 102 m^2/g. This would argue that there is only minimal porosity in the deposited FeO_x films.

To further understand how the ALD films affect the nanopores, the pore-size distributions were measured from the N_2 adsorption isotherm for samples after deposition of 0, 10, 20, and 40 ALD cycles. The isotherms are shown in Figure 3.2 while average pore sizes and pore size distributions are reported in Table 3.1 and Figure 3.3. All the samples showed type IV isotherms, with a bimodal trend, which is most evident for the calcined Al_2O_3. With the exception of the loss of very large, ~30-nm pores that were present on the

initial Al_2O_3, there were no dramatic changes in the pore sizes with either increasing calcination temperature or increasing number of ALD cycles. The peak in pore-size distribution for the starting Al_2O_3 occurred at 9.56 nm and decreased to 8.47 nm on the $40Fe_2O_3$-Al_2O_3 sample. From the weight increase after 40 ALD cycles, a uniform, dense Fe_2O_3 film would be 0.72 nm thick, so that cylindrical pores should decrease from 9.56 nm to 8.12 nm, in reasonable agreement with our experimental observations.

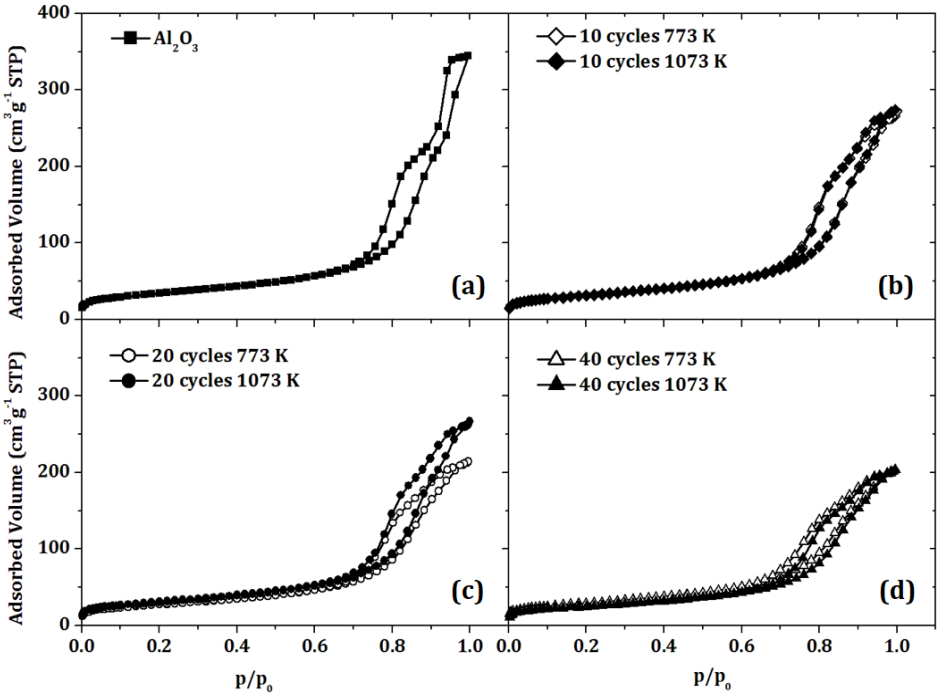

FIG. 3.2. BET Isotherms of (a) Al_2O_3, which was calcined to 1173 K, and ALD-modified support with different coverages: (b) $10Fe_2O_3$-Al_2O_3, (c) $20Fe_2O_3$-Al_2O_3, and (d) $40Fe_2O_3$-Al_2O_3

XRD results for selected samples are shown in Figure 3.4, together with the expected peak positions for α-Fe_2O_3 at the bottom. The pattern for the unmodified Al_2O_3 is shown in Figure 3.4(a) for reference, while diffraction patterns for samples prepared by

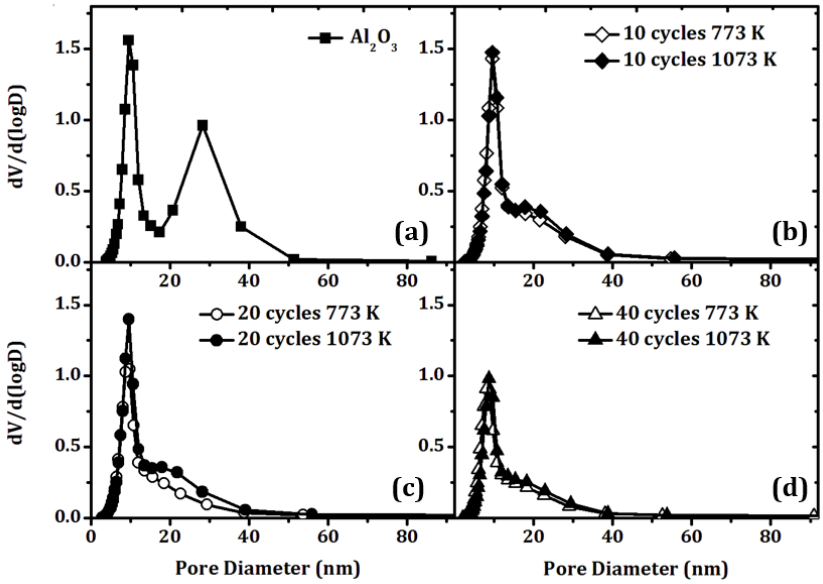

FIG. 3.3. Pore-size distributions determined from N_2 adsorption isotherms on (a) the γ-Al_2O_3 support, (b) 10Fe_2O_3-Al_2O_3 (c) 20Fe_2O_3-Al_2O_3, and (d) 40Fe_2O_3-Al_2O_3 after calcination at 773 K and 1073 K.

ALD with low (20Fe_2O_3-Al_2O_3, 0.25 g Fe_2O_3/g Al_2O_3) and high coverages (100Fe_2O_3-Al_2O_3, 0.84 g Fe_2O_3/g Al_2O_3), calcined in air to 1073 K, are shown in Figures 3.4(b) and 3.4(c). Even with the addition of these large amounts of Fe_2O_3, there are no obvious diffraction features that can be associated with the Fe. For comparison, Figure 3.4(d) shows the XRD pattern for the Fe_2O_3(IMP)/Al_2O_3 sample, prepared by impregnation to have 0.84 g Fe_2O_3/g Al_2O_3, similar to the high-loading ALD sample. The XRD pattern of the impregnated sample showed clear features associated with α-Fe_2O_3. With the ALD-prepared samples, the films are apparently thinner than the coherence length of the x-rays, while the results for the impregnated sample are consistent with the formation of relatively large crystallites.

Additional evidence for the formation of thin films in the ALD-prepared samples came from High Angle Annular Dark Field (HAADF) STEM imaging and EDS elemental

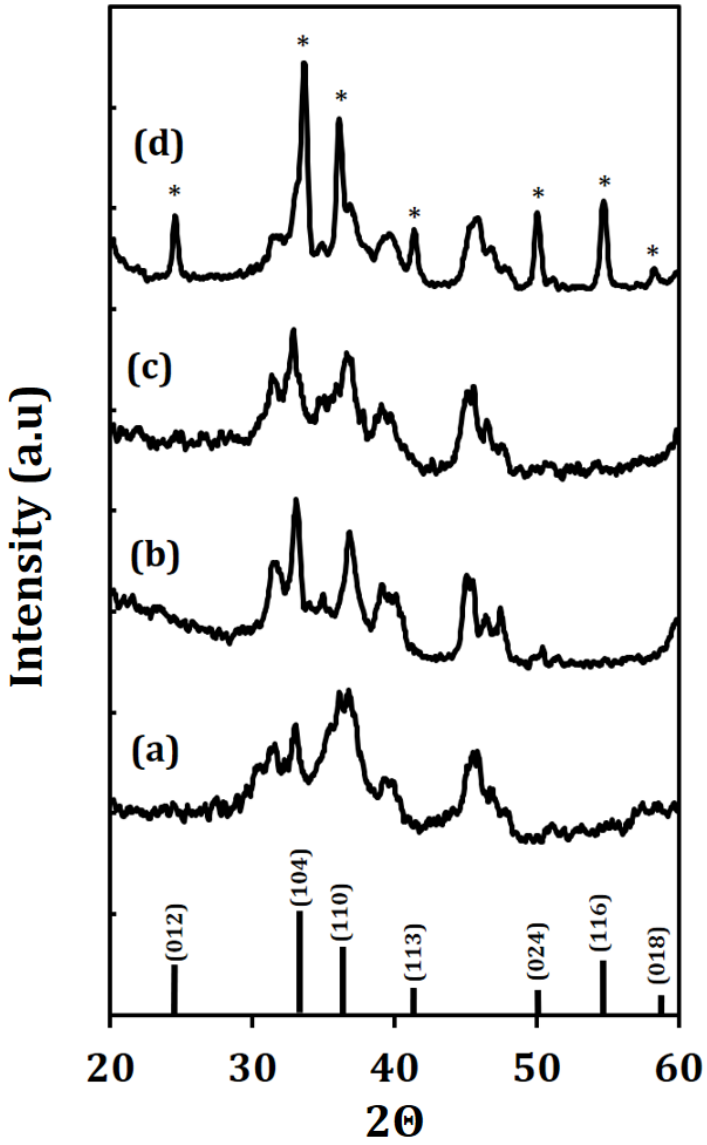

FIG. 3.4. XRD patterns of (a) the γ-Al_2O_3 support after heating to 1173 K and two ALD-coated samples after calcination to 1073 K: (b) 20Fe_2O_3-Al_2O_3 and (c) 100 Fe_2O_3-Al_2O_3. The pattern in (d) was obtained on Fe_2O_3(IMP)/Al_2O_3 with the same Fe_2O_3 loading as 100Fe_2O_3-Al_2O_3 heated to 1073 K. Characteristic peaks for hematite, α-Fe_2O_3, are shown by the bold lines and marked by *.

mapping, shown in Figure 3.5. Results are shown for samples with 0.25 g Fe_2O_3/g Al_2O_3 made by infiltration, (Fe_2O_3(IMP)/Al_2O_3, Figure 3.5(a)), and by ALD (20Fe_2O_3-Al_2O_3, Figure 3.5(b)). Due to the small difference in the atomic number between Fe and Al, HAADF images alone were not sufficient to clearly show how Fe is distributed on the Al_2O_3 in either case, even when using the aberration-corrected STEM. However, EDS elemental maps for Al, Fe, and O confirmed that relatively large Fe_2O_3 agglomerates were present on the infiltrated sample while thin layers of Fe appeared to uniformly coat Al_2O_3 for the ALD-coated sample.

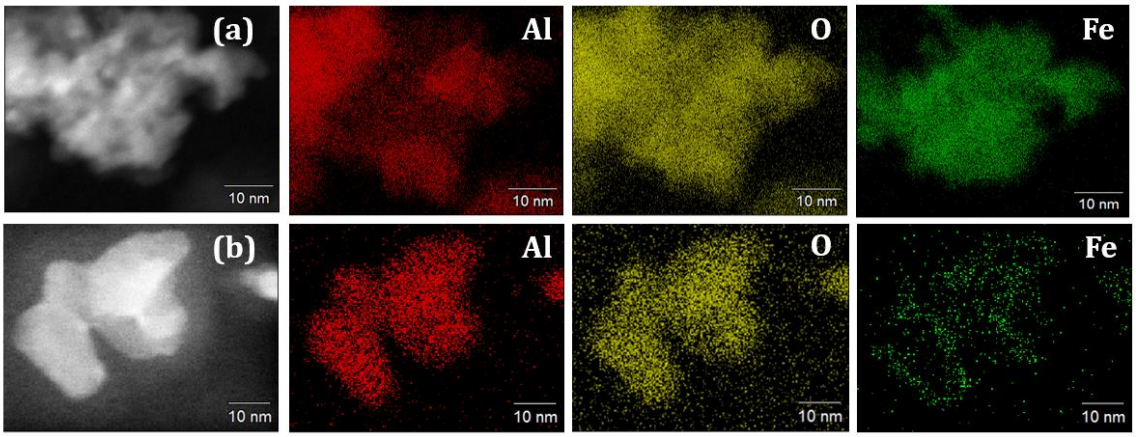

FIG. 3.5. High angle annular dark field STEM image of (a) Fe_2O_3(IMP)/Al_2O_3 (0.25 g Fe_2O_3/g Al_2O_3) and (b) 20Fe_2O_3-Al_2O_3 after calcination at 773 K. EDS mapping of Al, O, and Fe shows rich Fe signals on the edges on the ALD-modified Al_2O_3 support, while there was no preferential distribution of Fe on the infiltrated sample.

Raman spectra, shown in Figure 3.6, provided additional evidence about how the FeO_x films evolved with coverage. The spectra in Figures 3.6(a) to 3.6(c) were obtained on samples prepared by ALD with 10, 20, and 50 cycles, while the spectrum in Figure 3.6(d) was obtained from the Fe_2O_3(IMP)/Al_2O_3 sample prepared by impregnation with

0.25-g Fe_2O_3/g Al_2O_3. The sample with 10 ALD cycles, 10Fe_2O_3-Al_2O_3, exhibited only a single, sharp band at 250 cm^{-1}, which is also the most intense band observed for lepidocrocite. This suggests that the very thin ALD film retained a γ-FeO(OH) structure even after calcination to 773 K. By comparison, the Raman spectra of the ALD-prepared samples with higher Fe_2O_3 coverages, 20Fe_2O_3-Al_2O_3 and 50Fe_2O_3-Al_2O_3, along with the impregnated sample, Fe_2O_3(IMP)/Al_2O_3, all exhibit broad bands at 365, 720-730 and 1390-1430 cm^{-1}. These peaks are consistent with the formation of γ-Fe_2O_3 (maghemite).

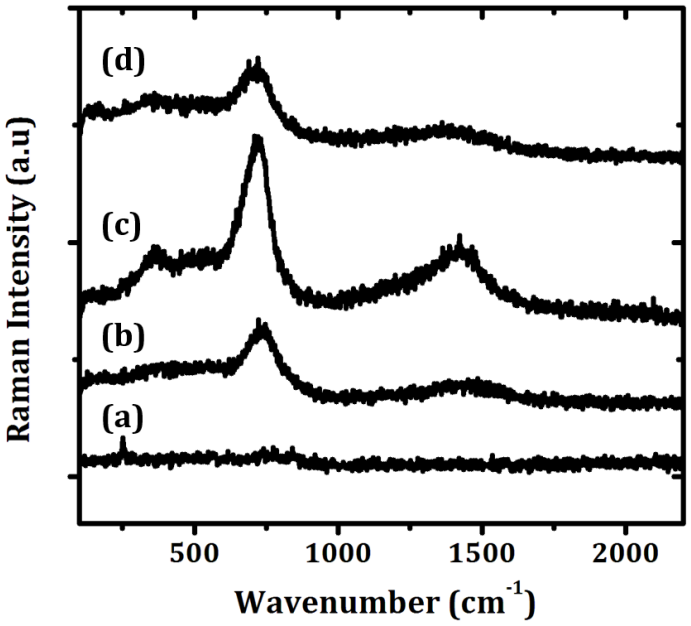

FIG. 3.6. Raman spectra of various Fe_2O_3/Al_2O_3 supports: (a) 10Fe_2O_3-Al_2O_3, (b) 20Fe_2O_3-Al_2O_3, and (c) 40Fe_2O_3-Al_2O_3 and (d) Fe_2O_3(IMP)/Al_2O_3 (0.25 g Fe_2O_3/g Al_2O_3).

3.3.2 Catalytic Properties of Fe_2O_3 Film:

Since Fe_3O_4 is the catalytically active phase in high-temperature WGS catalysts, we examined how modification of the Al_2O_3 support by ALD of Fe_2O_3 at different

coverages compares to bulk Fe_2O_3 and a conventional supported catalyst, Fe_2O_3(IMP)/Al_2O_3. Figure 3.7 shows specific rates, measured under differential conditions at 25 Torr each of H_2O and CO, as a function of temperature for bulk Fe_2O_3, Fe_2O_3(IMP)/Al_2O_3 with 0.13 g Fe_2O_3/g Al_2O_3, and two ALD-prepared samples, 10Fe_2O_3-Al_2O_3 and 40Fe_2O_3-Al_2O_3. Rates have been normalized to the BET surface areas, which were 41 m^2/g for bulk Fe_2O_3, 110 m^2/g for Fe_2O_3(IMP)/Al_2O_3, 104 m^2/g for 10Fe_2O_3-Al_2O_3, and 77 m^2/g for 40Fe_2O_3-Al_2O_3. While we expect the exposed surfaces of the ALD-prepared samples to consist of iron oxide, a significant fraction of the exposed surface on the Fe_2O_3(IMP)/Al_2O_3 sample will almost certainly be alumina, so that this normalization will underestimate the specific activity of the FeO_x on that sample.

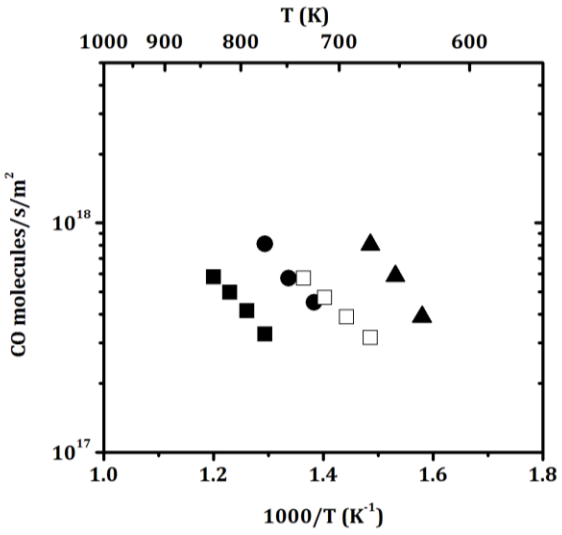

FIG. 3.7. Steady-state, differential reaction rates for the water-gas-shift (WGS) reaction with partial pressures of 25 Torr CO and 25 Torr H_2O: (■) – 10Fe_2O_3-Al_2O_3; (●) – 40Fe_2O_3-Al_2O_3; (▲) – bulk Fe_2O_3; and (□) – Fe_2O_3(IMP)/Al_2O_3 (0.13 g Fe_2O_3/g Al_2O_3). The rates were normalized to the BET surface areas and all catalysts were calcined to 773 K.

Bulk Fe_2O_3 showed by far the highest specific rates, roughly three times higher than those on the Fe_2O_3(IMP)/Al_2O_3 sample and 10 times higher than that on the 10Fe_2O_3-Al_2O_3 sample. The lower specific rates on Fe_2O_3(IMP)/Al_2O_3 can be explained by the fact that only a fraction of the surface area is FeO_x; however, this cannot explain the lower rates on the ALD-prepared samples. It has been reported that the active sites on Fe_3O_4 correspond to Fe^{3+}-Fe^{2+} pairs [13]; therefore, it is possible that the concentration of these sites is lower in two-dimensional films. For example, one study of supported Fe_2O_3 particles reported that the Fe_2O_3-Fe_3O_4 equilibrium shifted to higher P(O_2) on supported particles [9]. The fact that specific rates were higher on the 40Fe_2O_3-Al_2O_3 compared to 10Fe_2O_3-Al_2O_3 suggests that the catalytic activity will increase as one approaches bulk conditions.

Because WGS rates could depend on surface structure as well as surface area, a possibly better indication of the fraction FeO_x exposed at the catalyst surface is obtained by measuring WGS rate after impregnation of 1-wt% Pd. Contact between Pd and FeO_x results in reaction rates that are much higher than those observed on either Pd/Al_2O_3 or FeO_x catalysts individually [7], so that ALD-prepared catalysts should be more effective if all of the surface consists of FeO_x. This is indeed the case, as shown in Figure 3.8. Because reaction is expected to occur at the interface between Pd and FeO_x, rates for these catalysts have been normalized to the mass of the catalysts, since each contained 1-wt% Pd. Also, because the Pd-containing samples were so much more active, rates were measured at lower temperatures. For calcination at 773 K, specific rates on 1-wt% Pd on 20Fe_2O_3-Al_2O_3 were essentially identical to those on Pd/Fe_2O_3, implying that all of the Pd is in contact with Fe_2O_3 in both cases. Rates for Pd/Al_2O_3 were roughly a factor of 10 lower, with those

on $Pd/Fe_2O_3(IMP)/Al_2O_3$ (with 0.25 g Fe_2O_3/g Al_2O_3) in between. The lower rates for $Pd/Fe_2O_3(IMP)/Al_2O_3$ are consistent with much of the Pd not being in contact with FeO_x. Calcination to 1073 K had little effect 1-wt% Pd on $20Fe_2O_3$-Al_2O_3 because the surface area of the ALD sample was maintained, while rates on Pd/Fe_2O_3 decreased by a factor of about two due to the fact that the BET surface area dropped from 41 m^2/g to 2 m^2/g. Rates on $Pd/Fe_2O_2(IMP)/Al_2O_3$ decreased dramatically, presumably due to further loss in interfacial contact between the Pd and the iron oxide component of the support.

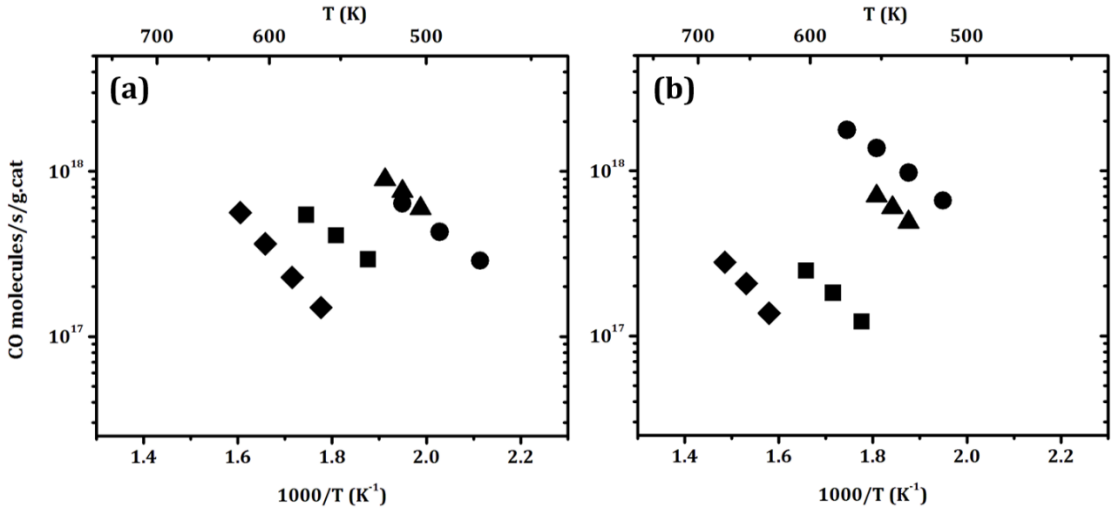

FIG. 3.8. Steady-state, differential reaction rates for the water-gas-shift (WGS) reaction with partial pressures of 25 Torr CO and 25 Torr H_2O after addition of 1-wt Pd. Rates were measured after calcination to (a) 773 K or (b) 1073 K: (●) – $Pd/20Fe_2O_3$-Al_2O_3, (▲) – Pd/Fe_2O_3, (■) $Pd/Fe_2O_3(IMP)/Al_2O_3$ (0.25 g Fe_2O_3/g Al_2O_3), and (♦) – Pd/Al_2O_3.

To verify Fe_2O_3 films prepared by ALD are reducible, CO-O_2 pulse measurements were performed on the 1-wt% Pd/Al_2O_3 and 1-wt% $Pd/20Fe_2O_3$-Al_2O_3 samples at 673 K. The data are shown in Figure 3.9. The regions between the dashed lines in the figure correspond to periods of time during which 10% O_2 (m/e = 32), 10% CO (m/e = 28), or

pure He was passing over the catalyst. The observation of CO_2 (m/e = 28, 44) upon exposure of the catalyst to CO is due to reduction of the catalyst and the reducibility can be calculated from the amount of CO_2 that is formed. It is qualitatively apparent that less reduction occurred in the 1-wt% Pd/Al_2O_3 sample, Figure 3.9(a) than in the 1-wt% $Pd/20Fe_2O_3$-Al_2O_3 sample, Figure 3.9(b).

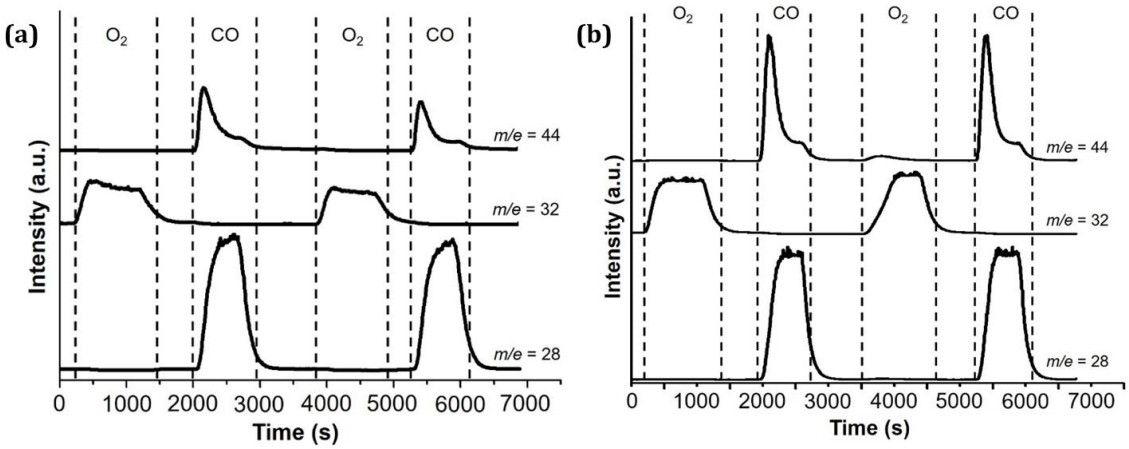

FIG. 3.9. CO-O_2 pulse measurements on a) 1-wt% Pd/Al_2O_3 and b) 1-wt% $Pd/20Fe_2O_3$-Al_2O_3 at 673 K. The data show CO (m/e = 28) O_2 pulse (m/e = 32) and CO_2 (m/e = 28, 44).

Based on the amount of CO_2 produced during the reduction cycles, 90 μmol of atomic oxygen could be reversibly removed per gram of catalyst on 1-wt% Pd/Al_2O_3 and 380 μmol/g on 1-wt% $Pd/20Fe_2O_3$-Al_2O_3. Theoretically, 1-wt% Pd/Al_2O_3 sample can give up 94 μmol/g of atomic oxygen by reduction of PdO, in reasonable agreement with the experimental results. Bulk reduction of Fe_2O_3 to Fe_3O_4 would yield 2100 μmol/g of oxygen, so that the $20Fe_2O_3$-Al_2O_3 sample (0.25 g Fe_2O_3/g Al_2O_3) could provide 420 μmol/g of oxygen from reduction of Fe_2O_3. Since the reduction conditions used in our measurements were relatively mild, it is not surprising that we did not achieve complete

reduction of Fe_2O_3. However, the experiment demonstrates that a very large fraction of the Fe_2O_3 could be reduced.

3.4 Discussion

The work here demonstrates that ALD can be used to prepare high-surface-area, functional oxides for application as porous, catalytic materials by a static deposition system. The Fe_2O_3 deposited on Al_2O_3 in the present study appears to form dense, conformal films. The fact that the films remain invisible to XRD to very high temperatures, even for loadings greater than 40-wt% Fe_2O_3, suggests that these films are also thermally stable. The low specific rates we observed for the WGS reaction seem to indicate that the structure and properties of ALD-prepared oxide films can be different from that of the bulk oxides. However, given that commercial WGS catalysts are promoted with additional additives, it is very likely that the thin film oxides could be modified to increase their activity.

Table 3.1. Pore Size from N_2 Isotherm in the Nanopore Region as a function of ALD Cycles after the samples were heated to 773 K.

Number of ALD Cycles	Nanopore Size (nm)
0	9.56
10	9.59
20	9.26
40	8.47

It is important to recognize that the methods used in performing ALD can result in very different types of materials when the substrate is porous. Most previous studies have

used an inert carrier gas to provide contact between the substrate and the organometallic precursor [14]. Because gas-phase diffusion is a relatively slow process, this can result in concentration gradients. For non-porous powders, these concentration gradients can be reduced by performing the ALD in a fluidized bed [15]; however, most of the surface area in catalytic materials exists within small pores and gradients in these pores cannot be removed by fluidization. Exposing the substrate to the precursor and oxidant under static conditions largely eliminates these problems and allows the use of relatively large, high-surface-area samples. Static conditions also minimize the loss of potentially expensive organometallic precursor, since essentially all the precursor is used in the films and very little is lost during the evacuation cycle.

The nature of the oxide films is also different depending on how ALD is performed. Some previous reports of ALD films grown in porous materials have shown that the oxide films were porous [16,17]. While the production of nanopores may be desirable [18,19], it is clearly important to control the process. Exactly why ALD films are sometimes porous is uncertain and may not always be the same. Simple shrinkage of low-density films is likely responsible for pores in many cases. However, in at least one example where porous ZrO_2 films were produced, the observed growth rates were unexpectedly high, greater than 0.5-nm per cycle [17]. Using the same organometallic precursor, the ZrO_2 growth rate observed by some on CeO_2 [20] and Al_2O_3 [21] substrates was only ~0.02 nm per cycle. It is unlikely that the higher growth rate was due to chemical vapor deposition (CVD), since the deposition temperature was not high and CVD would likely have resulted in thicker films near the external surface of the sample. An alternative possible explanation is that

excess precursor may condense on the porous substrate and then not be completely removed prior to the oxidation cycle due to slow diffusion of the precursor in the inert carrier. The exact reason for differences in the oxide-film morphologies remains unknown but the differences clearly demonstrate the need for a better understanding of the processes involved for ALD in porous materials.

The high thermal stability of oxide films prepared by ALD was observed here for Fe_2O_3 on Al_2O_3. In part, this is due to the relatively lower surface energy of oxides compared to metals. There may also be attractive interactions between the Al_2O_3 substrate and film. Assuming that is the case, it would be interesting to explore the effect of substrate composition on the stability and properties of the films. It may even be desirable to grow other interesting oxides such as CeO_2 on Al_2O_3, or multiple layers with different compositions such as Fe_2O_3 layers on CeO_2/Al_2O_3 substrates in which the CeO_2 was grown by ALD. These multilayer systems may allow one to build in specific chemical interactions between various oxides.

3.5 Conclusion

In the present study, we successfully demonstrated the growth of Fe_2O_3 films by Atomic Layer Deposition (ALD) on high-surface-area γ-Al_2O_3 using our home-built static deposition system. The sample mass was found to increase almost linearly with the number of ALD cycles at lower coverages, with a growth rate corresponding to 0.016 nm per cycle. Surface-area and pore-size-distribution measurements, along with TEM-EDS mapping, were consistent with formation of dense, conformal films on the Al_2O_3. Relevant film

thicknesses are limited to 0.3 to 1.0-nm as thicker films led to blockage of pore entrances and a significant decrease in specific surface area. The catalytic properties for the water-gas-shift reaction were different from that of bulk Fe_2O_3 but the films were reducible and could be promoted to provide high activity by addition of Pd. The results demonstrate that ALD can be an important tool for catalyst synthesis, and it can be applied for producing novel catalytic materials.

3.6 References

1. Jen, H.-W.; Graham, G.; Chun, W.; McCabe, R.; Cuif, J.-P.; Deutsch, S.; Touret, O., *Catal. Today* **1999,** *50*, 309-328.

2. Sugiura, M., *Catal. Surveys from Asia* **2003,** *7*, 77-87.

3. Rhodes, C.; Hutchings, G. J., *Phys. Chem. Chem. Phys.* **2003,** *5*, 2719-2723.

4. Zhang, L.; Wang, X.; Millet, J.-M. M.; Matter, P. H.; Ozkan, U. S., *Appl. Catal. A.* **2008,** *351*, 1-8.

5. Basińska, A.; Domka, F., *Catal. Lett.* **1993,** *17*, 327-332.

6. Basińska, A.; Nowacki, A.; Domka, F., *React. Kin. and Catal. Lett.* **1999,** *66*, 3-11.

7. Zhao, S.; Gorte, R. J., *Catal. Lett.* **2004,** *92*, 75-80.

8. Ratnasamy, C.; Wagner, J. P., *Catal. Rev.* **2009,** *51*, 325-440.

9. Baldychev, I.; Vohs, J. M.; Gorte, R. J., *Appl. Catal. A.* **2009,** *356*, 225-230.

10. Popa, T.; Xu, G.; Barton, T. F.; Argyle, M. D., *Appl. Catal. A.* **2010,** *379*, 15-23.

11. Martinson, A. B.; DeVries, M. J.; Libera, J. A.; Christensen, S. T.; Hupp, J. T.; Pellin, M. J.; Elam, J. W., *J. Phys. Chem. C.* **2011,** *115*, 4333-4339.

12. Rooth, M.; Johansson, A.; Kukli, K.; Aarik, J.; Boman, M.; Hårsta, A., *Chem. Vap. Dep.* **2008,** *14*, 67-70.

13. Zhu, M.; Wachs, I. E., *ACS Catal.* **2015,** *6*, 722-732

14. O'Neill, B. J.; Jackson, D. H.; Lee, J.; Canlas, C.; Stair, P. C.; Marshall, C. L.; Elam, J. W.; Kuech, T. F.; Dumesic, J. A.; Huber, G. W., *ACS Catal.* **2015,** *5*, 1804-1825.

15. King, D. M.; Spencer, J. A.; Liang, X.; Hakim, L. F.; Weimer, A. W., *Surf. Coat. Technol.* **2007,** *201*, 9163-9171.

16. Li, T.; Karwal, S.; Aoun, B.; Zhao, H.; Ren, Y.; Canlas, C. P.; Elam, J. W.; Winans, R. E., *Chem. Mater.* **2016,** *28*, 7082-7087.

17. Chen, Y.; Gerdes, K.; Song, X., *Sci. Rep.* **2016,** *6*, 32997.

18. Lu, J.; Fu, B.; Kung, M. C.; Xiao, G.; Elam, J. W.; Kung, H. H.; Stair, P. C., *Science* **2012,** *335*, 1205-1208.

19. O'Neill, B. J.; Jackson, D. H.; Crisci, A. J.; Farberow, C. A.; Shi, F.; Alba-Rubio, A. C.; Lu, J.; Dietrich, P. J.; Gu, X.; Marshall, C. L., *Angewandte Chemie* **2013,** *125*, 14053-14057.

20. Onn, T. M.; Zhang, S.; Arroyo-Ramirez, L.; Chung, Y.-C.; Graham, G. W.; Pan, X.; Gorte, R. J., *ACS Catal.* **2015,** *5*, 5696-5701.

21. Onn, T. M.; Zhang, S.; Arroyo-Ramirez, L.; Xia, Y.; Wang, C.; Pan, X.; Graham, G. W.; Gorte, R. J., *Appl. Catal. B.* **2017,** *201*, 430-437.

CHAPTER 4. PREPARATION OF HIGH-SURFACE AREA CERIA BY ATOMIC LAYER DEPOSITION ON ALUMINA

Summary:

High-Surface area Ceria (CeO_2) film was prepared by Atomic Layer Deposition (ALD) on γ-Al_2O_3 to produce a composite catalyst supports for Pd. The weight of the support was found to increase linearly with the number of ALD cycles. This, together with TEM images, indicated that the CeO_2 grows as a dense, conformal film, with a growth rate of 0.02 nm per cycle. The films showed good thermal stability under oxidizing conditions. XRD measurements on a sample with 0.28 g CeO_2/g Al_2O_3 showed no evidence for crystalline CeO_2 until calcination above 1073 K. Water-gas-shift (WGS) rates on 1-wt% Pd catalysts supported on the CeO_2 ALD-modified Al_2O_3 were essentially identical to rates on conventional Pd-CeO_2 catalysts and much higher than rates on a catalyst in which Pd was supported on Al_2O_3 with CeO_2 added by infiltration. When calcined to 1073 K, the Pd supported on the ALD-modified support retained its WGS reaction rates while the rates for the two Pd-supported conventional supports decreased significantly. The WGS rates, together with results from FTIR and CO-O_2 pulse studies, suggest that all the Pd is in contact with CeO_2 on the ALD-prepared supports and that it should be possible to prepare high-surface-area, functional supports using ALD.

[*This chapter was published as a research paper in the Applied Catalysis B, 201 (2017) 430-437. Copyright: 2017, Elsevier.*]

4.1 Introduction

Ceria is the material of choice as an Oxygen Storage Capacitor (OSC) in automotive, three-way catalysts due to its ability to undergo facile oxidation and reduction [1,2]. These redox properties are also responsible for promotion of rates on ceria-supported metals for the CO-oxidation [3], water-gas-shift [4], methane-steam-reforming [5], and methane-oxidation [6] reactions. For CO oxidation, the rate enhancements were shown to depend on the interfacial contact between the ceria and the metal [7], implying that direct contact between the two phases is essential. Unfortunately, the stability of ceria is a problem. In automotive applications, ceria readily crystallizes and sinters, "with growth of particles and loss of surface area, leading to rapid reduction of the oxygen storage and release properties" [8]. Hydrothermal aging and the resulting increase in ceria crystallinity has also been shown to change the thermodynamics of CeO_2 reduction, increasing the magnitude of the heat of oxidation by as much as 50% [9].

Various strategies are used to stabilize the ceria component. First, the OSC component in three-way catalysts is always in the form of a CeO_2-ZrO_2 mixed oxide [10]. These mixed oxides still lose most of their surface area after thermal treatments [11] but the mixed oxides remain thermodynamically reducible. The heats of oxidation for CeO_2-ZrO_2 mixed oxides do not significantly change with particle size or surface area [12,13]. However, a high surface area for the ceria component is still important for maintaining contact with the transition metal. One strategy to stabilize the surface area of the OSC component involves incorporating alumina particles as diffusion barriers to prevent contact between adjacent CeO_2-ZrO_2 particles [8]. This approach has been shown to be effective

in maintaining surface areas but introduces difficulties in that the supported metals may not be in contact with the ceria-containing component.

In the present work, we set out to synthesize a composite support of ceria on high-surface-area Al_2O_3 using Atomic Layer Deposition (ALD). While conventional infiltration of Al_2O_3 with $Ce(NO_3)_3$ solutions, followed by heating to decompose the nitrate ions, forms CeO_2 crystallites that cover only a fraction of the surface, ALD is in principle capable of forming uniform, atomic-scale films that cover the entire Al_2O_3 surface. This morphology maximizes the interfacial contact between ceria and any metal catalyst that is introduced to the support. The Al_2O_3 could also stabilize the ceria surface area and prevent crystallite growth, depending on the relative interfacial energies between CeO_2 and Al_2O_3. We will also show that this composite support has similar catalytic properties to what would be expected for a high-surface-area CeO_2 support, but with better stability.

4.2 Experimental Methods

Atomic Layer Deposition (ALD) of CeO_2 was performed using the home-built deposition system that was described in Chapter 2. Tetrakis (2,2,6,6-tetramethyl-3,5-heptanedionato) cerium ($Ce(TMHD)_4$, Strem Chemicals) was selected as the precursor to deposit CeO_2 film due to its thermal stability. The procedure for successful ALD was described in Chapter 2. The solid organometallic precursor was heated to 453 K to produce a vapor pressure of approximately 2 to 5 Torr. During the deposition cycle, the $Ce(TMHD)_4$ vapor was introduced to the evacuated sample chamber containing approximately 0.5-g γ-Al_2O_3. The substrate was exposed to the precursor vapor at 503 K for 300 s. Multiple

exposure to the precursor vapor was carried out to ensure that the reaction with the surface was complete. Because a previous study showed that the $Ce(TMHD)_4$ precursor may not be completely oxidized at 503 K [14], in the present study, we removed the sample from the ALD system after evacuation and then heated it to 673 K in a muffle furnace for 5 min between exposures to the $Ce(TMHD)_4$ precursor. A total of 20 ALD cycles was carried out on the Al_2O_3 substrate.

To characterize film growth during ALD, the support was weighed after every 5 ALD cycles. The elemental composition of the sample was confirmed by ICP-OES (See Chapter 2 for full procedure). To benchmark the properties of this composite support, catalysts were also prepared using the unmodified Al_2O_3, the same Al_2O_3 with 0.28 g CeO_2/g Al_2O_3 added by infiltration with aqueous solutions of $Ce(NO_3)_3 \cdot 6H_2O$ (Referred to here as $CeO_2(IMP)/Al_2O_3$.), and a bulk CeO_2 powder. The $CeO_2(IMP)/Al_2O_3$ was calcined to 673 K for 6 h to remove any nitrates. The CeO_2 powder was prepared as described in Chapter 2. All 1-wt% Pd catalysts were prepared by incipient wetness using an aqueous solution of tetraaminepalladium (II) nitrate (Sigma Aldrich).

Pd dispersions, BET surface area measurements, XRD, STEM, and FTIR were used to characterize the samples. Steady-state WGS reaction was used to probe the activity of the Pd-supported samples. The flow reactor setup was described in Chapter 2. The partial pressures of CO and H_2O were both at 25 Torr (3.3-vol.%). The total flow rate of He was kept at 60 mL/min. Before testing, each sample was activated by heating the catalysts to 673 K in the reaction mixture before cooling back to the desired reaction temperature. The light-off profile CO-oxidation rates were also determined in the same flow reactor with CO

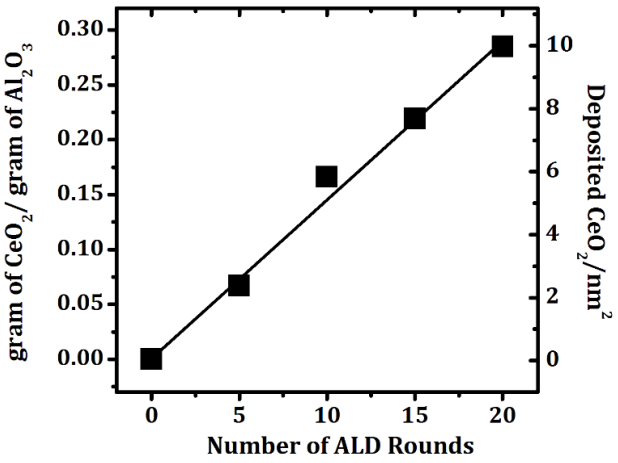

FIG. 4.1. Mass change as a function of the number of CeO_2 ALD cycles on an Al_2O_3 support which had an initial surface area of 130 m^2/g.

and O_2 being 25 and 12.5 Torr, respectively, and the balance being He. The total flow rate of the gas mixture was maintained at 120 mL min^{-1}. The samples tested for CO oxidation were previously heated to 1073 K in air before testing. The mass of catalyst used in every rate measurement was 0.10 g. Transient, pulse experiments were performed using procedure described in Chapter 2. No attempt was made to analyze the shapes of the pulses because coupling between desorption, re-adsorption, reaction, and diffusion does not allow for a unique determination of rate processes in transient experiments of this type.

4.3 Results

4.3.1 Characterization of CeO_2 Film on Al_2O_3

The growth rates for the CeO_2 films on Al_2O_3 were determined gravimetrically by measuring the sample mass after every 5 ALD cycles, with results shown in Figure 4.1. The sample weight increased linearly with the number of cycles, and after 20 ALD cycles, the sample (Referred to here as $20CeO_2$-Al_2O_3) had a total weight gain of approximately

0.28 g CeO_2/g Al_2O_3. This weight increase by CeO_2 was confirmed by ICP analysis. Assuming that ceria forms a uniform, dense film with the bulk properties of CeO_2 over the 130-m^2/g Al_2O_3 surface, a 0.28 g CeO_2/g Al_2O_3 loading of CeO_2 corresponds to a film thickness of 0.4 nm ((0.28 g CeO_2/g Al_2O_3) x (1 cm^3/7.21 g CeO_2) x (1 g Al_2O_3/130 m^2) x (1 m^2/10^4 cm^2) x (10^7 nm/cm)). The growth rate calculated from this loading, 0.02 nm/cycle, is identical to the value that has been reported in the literature for this precursor on flat substrates [15].

In order to verify the presence of a thin CeO_2 film, high angle annular dark field (HAADF) STEM imaging was used to characterize the 20CeO_2-Al_2O_3 sample, as shown

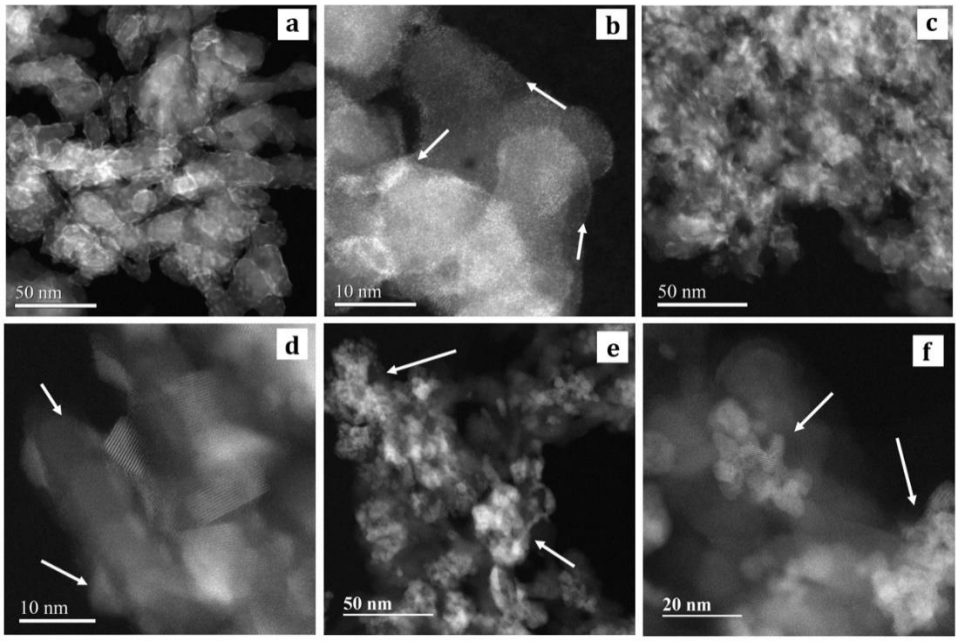

FIG. 4.2. High angle annular dark field STEM image of ALD 20CeO_2-Al_2O_3 sample after calcination at 673 K (a-b) and 1073 K (c-d), showing that the uniform atomic CeO_2 layer made through ALD deposition evolved into a mixture of 5-nm CeO_2 particles and CeO_2 film after 1073 K calcination. Impregnated samples after calcination at 673 K (e-f) are shown for comparison. CeO_2 particles appear in agglomerates, ~20-nm in size, and do not cover the surface uniformly. Arrows indicate the location of CeO_2, which appears as the brighter features in all six images.

in Figure 4.2 (a) through (d). Due to the atomic number difference between Ce and Al, CeO_2 appears brighter so the surface layer is distinguishable. The images in Figure 4.2(a) and 4.2(b) were obtained on the fresh sample calcined at 673 K and show that the Al_2O_3 is covered uniformly by CeO_2 film with a thickness close to the expected 0.4-nm. Not surprisingly for deposition on curved surfaces, some slightly larger CeO_2 particles are observed at the higher magnification. The images in Figures 4.2(c) and 4.2(d) show the same sample after calcination to 1073 K. Under low magnification, Figure 4.2(c), the entire surface of the support still appears to be covered with CeO_2. However, small particles, less than 5-nm in size, were also observed at high magnification, Figure 4.2(d), along with areas that still show the presence of a CeO_2 film.

The morphology of the $20CeO_2$-Al_2O_3 sample was clearly different from that of the CeO_2(IMP)/Al_2O_3 sample, obtained by infiltration with aqueous solutions $Ce(NO_3)_3$ onto the same Al_2O_3. The images in Figures 4.2(e) and 4.2(f) were obtained on CeO_2(IMP)/Al_2O_3, which had the same weight loading of CeO_2, after calcination to 673 K. The images show that the CeO_2 exists as 20-nm clusters of roughly 3-nm particles, even after this low calcination temperature. Furthermore, most of the Al_2O_3 remains uncovered by CeO_2. It should be acknowledged that we did not attempt to optimize the impregnation procedure to maximize the CeO_2 dispersion.

XRD patterns of the $20CeO_2$-Al_2O_3 sample are shown as a function of calcination temperature in Figure 4.3, together with the pattern for the untreated Al_2O_3, Figure 4.3(a) and the pattern for the CeO_2(IMP)/Al_2O_3 sample, Figure 4.3(e). First, it is worth noting that the diffraction pattern of the infiltrated sample with the same CeO_2 loading and calcined to

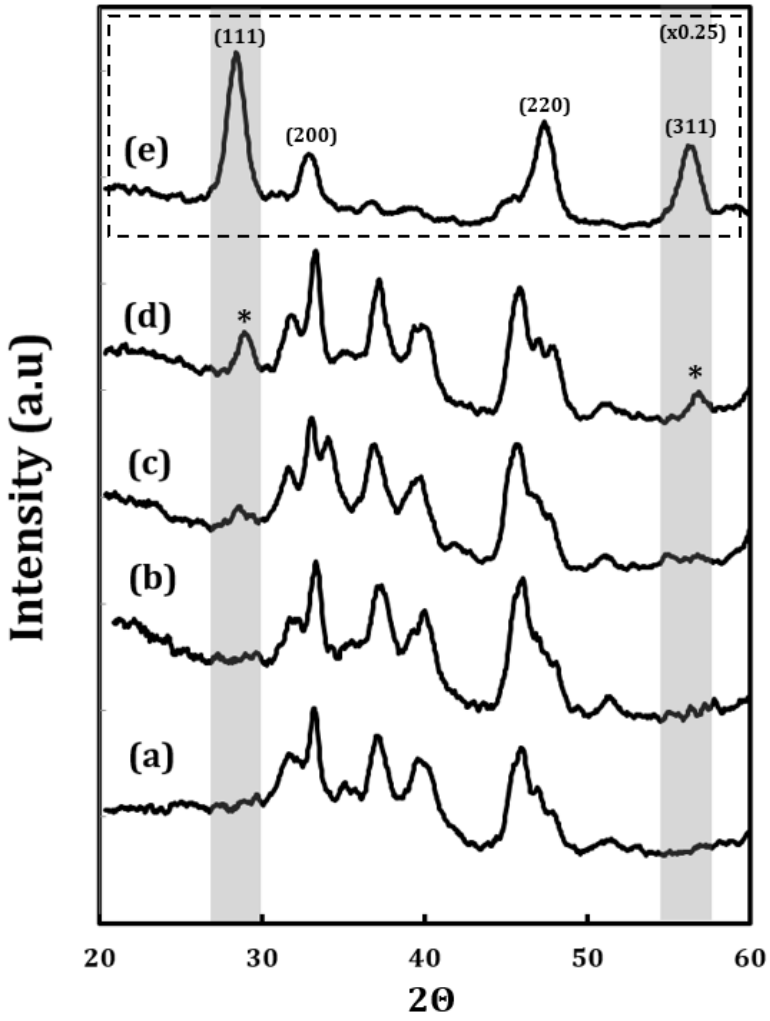

FIG. 4.3. XRD patterns of the (a) uncoated Al_2O_3 support heated to 1173 K and the ALD-coated, $20CeO_2$ -Al_2O_3 sample after calcination to the following temperatures: (b) 873 K; (c) 1073 K; and (d) 1173 K. The pattern in (e) was obtained on CeO_2(IMP)/Al_2O_3 heated to 673 K. Characteristic peaks for CeO_2 are marked by the grey line and *. Peaks were normalized to a distinct Al_2O_3 peak at $2\Theta = 46^o$, and the image (e) was scaled by x 0.25.

only 673 K, Figure 4.3(e), is very different. The peaks associated with CeO_2 dominate on CeO_2(IMP)/Al_2O_3, to the point that the peaks from Al_2O_3 are difficult to see on the same scale due to the larger X-Ray scattering cross section for Ce compared to Al. Even for this relatively low calcination temperature, the CeO_2 domain size, calculated using the Scherrer Equation and the peak width at 28 degrees 2θ, was already 10 nm. By comparison, there is no evidence for the presence of CeO_2 in the 20CeO_2-Al_2O_3 from the diffraction results after calcination at 873 K, Figure 4.3(b). This is consistent with the fact that the domain size for ceria in these samples is very small. Features associated with CeO_2 begin to appear near 28 and 58 degrees 2θ in the diffraction pattern of the sample calcined to 1073 K, Figure 4.3(c), and become more prominent after calcination at 1173 K, Figure 4.3(d). However, the intensity of the CeO_2 peaks remains weak, implying that much of the CeO_2 is not contributing. Based on diffraction peak widths, the crystallite size of CeO_2 particles was only 8 nm, even after calcination to 1173 K.

Table 4.1: BET Surface Area as a function of Calcination Temperature. The surface area of the Alumina support is 130 m^2/g.

	BET Surface Area (m^2/g)		
Calcination Temperature (K)	**Pd/CeO_2**	**Pd/20CeO_2-Al_2O_3**	**Pd/CeO_2 (IMP)/Al_2O_3**
773	42	82	110
973	30	78	100
1073	18	84	100

4.3.2. Catalytic Properties of Ceria Film

To determine how modification of the Al_2O_3 support by CeO_2 ALD affects the catalyst-support properties, we examined a series of 1-wt% Pd catalysts prepared from the unmodified Al_2O_3, from the CeO_2 powder, from the CeO_2(IMP)/Al_2O_3 sample, and from the 20CeO_2-Al_2O_3 sample. It is first interesting to compare the BET surface areas of 1-wt Pd/CeO_2 powder and 1-wt% Pd/20CeO_2-Al_2O_3 as a function of calcination temperature. These results are reported in Table 4.1. Because the γ-Al_2O_3 used here was initially heated to 1173 K, its surface area was only 130 m^2/g. The addition of 20 cycles of CeO_2 by ALD and of 1-wt% Pd by infiltration reduced this to 82 m^2/g. Most of this decrease in specific surface area can be accounted for by the addition of 0.28-g CeO_2 and 0.01-g Pd per gram of catalyst (130 m^2/1.29 g = 100 m^2/g). The additional decrease in specific surface area is likely due to a decreased average pore diameter as the pores of the Al_2O_3 are coated with a nonporous, 0.4-nm film. Calcination of this sample to 1073 K had essentially no effect on the surface area. By contrast, the specific surface area of the Pd/CeO_2 powder decreased from 46 m^2/g after calcination to 673 K, to 42 m^2/g at 773 K and 18 m^2/g at 1073 K.

Table 4.2: Dispersion Measurement as a function of Calcination Temperature

	Pd Dispersion (%)		
Calcination Temp (K)	**Pd/CeO_2**	**Pd/20CeO_2-Al_2O_3**	**Pd/Al_2O_3**
773	40	65	34
973	35	63	30
1073	30	59	24

Pd dispersion measurements were also performed as a function of calcination temperature on the Pd/Al_2O_3, Pd/CeO_2, and $Pd/20CeO_2$-Al_2O_3 samples, with results shown Table 4.2. The data indicate that there was a fairly significant loss of Pd dispersion with calcination temperature on the Pd/Al_2O_3 sample, from 34% after 773 K and 24% after 1073 K. Given the significant loss in total surface area of Pd/CeO_2, the decrease in dispersion from 40% to 30% in this temperature range is small, indicating that CeO_2 likely helps maintain dispersion [16]. The Pd dispersion on $Pd/20CeO_2$-Al_2O_3 was 65% following catalyst treatment at 773 K and did not change significantly with calcination.

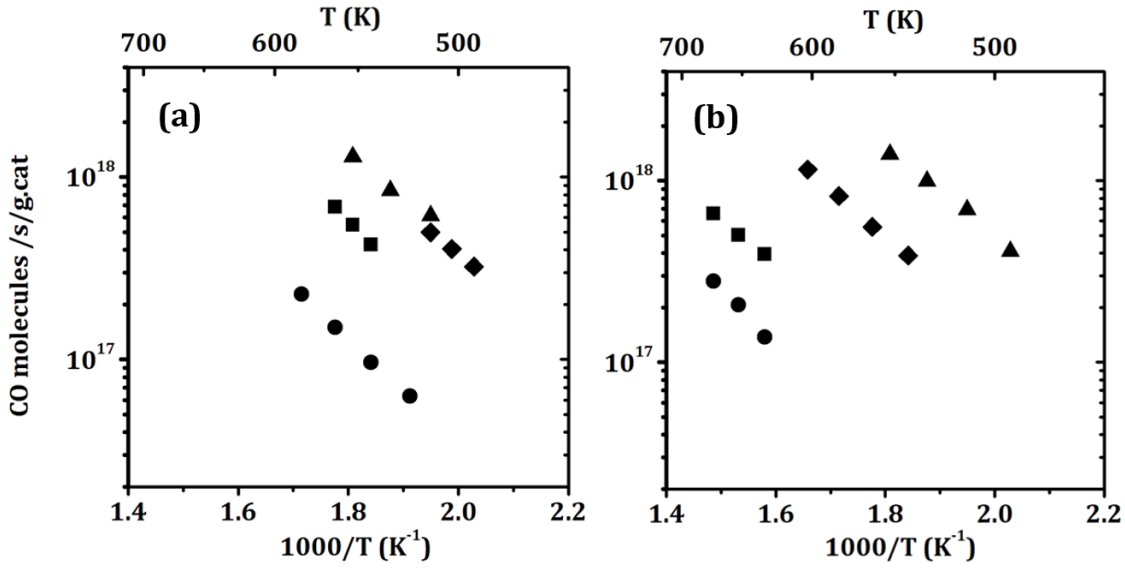

FIG. 4.4. Steady-state, differential reaction rates for water gas shift (WGS) reaction with partial pressure of CO and H_2O both at 25 Torr. WGS rates after pretreatment calcination to (a) 773 K and (b) 1073 K were compared for the following catalysts: (▲) – $Pd/20CeO_2$-Al_2O_3 (♦) – Pd/CeO_2, (■) Pd/CeO_2 (IMP) /Al_2O_3, and (●) – Pd/Al_2O_3.

It has been suggested that sites of contact between Pd and ceria are especially active for the WGS reaction due the ability of reduced ceria to be oxidized by water, then transfer

either oxygen or OH to CO that is adsorbed on the Pd [4]. Based on this picture, WGS rates provide information about whether Pd is in contact with CeO_2 in composite materials. Therefore, differential WGS rates were measured for the Pd/20CeO_2-Al_2O_3, Pd/CeO_2, Pd/Al_2O_3 and Pd/CeO_2(IMP)/Al_2O_3 catalysts. The data obtained following calcination of the catalysts to 773 K are shown in Figure 4.4(a). Rates on Pd/CeO_2 were almost 10 times higher than those on Pd/Al_2O_3, as expected. What is more interesting is that the differential rates on Pd/CeO_2 were nearly indistinguishable from rates on Pd/20CeO_2-Al_2O_3. Because the ALD-prepared sample is completely covered with CeO_2, its catalytic properties are nearly identical to those of a conventional CeO_2-supported catalyst. Since the Pd dispersions on Pd/CeO_2 and Pd/20CeO_2-Al_2O_3 are also reasonably close for 773-K calcination, the number of contact sites between Pd and ceria are also similar. Rates on Pd/CeO_2(IMP)/Al_2O_3 are approximately 2 times lower, probably because some of the Pd particles are not in contact with CeO_2.

Larger differences in the WGS rates were observed between the samples after the samples were calcined at 1073 K, as shown in Figure 4.4(b). Most significantly, rates on the Pd/20CeO_2-Al_2O_3 sample remain unchanged. This is consistent with the observations that increased calcination temperature did not affect either the surface area or the Pd dispersion. The fact that the rates remain unchanged implies that contact between Pd and ceria also remains good. Rates on Pd/CeO_2 decreased by a factor of about three after heating to higher temperatures, an amount that is too large to be explained entirely by the lower Pd dispersion. Because loss in ceria surface area is associated with an increase in crystallite size and larger ceria crystallites are considered to be less reducible, it is possible

that the decrease in rates is associated with a change in the ceria reducibility. An even larger drop in rates occurs with the $Pd/CeO_2(IMP)/Al_2O_3$ sample, possibly due to a loss in interfacial contact between the Pd and the ceria component of the support.

To further probe the catalytic properties of these catalysts, we measured light-off rates for CO oxidation on the $Pd/20CeO_2$-Al_2O_3, Pd/CeO_2 and Pd/Al_2O_3 samples after they had been calcined to 1073 K in air. These results are shown in Figure 4.5. The light-off temperatures correspond reasonably well with the relative WGS rates. The $Pd/20CeO_2$-Al_2O_3 sample was by far the most active, followed by the Pd/CeO_2 and Pd/Al_2O_3 samples. Again, the higher rates on $Pd/20CeO_2$-Al_2O_3 are an indication of good contact between Pd and ceria.

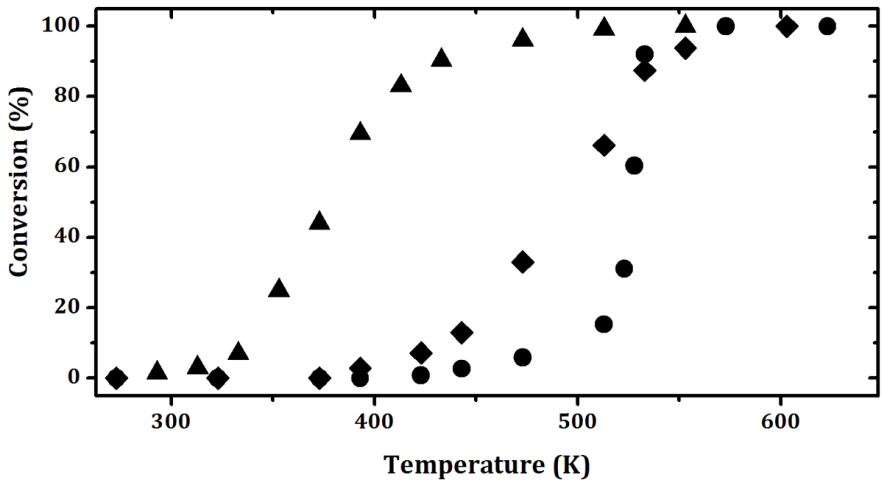

FIG. 4.5. Light-off curves of CO conversion versus temperature for: (▲) – $Pd/20CeO_2$-Al_2O_3, (♦) – Pd/CeO_2, and (●) – Pd/Al_2O_3 calcined at 1073 K. The CO oxidation reaction was carried out with partial pressures of CO and O_2 at 25 Torr and 12.5 Torr, respectively.

The redox properties of $Pd/20CeO_2$-Al_2O_3, Pd/CeO_2 and Pd/Al_2O_3 samples were probed using alternating CO and O_2 pulses at 673 K. Figure 4.6 shows a comparison of

results for the $Pd/20CeO_2$-Al_2O_3 and Pd/Al_2O_3 catalysts, while a summary of the quantities of oxygen that could be added and removed from the samples is reported in Table 4.3. In Figure 4.6, the regions between the dashed lines correspond to when either 10% O_2 (m/e = 32) or 10% CO (m/e = 28) was added to the He passing over the catalyst. The observation of CO_2 (m/e =44) upon exposure of the catalyst to CO is due to reduction of the catalyst. Formation of CO_2 during the O_2 pulse on $Pd/20CeO_2$-Al_2O_3, but not on Pd/Al_2O_3, sample is due to decomposition of carbonates that form on reduced ceria [17]. In the calculation of oxygen capacitance, the CO_2 from both the CO and O_2 pulses were added in determining the capacitance. A sample with 1-wt% Pd can provide 94 μmol/g of atomic oxygen by reduction of PdO. For bulk CeO_2, complete reduction to Ce_2O_3 removes 2900 μmol/g of oxygen. The amounts oxygen removed from the Pd/Al_2O_3 sample, 87 μmol/g of CO_2, are within experimental error of the amount expected. Results for $Pd/20CeO_2$-Al_2O_3 and Pd/CeO_2 were similar, forming 220 and 160 μmol/g of CO_2 respectively. In both cases, the ceria in contact with the Pd must be undergoing oxidation and reduction.

Table 4.3: Redox data for the pulse-reactor measurements performed at 673 K using CO-O_2 pulses over the samples.

	Average CO_2 (μmol/g) formed from CO Pulse
$Pd/20CeO_2$-Al_2O_3	220
Pd/CeO_2	160
Pd/Al_2O_3	87

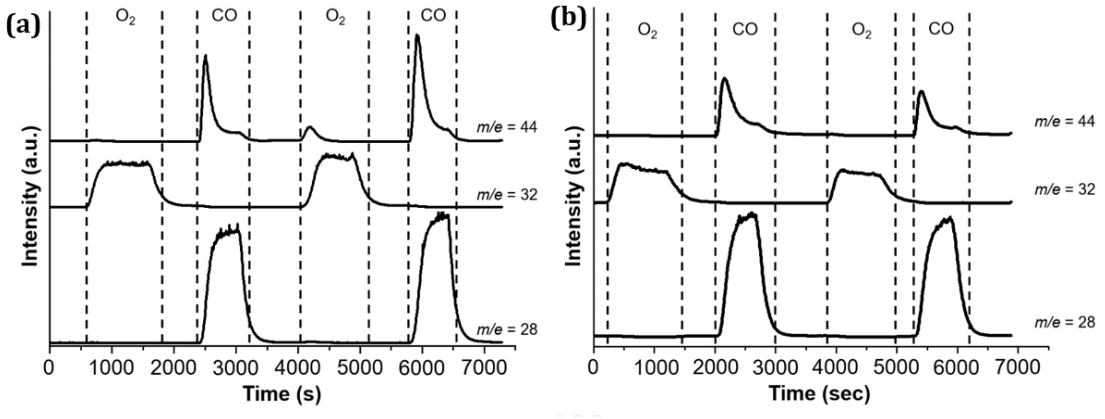

FIG. 4.6. Pulse measurements on a) Pd/20CeO_2-Al_2O_3, and b) Pd/Al_2O_3 catalysts at 673 K. The data are for two rounds of CO pulse (m/e = 28) and of O_2 pulse (m/e = 32). Formation of CO_2 (m/e = 44) is observed.

Finally, in order to compare the surface chemistry of 20CeO_2-Al_2O_3 and bulk CeO_2, we performed FTIR measurements on the Pd/ceria and Pd/20CeO_2-Al_2O_3 catalysts after they had been reduced in 10% CO-He mixtures. As mentioned above, this treatment is expected to reduce the ceria surface and form carbonates. As shown by the spectra in Figure 4.7, this is exactly what is observed on both samples. Both samples exhibit broad features between 1300 and 1700 cm^{-1} that correspond to the carbonates. Because absorption in the IR region is strong on bulk CeO_2, the spectrum on Pd/20CeO_2-Al_2O_3 is simpler. The results suggest that the ALD-modified sample could be a convenient, model system for spectroscopic characterization.

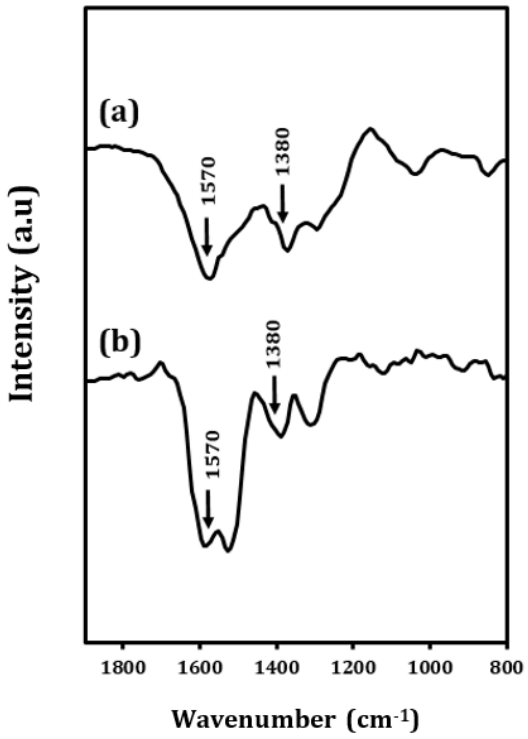

FIG. 4.7. DRIFTS spectra obtained for (a) Pd/CeO_2 and (b) $Pd/20CeO_2$-Al_2O_3, after exposure to 10% CO in flowing He at 573 K for 10 min.

4.4 Discussion

The present results indicate that it is possible to prepare a support material with the catalytic, promotional properties of ceria by depositing a thin conformal layer of CeO_2 onto a high-surface-area Al_2O_3 using ALD. When used as a support for Pd, the thin CeO_2 film has a similar effect on the water-gas-shift and CO-oxidation reactions as bulk CeO_2. The ALD-modified support has advantages over bulk ceria in that the underlying Al_2O_3 provides surface area for the CeO_2 and stabilizes that area to high-temperature calcination.

The thin-film, CeO_2-coated Al_2O_3 morphology would be difficult to achieve using conventional methods. With normal infiltration of Ce salts onto Al_2O_3, particles tend to form clusters during the drying or precipitation steps. Similarly, co-precipitation of alumina and ceria will tend to form a mixture of particles in which a large fraction of the surface will be Al_2O_3. As we have seen in the present study, these materials are not as effective as bulk CeO_2, probably because supported metals will distribute between the Al_2O_3 and CeO_2 phases. In this regard, ALD may be unique in providing this hierarchical structure.

The CeO_2 films that were formed by ALD showed surprising good thermal stability upon calcination. Even after calcination to 1173 K, the diffraction peaks for CeO_2 were weak compared to what was observed for a CeO_2/Al_2O_3 formed by infiltration with a similar CeO_2 loading. It is possible that spatial isolation is responsible for maintaining the small crystallites but surface energies may also be responsible. Although CeO_2 does not react with Al_2O_3, Ce^{+3} can form a $CeAlO_3$ perovskite structure. It is therefore possible that there could be bonding interactions at the CeO_2-Al_2O_3 interface. High-temperature reducing conditions could be a problem if compound formation were to occur.

Finally, it is interesting to note that the ALD approach for making "coated" supports is quite general and could be used to make other high-surface-area, functional supports. This opens up a number of opportunities. An obvious extension to the work in this present work would be to prepare CeO_2-ZrO_2, mixed-oxide films, which will be described in the next Chapter. While the mixed oxides are used in today's automotive catalysts, the surface areas are reported to drop below 2 m^2/g [18,19]. Maintaining a higher surface area could enhance the properties of the mixed oxide. In another example, researchers at Daihatsu

reported that perovskite-supported catalysts can exhibit very attractive properties [20,21]; however, because most perovskite powders have very low surface areas, it may not be possible to take full advantage of this fact. Preparation of a perovskite film on a support, which will be described in the following Chapter, could allow the attractive properties of the perovskite to be used to full advantage.

4.5 Conclusion

Deposition of CeO_2 by ALD can be used to form thin, conformal films on porous Al_2O_3, and the composites formed in this way can be used as catalyst supports for Pd. The supported-Pd catalysts prepared from the ALD-modified supports exhibit similar water-gas-shift rates to those obtained on conventional Pd/CeO_2 catalysts, implying that there is good contact between the Pd and the CeO_2. The ALD-prepared catalysts have much better thermal stability than conventional CeO_2 supports due to the underlying Al_2O_3. In addition, the concept of preparing functional catalysts supports by ALD is still in its infancy. However, we believe this approach could result in catalysts with improved performance and stability.

4.6 References

1. Gandhi, H.; Graham, G.; McCabe, R. W., *J. Catal.* **2003,** *216*, 433-442.

2. Shelef, M.; Graham, G. W.; McCabe, R. W., *World Scientific*: 2002; pp 343-375.

3. Bunluesin, T.; Putna, E.; Gorte, R., *Catal. Lett.* **1996,** *41*, 1-5.

4. Bunluesin, T.; Gorte, R.; Graham, G., *Appl. Catal. B* **1998,** *15*, 107-114.

5. Feio, L.; Hori, C.; Damyanova, S.; Noronha, F.; Cassinelli, W.; Marques, C.; Bueno, J., *Appl. Catal. A.* **2007,** *316*, 107-116.

6. Cargnello, M.; Doan-Nguyen, V. V.; Gordon, T. R.; Diaz, R. E.; Stach, E. A.; Gorte, R. J.; Fornasiero, P.; Murray, C. B., *Science* **2013,** *341*, 771-773.

7. Cargnello, M.; Jaén, J. D.; Garrido, J. H.; Bakhmutsky, K.; Montini, T.; Gámez, J. C.; Gorte, R.; Fornasiero, P., *Science* **2012,** *337*, 713-717.

8. He, B. J.-J.; Wang, C.-X.; Zheng, T.-T.; Zhao, Y.-K., *Johnson. Matthey Technol. Rev.* **2016,** *60*, 196-203.

9. Zhou, G.; Shah, P. R.; Montini, T.; Fornasiero, P.; Gorte, R. J., *Surf. Sci.* **2007,** *601*, 2512-2519.

10. Montini, T.; Melchionna, M.; Monai, M.; Fornasiero, P., *Chem. Rev.* **2016,** *116*, 5987-6041.

11. Morikawa, A.; Suzuki, T.; Kanazawa, T.; Kikuta, K.; Suda, A.; Shinjo, H., *Appl. Catal. B.* **2008,** *78*, 210-221.

12. Shah, P. R.; Kim, T.; Zhou, G.; Fornasiero, P.; Gorte, R. J., *Chem. Mater.* **2006,** *18*, 5363-5369.

13. Kim, T.; Vohs, J. M.; Gorte, R. J., *Ind. Eng. Chem. Res.* **2006,** *45*, 5561-5565.

14. Anthony, S. Y.; Küngas, R.; Vohs, J. M.; Gorte, R. J., *J. Electrochem. Soc.* **2013,** *160*, F1225-F1231.

15. Coll, M.; Gazquez, J.; Palau, A.; Varela, M.; Obradors, X.; Puig, T., *Chem. Mater.* **2012,** *24*, 3732-3737.

16. Jones, J.; Xiong, H.; DeLaRiva, A. T.; Peterson, E. J.; Pham, H.; Challa, S. R.; Qi, G.; Oh, S.; Wiebenga, M. H.; Hernández, X. I. P., *Science* **2016**, *353*, 150-154.

17. Wang, X.; Gorte, R. J.; Wagner, J., *J. Catal.* **2002,** *212*, 225-230.

18. Voorhoeve, R.; Johnson, D.; Remeika, J.; Gallagher, P., *Science* **1977,***195*, 827-833.

19. Singh, U. G.; Li, J.; Bennett, J. W.; Rappe, A. M.; Seshadri, R.; Scott, S. L., *J. Catal.* **2007,** *249*, 349-358.

20. Nishihata, Y.; Mizuki, J.; Akao, T.; Tanaka, H.; Uenishi, M.; Kimura, M.; Okamoto, T.; Hamada, N., *Nature* **2002,** *418*, 164-167.

21. Tanaka, H.; Tan, I.; Uenishi, M.; Kimura, M.; Dohmae, K., *Topics Catal.* **2001,** *16*, 63-70.

CHAPTER 5. ACTIVE AND STABLE HIGH-SURFACE AREA CERIA-ZIRCONIA SOLID SOLUTION FILMS PREPARED BY ALD ON ALUMINA AND THEIR THERMODYNAMIC PROPERTIES

Summary:

Ceria-zirconia, solid solutions were prepared as thin, dense films on a 130-m^2/g γ-Al_2O_3 by Atomic Layer Deposition (ALD) for use as catalyst supports. $Ce_{0.5}Zr_{0.5}O_2$ solid solution were grown by alternating between $Ce(TMHD)_4$ and $Zr(TMHD)_4$ precursors during ALD cycles. Different coverages of $Ce_{0.5}Zr_{0.5}O_2$ film were grown on γ-Al_2O_3. 50 ALD cycles resulted in a material with 0.77 g $Ce_{0.5}Zr_{0.5}O_2$ per g γ-Al_2O_3 (film thickness of 1.0 nm) while 20 ALD cycles resulted in a material with 0.24 g $Ce_{0.5}Zr_{0.5}O_2$ per g γ-Al_2O_3 (film thickness of 0.4 nm). The lattice parameter obtained from XRD on the higher coverage ALD sample was consistent with formation of a solid solution and scanning transmission electron microscopy (STEM) showed the mixed oxide was uniformly deposited. No XRD peak was observed from the lower coverage material, which could be in part due to the coherent length of the X-ray being unable to diffract the film. When impregnated with 1-wt% Pd, the ALD-prepared $Ce_{0.5}Zr_{0.5}O_2$-γ-Al_2O_3 and CeO_2-γ-Al_2O_3 catalysts showed CO-oxidation activity similar to Pd on bulk $Ce_{0.5}Zr_{0.5}O_2$ and CeO_2; however, the ALD-prepared sample maintained its surface area and catalytic activity when heated to temperatures up to 1273 K. Flow titration and coulometric titration revealed to understand the catalytic and thermodynamic properties of the CeO_2 and $Ce_{0.5}Zr_{0.5}O_2$ films. The redox properties of the ALD samples and bulk $Ce_{0.5}Zr_{0.5}O_2$ were measured by

determining the oxidation state of the ceria as a function of the H_2: H_2O ratio using flow titration and coulometric titration. The 20-wt% CeO_2 ALD film exhibited similar thermodynamics to that measured previously for a sample prepared by impregnation. However, the sample with 21-wt% $Ce_{0.5}Zr_{0.5}O_2$ on γ-Al_2O_3 reduced at a much higher P_{O_2} and showed evidence for transition between the $Ce_{0.5}Zr_{0.5}O_2$ and $Ce_{0.5}Zr_{0.5}O_{1.75}$ phases.

[*This chapter, in parts, was published as part of a research paper in the Catalysis Letters, 147 (2017) 1464-1470. Copyright: 2017, Springer.]*

5.1 Introduction

As described in the previous chapter, ceria plays an important role as oxygen-storage capacitors in automotive three-way catalysts. The critical property of ceria that makes it useful for this purpose and other catalytic applications is the relative ease with which it changes oxidation states between Ce^{3+} and Ce^{4+}. However, after harsh redox cycling, pure ceria powders become much more difficult to reduce and lose their promotional effect [1,2]. In three-way catalysts, the redox properties of ceria are stabilized by addition of zirconia to form ceria-zirconia solid solution [3,4]. Thermodynamically, ceria-zirconia solid solutions are more easily reduced than pure ceria [5-7]. They also maintain this reducibility after harsh redox cycling and in the high-temperature, hydrothermal environment of the automotive catalytic converter [3,6,7].

For many applications, loss of surface area remains an important issue with reducible oxides in catalysis. For example, after operation in a vehicle, ceria-zirconia mixed oxides typically have surface areas of only 2 m^2/g [2]. The common approach for achieving higher surface areas in materials that sinter easily is to incorporate the active component onto an inert support, like alumina [3]. However, depending on the preparation conditions, infiltration of ceria or ceria-zirconia mixtures onto a support can still result in materials in which the ceria-containing phase exists as larger particles, with most of the exposed surface being the inert support. An approach for preparing well-dispersed, uniform films on an oxide substrate is to use ALD. As a 1-nm film of dense CeO_2 on a 100-m^2/g support corresponds to a loading of 41-wt% CeO_2, only very thin films are needed or desired. As described in Chapter 4, uniform ceria films were successfully prepared on a γ-

Al_2O_3 support, resulting in a material that has catalytic properties similar to a high-surface-area ceria but the ceria films have surprisingly good thermal stability against sintering.

As the reducibility of ceria depends on the surface area and/or crystallite size and ceria-zirconia solid solutions are more reducible than pure ceria [1], this present work set out to investigate thin films of mixed-oxide prepared by ALD on a γ-Al_2O_3 support. Because the films prepared by ALD can be sub-nanometer in thickness, 0.02-nm per cycle, it is anticipated that the reducibility of these materials may be very different from even ordinary polycrystalline ceria. Quantification of reducibility can be difficult and kinetic measures, such as Temperature Programmed Reduction peak temperatures, can be dramatically affected by the presence of catalysts and other factors. Therefore, the reducibility will be quantified by measuring the thermodynamic properties of ALD-prepared films using flow titration and coulometric titration [1,8]. In both of these techniques, the sample is equilibrated at high temperatures in a specified P_{O_2} and the extent of ceria reduction (e.g. x in $CeO_{(2-x)}$) is then determined as a function of that P_{O_2} and temperature. The P_{O_2} is typically established by equilibrium with H_2 oxidation (i.e. $P_{O_2}^{½} = K_{\text{equi}}^{-1} \frac{P_{H_2O}}{P_{H_2}}$) and is therefore fixed by passing a mixture of H_2 and H_2O over the sample at a specified H_2O: H_2 ratio. Because the activity of solids is one, the equilibrium constant for oxidation of $CeO_{(2-x)}$, and therefore the free energy of oxidation at that value of x, is determine directly from the measured P_{O_2}. Furthermore, the temperature dependence of the equilibrium constant can be used to determine the heat of oxidation through the Clausius-Clapeyron Equation.

In the present study, we set out to investigate mixed-oxide films on a γ-Al_2O_3 support and its catalytic and thermodynamic properties. We will demonstrate that thin films of a ceria-zirconia solid solution can indeed be formed using ALD. The materials have catalytic properties similar to that of bulk ceria zirconia but they maintain their surface areas to much higher temperatures. In addition, we will compare the thermodynamic properties of ALD-prepared ceria-zirconia films with ceria films, which were described in Chapter 4. What we will show is that the ALD-prepared ceria films on γ-Al_2O_3 have thermodynamic redox properties that are different from that of bulk ceria but essentially identical to that reported previously for polycrystalline ceria formed by impregnation into γ-Al_2O_3. This may be due the film coalescing into particles upon redox cycling. By contrast, the ceria-zirconia films were stable and very different from either bulk ceria or ceria-zirconia solid solution. The films exhibit evidence for an equilibrium transition between the $Ce_{0.5}Zr_{0.5}O_2$ and $Ce_{0.5}Zr_{0.5}O_{1.75}$ phases.

5.2 Experimental Methods

5.2.1 Sample Preparation and Characterization

Samples were prepared by both ALD and conventional impregnation methods, using γ-Al_2O_3 (Strem Chemicals, Inc.) as a support that had been calcined at 1173 K and had a BET surface area of 130 m^2/g. The ALD-prepared samples were synthesized in a home-built apparatus described in Chapter 2. The ALD cycle consisted of exposing the γ-Al_2O_3 substrate to a few Torr of the organometallic precursors, either $Ce(TMHD)_4$ (Strem Chemicals, Inc.) or $Zr(TMHD)_4$ (Strem Chemicals, Inc.), at 503 K for ~300 s, followed by

evacuation to ~50 millitorr and precursor oxidation. It should be noted that the substrate was exposed to each gaseous precursor for multiple times to ensure surface saturation. The precursor oxidation was performed at 503 K for 300 s using an O_2 plasma generated by adding ~100 Torr of O_2 to the substrate chamber, followed by contacting a tesla coil to a Cu wire that was wrapped around the substrate chamber. To ensure that the ligands were completely oxidized, we removed each sample from the system after every 5 cycles and then heated it to 673 K in a muffle furnace for 5 min. Growth rates for both CeO_2 (0.016 nm/cycle) and ZrO_2 (0.024 nm/cycle) were determined by measuring the sample mass after every five cycles. The present study focused on a $CeO_2/\gamma\text{-}Al_2O_3$ made with 20 ALD cycles of ceria (20-wt% CeO_2, 20 CeO_2(ALD)/γ-Al_2O_3) and two different coverages of $Ce_{0.5}Zr_{0.5}O_2/\gamma\text{-}Al_2O_3$ made with 20 ALD cycles (12 ALD CeO_2 + 8 ALD ZrO_2, 21 wt.% $Ce_{0.5}Zr_{0.5}O_2$, 20 CZ(ALD)/γ-Al_2O_3) and 50 ALD cycles (30 ALD CeO_2 + 20 ALD ZrO_2, 53 wt.% $Ce_{0.5}Zr_{0.5}O_2$, 50 CZ(ALD)/γ-Al_2O_3).

Conventional alumina-supported catalysts containing 20-wt% CeO_2 (CeO_2(IMP)/γ-Al_2O_3) or 21-wt% of a CeO_2-ZrO_2 mixture (CZ(IMP)/γ-Al_2O_3) were prepared by infiltration with aqueous solutions of $Ce(NO_3)_3$•$6H_2O$ (Sigma Aldrich) or a mixture of $ZrO(NO_3)_2$•x H_2O (Sigma Aldrich, degree of hydration of fresh bottle ~ 6) and $Ce(NO_3)_3$•$6H_2O$. The samples were then dried at 333 K overnight, followed by calcination to 673 K for 6 h to remove the remaining nitrates. Bulk CeO_2 and bulk $Ce_{0.5}Zr_{0.5}O_2$ were prepared by ammonium hydroxide precipitation as described in Chapter 2. Samples containing 1-wt% Pd were prepared by incipient wetness using aqueous solutions of tetraaminepalladium(II) nitrate (Sigma Aldrich).

X-Ray Diffraction (XRD) patterns were recorded on a Rigaku Smartlab diffractometer equipped with a Cu Kα source (λ = 0.15416 nm). Crystalline graphite, physically mixed with the samples in a ratio of 1:8, was used as a reference for the peak positions in XRD. BET surface-area measurements, STEM and EDS, and CO chemisorption were used to characterize the samples. Steady-state rates for CO oxidation were measured under differential conditions in a flow reactor setup equipped with a GC as described in Chapter 2. The partial pressure for CO and O_2 were 25 Torr and 12.5 Torr O_2 respectively and the balance being He. The total flow rate of the gas mixture was maintained at 120 mL/ min.

5.2.2 Redox Equilibrium Measurements:

Equilibrium oxidation isotherms were obtained from ALD-prepared samples with low coverages (20 CeO_2(ALD)/γ-Al_2O_3 and 20 CZ(ALD)/ γ-Al_2O_3) by flow titration and coulometric titration, with both techniques described in further detail in Chapter 2. The flow titration experiments were performed in the following manner: 0.5 g of sample were placed in a quartz-tube flow reactor, exposed to dry flowing H_2 (30 mL/min) at the temperature of interest for 0.5 h, and then exposed to a flowing H_2-H_2O mixture (30 ml/min) for 1 h. The H_2-H_2O mixture was produced by passing H_2 through a temperature-controlled water bubbler, using the equilibrium vapor pressure to calculate the H_2O partial pressure. After purging the sample with dry He for 0.5 h, flowing air (21% O_2 and 79% N_2) was passed over the sample at a rate of 3.1 ml/min and the composition of the effluent gas was determined using a quadrupole mass spectrometer. The amount of oxygen required

to re-oxidize the sample was obtained by integrating the difference between the N_2 and O_2 signals. A typical result is shown in Figure 5.1. This in turn provides the oxidation state of the ceria that had been in equilibrium with the H_2-H_2O mixture.

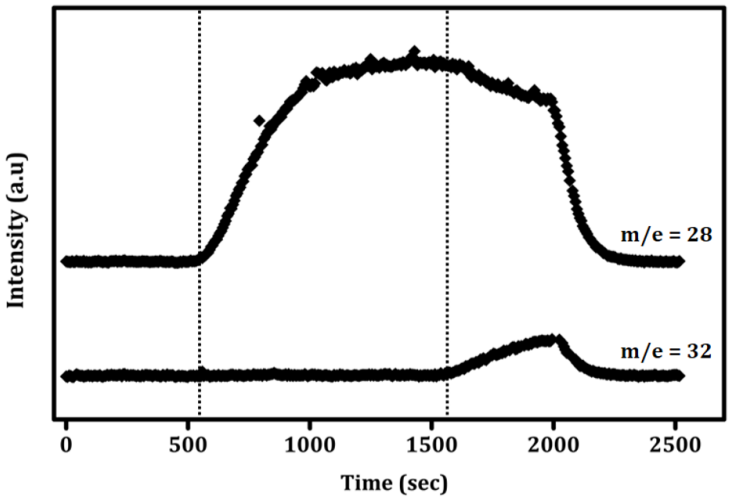

FIG. 5.1. Flow Titration Study of 20CeO_2-Al_2O_3 after reduction with pure H_2 at 973 K for 1 hour. The data are for signals for air, N_2 (m/e = 28) and O_2 (m/e = 32), titrated into the system. The amount of oxygen uptake is determined by length of time between the N_2 and O_2 signal.

Because the H_2-H_2O ratio can only be controlled over a limited range in flow titration, coulometric titration was also used to verify the flow-titration data and to extend the range of P_{O_2} equilibrium measurements [1,8]. In coulometric titration, a 0.5-g sample was inserted into a YSZ (yttria-stabilized zirconia) tube that had Ag electrodes painted on both inside and outside. The YSZ tube was then placed in a horizontal tube furnace and then heated to the temperature of interest, either 873 K or 1073 K, using a heating rate of 1.0 K/min. During the temperature ramp, a mixture of 5% O_2, 10% H_2O, and 85% Ar was allowed to flow over the sample at a flow rate of 110 ml/min in order to ensure that the sample was completely oxidized at the start of the measurements. After 1 h at the

temperature of interest, the flow was stopped and the ends of the YSZ tube were sealed with Cajon fittings. Specified amounts of oxygen were then electrochemically pumped from the inside of the YSZ tube by applying a current across the electrodes using a Gamry instruments potentiostat. After allowing the system to come to equilibrium with the electrodes at open circuit, the equilibrium P_{O_2} was calculated from the Nernst equation and the open circuit potential. To demonstrate equilibrium, oxidation isotherms were also measured starting with the reduced sample.

5.3 Results

5.3.1 Characterization of Materials

The individual growth rates ZrO_2 and CeO_2 were first determined gravimetrically by measuring the mass of the substrate after every 5 ALD cycles, with results shown in Figure 5.2(a) and 5.2(b). Each ALD cycle involved exposure of the sample to either $Zr(TMHD)_4$ or $Ce(TMHD)_4$ at 523 K, followed by oxidation at 773 K. For both ZrO_2 and CeO_2, the sample mass increased almost linearly with the number of cycles but the growth rates for the two oxides were slightly different on a molar basis. After 25 cycles, the ZrO_2 loading was 0.44 g ZrO_2/g Al_2O_3 (3.6 x 10^{-3} mole Zr/g Al_2O_3) and the CeO_2 loading was 0.38 g CeO_2/g Al_2O_3 (2.2 x 10^{-3} mole Ce/g Al_2O_3). Using the surface area of the γ-Al_2O_3 (130 m^2/g) and assuming that the films formed dense, bulk-like ZrO_2 and CeO_2, the growth rates for the individual oxides would be 0.024 nm/cycle and 0.016 nm/cycle, respectively. These values are close to values reported previously [9,10] and are reasonable based on the size of the ligands in the precursor molecules.

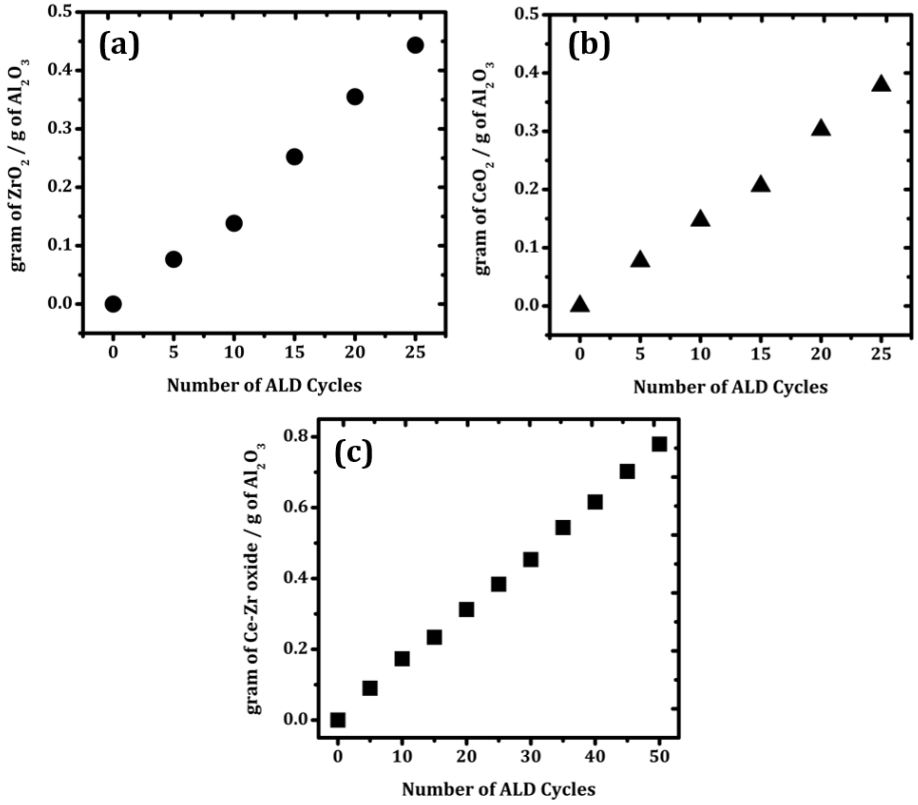

FIG. 5.2. The mass change of (a) (●) – ZrO_2, (b) (▲) – CeO_2, and (c) (■) – $Ce_{0.5}Zr_{0.5}O_2$ per gram of Al_2O_3 support as a function of the number of ALD cycles. The Al_2O_3 support has an initial surface area of 130 m^2/g. The mole ratio for the individual growth of Zr to Ce was approximately 3: 2. $Ce_{0.5}Zr_{0.5}O_2$ ALD was carried out with alternating 2 Zr ALD cycles to 3 Ce ALD cycles up to a grand total of 50 cycles.

Since the relative molar growth rates for Zr and Ce were in a ratio of roughly 3:2, an equimolar CeO_2-ZrO_2 film was grown using an alternating sequence of 2 ZrO_2 ALD cycles followed by 3 CeO_2 ALD cycles. The growth rate using this sequence was again linear with the number of cycles and is shown in Figure 5.2(c). After depositing 50 ALD cycles (20 cycles of ZrO_2 and 30 cycles of CeO_2), the mass change was 0.77 g/g Al_2O_3, a value close to what would be expected based on the growth rates of the individual oxides.

Assuming a density of 6 g/cm^3 for the mixed oxide, the film thickness after 50 cycles was approximately 1 nm.

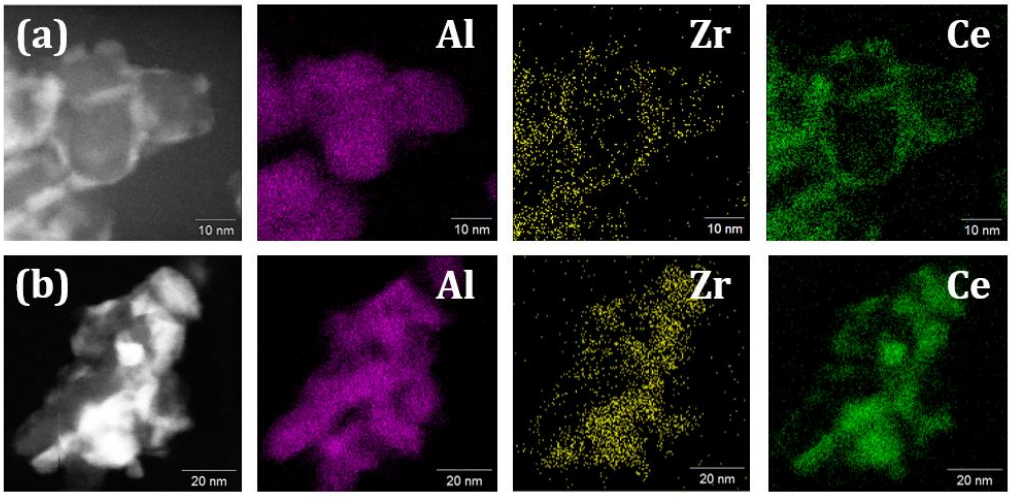

FIG. 5.3. High angle annular dark field STEM image of ALD 50$Ce_{0.5}Zr_{0.5}O_2$-Al_2O_3 after calcination at (a) 773 K, and (b) 1273 K. EDS mapping of Al, Ce, and Zr shows overlapping Ce and Zr signals at both temperature, as expected for a ceria-zirconia solid solution, but the distribution of the mixed oxide on the surface of the Al_2O_3 support is more uniform, as expected for a conformal coating, at the lower temperature.

High angle annular dark field (HAADF) STEM imaging and EDS elemental mapping were used to examine the sample with 50 ALD cycles of CeO_2-ZrO_2, with the results for a sample calcined at 773 K shown in Figure 5.3(a). Since the atomic number of Ce and Zr are greater than that of Al, the ceria-zirconia film appears as fairly uniform, bright edges at the surface of the Al_2O_3 support. EDS elemental maps for Al, Ce, and Zr also confirm that these bright edges are due to ceria-zirconia mixture since the Zr and Ce were localized along the edges of the Al_2O_3. The sample was also examined after calcination in air to 1273 K, with images shown in Figure 5.3(b). EDS maps show that Ce and Zr are still present over the entire sample. There is evidence for growth of larger ceria-

zirconia particles after this treatment, although it is difficult to assess what fraction of the CeO_2-ZrO_2 is part of this. Furthermore, it is important to recognize that the Al_2O_3 itself had never been heated to this high a temperature prior to deposition of CeO_2 and ZrO_2, so that film breakup is likely due to collapse of the underlying support, in addition to sintering.

Information on the phase of the ALD-prepared, CeO_2-ZrO_2, mixed oxide films can be gathered from the XRD patterns in Figure 5.4. All of the patterns have been normalized to the intensity of the graphite peak that was used as an internal standard, since all of the samples were mixed with graphite in a ratio of 8 parts sample to 1 part graphite. The pattern in Figure 5.4 (I, b) was measured on a sample with 0.31 g $Ce_{0.5}Zr_{0.5}O_2$/g of Al_2O_3 (12 ALD cycles of CeO_2 and 8 of ZrO_2, 20CZ(ALD)-Al_2O_3), calcined to 773 K. This pattern is indistinguishable from that of the Al_2O_3 substrate (Figure 5.4 (I, a)). Heating the sample to 1073 K showed evidence for a fluorite-related feature at 29.4 degrees 2θ on the ALD sample as shown Figure 5.4 (I, c); but the feature is very broad and weak, suggesting that the oxide is stable and it remains in the form of an amorphous film. The peak position, roughly half way between the expected angles for CeO_2 and ZrO_2, is consistent with formation of a solid, ceria-zirconia solution [11]. The very low XRD peak intensity is a general characteristic of oxide films prepared by ALD, even after high-temperature treatment, probably because the film thicknesses can be less than the X-Ray coherence length. The XRD pattern for the CeO_2-ZrO_2 mixed oxide prepared by impregnation with the same loading of $Ce_{0.5}Zr_{0.5}O_2$/g of Al_2O_3 is very different as shown in Figure 5.4 (I, d).

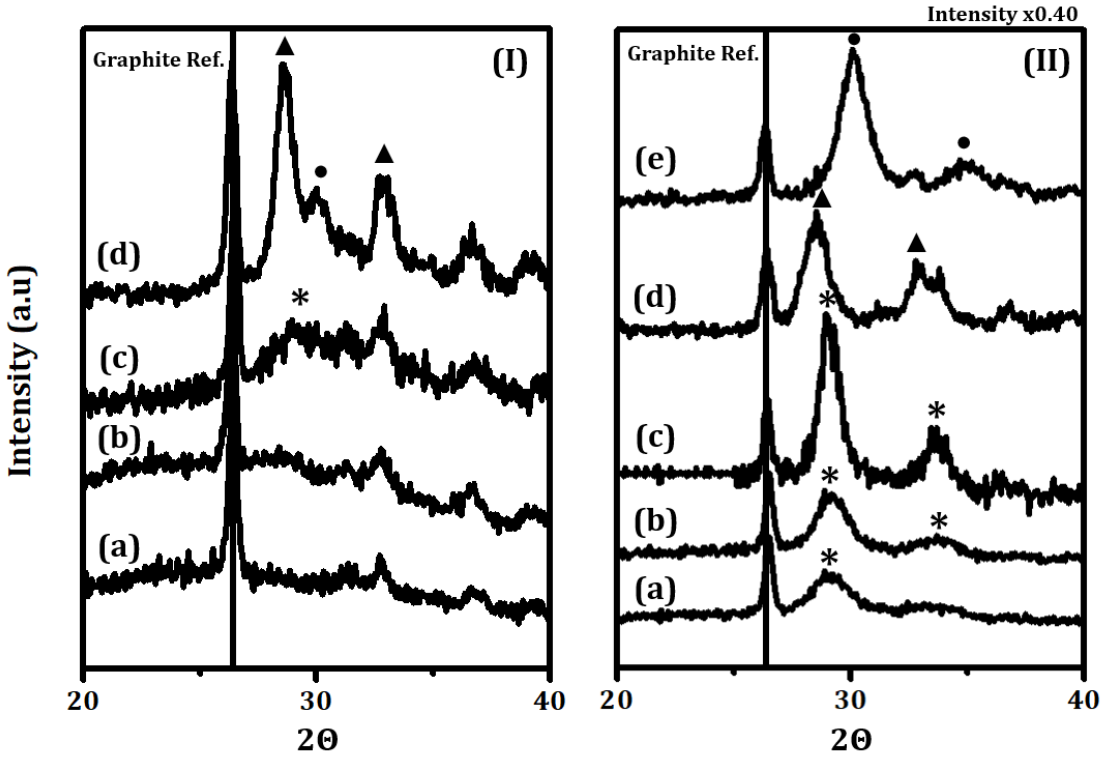

FIG. 5.4. XRD patterns of Ceria-Zirconia ALD on Al_2O_3 at two different coverages, (I) – 0.31 g $Ce_{0.5}Zr_{0.5}O_2$/g Al_2O_3 (20CZ(ALD)/γ-Al_2O_3) and (II) – 0.77 g $Ce_{0.5}Zr_{0.5}O_2$/g Al_2O_3 (50CZ(ALD)/γ-Al_2O_3). For (I), XRD patterns of (a) γ-Al_2O_3 support after calcination to 1173 K in air were compared against the 20CZ(ALD)/γ-Al_2O_3 heated to (b) 773 K and (c) 1073 K. The pattern in (d) was obtained from CZ(IMP)/Al_2O_3 heated to 773 K and contained the same material loading as the 20CZ(ALD)/γ-Al_2O_3. For (II), XRD patterns were obtained from 50CZ(ALD)/γ-Al_2O_3heated to (a) 773 K, (b) 1173 K, and (c) 1273 K. These patterns were compared to that of (d) 30CeO_2-Al_2O_3 and (e) 20ZrO_2-Al_2O_3 heated to 1273 K. All the peaks were normalized to a distinct graphite peak around 2Θ = 26.5° as shown by the solid line. Characteristic peaks for the $Ce_{0.5}Zr_{0.5}O_2$ are marked by * while peaks for CeO_2 and ZrO_2 are marked by ▲ and ● respectively. Patterns on (II) were scaled by x 0.40 for the sake of comparison with patterns on (I).

Because it is difficult to form a single-phase, ceria-zirconia solid solution by impregnation, the impregnated sample shows two features in this region, at approximately 28 and 30 degrees 2θ, which are due to ceria- and zirconia-rich phases, respectively [12]. Again, the

intensities of the peaks on CZ(IMP)/γ-Al_2O_3 are much greater, implying the presence of three-dimensional crystallites.

The pattern in Figure 5.4 (II, a) was measured on a ALD sample with a higher coverage of 0.77 g $Ce_{0.5}Zr_{0.5}O_2$/g of Al_2O_3 after calcination at 773 K. This pattern shows a broad band centered at 29.4 degrees 2θ begins to appear. This may be due to the film thickness being in a relevant length scale to the X-ray coherence length. This band grew in intensity when the calcination temperature was increased to 1173 K Figure 5.4 (II, b) and 1273 K (Figure 5.4 (II, c)). The peak position is roughly halfway between that observed for 1273-K calcined samples with 30 ALD cycles of CeO_2 (Figure 5.4 (II, d)) and 20 ALD cycles of ZrO_2 (Figure 5.4 (II, e)). The position of the peak for these higher loadings of mixed oxide prepared by ALD is also consistent with the ceria-zirconia mixture being in the form of a solid solution [11].

Table 5.1: BET Surface Area of the ALD Modified Support as a Function of Calcination Temperature

	BET Surface Area (m^2/g)	
Calcination Temperature (K)	**50CZ(ALD)-Al_2O_3**	**$Ce_{0.5}Zr_{0.5}O_2$**
773	83	55
1173	65	3
1273	63	0.5

5.3.2 Catalytic Properties of $CeZrO_4$ film

The catalyst-support properties of the $Ce_{0.5}Zr_{0.5}O_2$ film with 0.77 g $Ce_{0.5}Zr_{0.5}O_2$/g of Al_2O_3 prepared by 50 ALD cycles (50CZ(ALD)-Al_2O_3) were compared to that of bulk $Ce_{0.5}Zr_{0.5}O_2$ after each sample had been heated to 773 K, 1173 K, and 1273 K. The surface areas after each of these calcination treatments are shown in Table 5.1. After heating the ALD prepared support to 773 K, the specific surface area decreased from 130 m^2/g to 83 m^2/g. Simply increasing the sample mass with no other changes in sample morphology would decrease the surface area to 73 m^2/g (130 m^2 /1.77 g). The fact that the surface area of the 50CZ(ALD)-Al_2O_3 sample was slightly higher than this may indicate corrugation in the $Ce_{0.5}Zr_{0.5}O_2$ film. The surface area of this sample did not change dramatically with increasing calcination temperature, maintaining a surface area of 65 m^2/g after 1173 K and 60 m^2/g after 1273 K. As discussed earlier, some of the loss in surface area after heating to 1273 K may be due to collapse of the underlying γ-Al_2O_3, since the γ-Al_2O_3 was calcined to only 1173 K prior to ALD. By comparison, the specific surface area of the bulk $Ce_{0.5}Zr_{0.5}O_2$ prepared by a standard precipitation method was 55 m^2/g after calcination to 773 K but decreased to 3 m^2/g at 1173 K and 0.5 m^2/g after 1273 K.

Table 5.2: Temperature with Differential Activity of 10% Conversion as a Function of Calcination Temperature

	Temperature with 10% CO Oxidation Conversion (K)	
Calcination Temp. (K)	**50CZ(ALD)-Al_2O_3**	**$Ce_{0.5}Zr_{0.5}O_2$**
773	353	353
1173	363	423
1273	403	463

In order to determine the catalytic activity of the two CeO_2-ZrO_2 samples after calcination, we impregnated each sample with 1-wt% Pd and performed CO-oxidation light-off measurements in 25 Torr CO and 12.5 Torr O_2. The mixed oxides were calcined prior to addition of Pd in order to separate issues of Pd sintering from thermal degradation of the support. A summary of all the data, in the form of the temperature at which 10% conversion is achieved for catalysts with 1-wt% Pd and a gas hourly space velocity of 72,000 mL g^{-1} hr^{-1} is shown in Table 5.2. Figure 5.5(a) shows a comparison of catalysts with 1-wt% Pd on 50$Ce_{0.5}Zr_{0.5}O_2$-Al_2O_3, bulk $Ce_{0.5}Zr_{0.5}O_2$, and γ-Al_2O_3 after the supports had been calcined to 773 K. (Note: In all cases, the γ-Al_2O_3 had been heated to 1173 K prior to any modification by ALD or catalyst testing.) The light-off temperature is shifted downward by approximately 100 K on the ceria-containing catalysts compared to that observed on Pd/γ-Al_2O_3. The promotional effect of CeO_2 and CeO_2-ZrO_2 on CO oxidation is well documented and is due to oxygen transfer at the Pd-support interface [13,14]. The light-off curves for 1-wt% Pd on 50$Ce_{0.5}Zr_{0.5}O_2$-Al_2O_3 and bulk $Ce_{0.5}Zr_{0.5}O_2$ are

indistinguishable. In both cases, the Pd is in contact with CeO_2-ZrO_2 and the similarity in rates results from a similarity in the Pd-support contact area.

Heating the supports to 1173 K had minimal effect on the $50Ce_{0.5}Zr_{0.5}O_2$-Al_2O_3 support but dramatically increased the light-off temperature observed for bulk $Ce_{0.5}Zr_{0.5}O_2$, as shown in Figure 5.5(b). The loss in activity of the bulk $Ce_{0.5}Zr_{0.5}O_2$ support is explained by the dramatic loss in surface area of this sample. The fact that the ALD-prepared $50Ce_{0.5}Zr_{0.5}O_2$-Al_2O_3 did not lose activity indicates that the CeO_2-ZrO_2 film must remain well dispersed on the support, since lower rates would be observed if Pd were only in contact with the underlying alumina. Finally, after heating to 1273 K, the catalyst prepared from bulk $Ce_{0.5}Zr_{0.5}O_2$ was less active than the initial Pd on γ-Al_2O_3 catalyst, primarily due to lost surface area, while the ALD-prepared sample retained some of its promotional properties. For comparison, the 1-wt% Pd/$50Ce_{0.5}Zr_{0.5}O_2$-Al_2O_3 catalyst showed 10% conversion at 353 K, 90 K lower than that found on the initial Pd/γ-Al_2O_3. The fact that promotional effects are still observed on the 1-wt% Pd/$50Ce_{0.5}Zr_{0.5}O_2$-Al_2O_3 provides additional evidence that the $Ce_{0.5}Zr_{0.5}O_2$ phase must remain reasonably well dispersed on the Al_2O_3 support in order for there to be good contacting with the Pd particles.

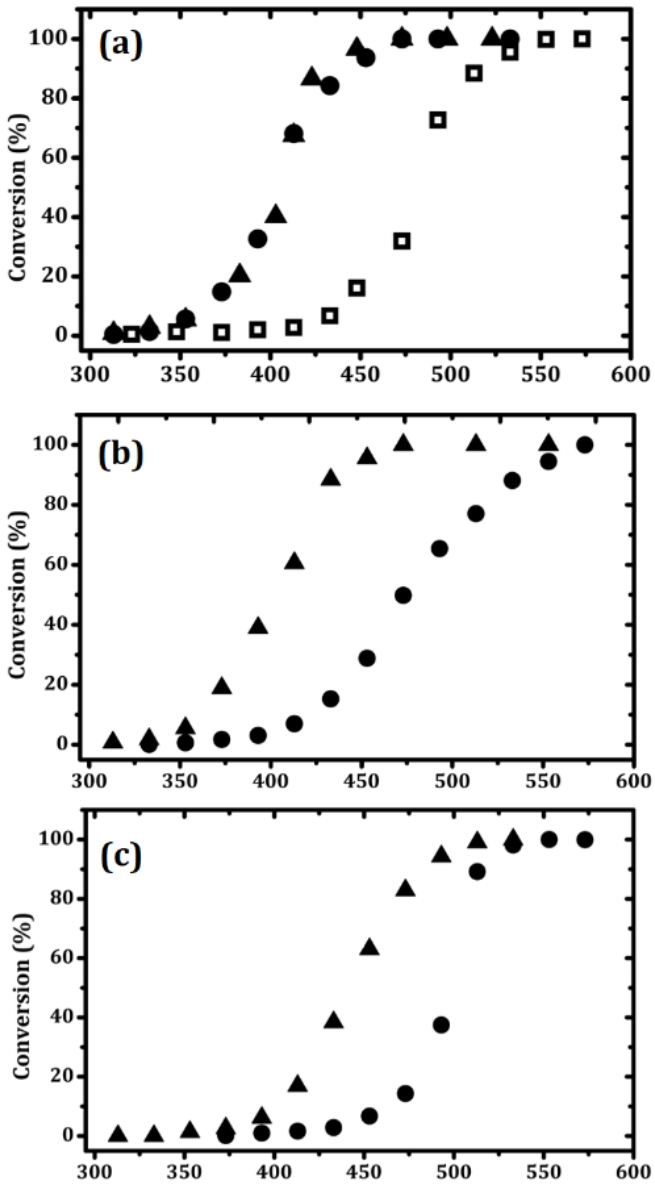

FIG. 5.5. Light-off curves of CO conversion versus temperature for: (▲) – Pd/50$Ce_{0.5}Zr_{0.5}O_2$-Al_2O_3 and (●) – Pd/ $Ce_{0.5}Zr_{0.5}O_2$ (bulk) after the support has been calcined to (a) 773 K, (b) 1173 K, and (c) 1273 K. After the pretreatment, 1 wt.% of Pd was added followed by calcination to 773 K. Rates from (□) – Pd/ Al_2O_3 calcined to 773 K are added for comparison. The CO oxidation reaction was carried out with partial pressures of CO and O_2 at 25 Torr and 12.5 Torr, respectively.

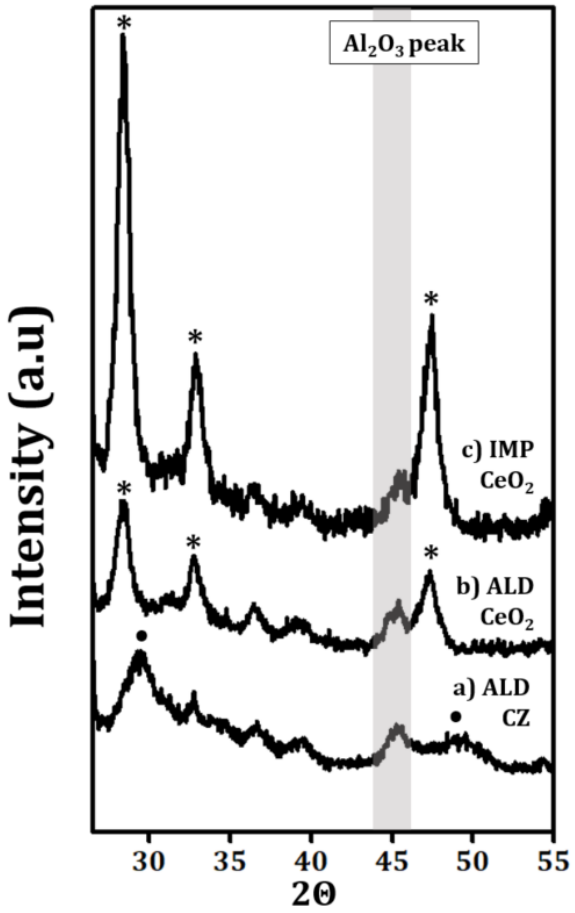

FIG. 5.6. XRD patterns of (a) 20CZ(ALD)-Al_2O_3, (b) 20CeO_2-Al_2O_3, and (c) CeO_2(IMP)/Al_2O_3 after redox cycling conditions. The CeO_2(IMP)/γ-Al_2O_3 sample underwent three cycles of alternating reduction (90% H_2 and 10% H_2O for 30 min) and oxidation (dry air for 30 min) at 1073 K. The ALD-prepared samples, (a) and (b), were exposed to similar oxidation and reduction cycles over a period of several weeks, at temperatures between 873 and 1073 K. Peaks were normalized to a distinct graphite peak around 2Θ = 26.7°. Characteristic peaks for ceria-zirconia solid solution are marked by ●, while peaks for CeO_2 are marked by *.

5.3.3 Thermodynamic Measurements:

Because redox cycling, alternating between reducing and oxidizing environments at high temperatures, has been shown to affect ceria crystallite size much more strongly

than simple, high-temperature calcination [1], we also measured XRD patterns for the $20CeO_2$-Al_2O_3, 20CZ(ALD)-Al_2O_3, and CeO_2(IMP)/Al_2O_3 samples after redox cycling, with results shown in Figure 5.6. The CeO_2(IMP)/Al_2O_3 sample underwent three cycles of alternating reduction (90% H_2 and 10% H_2O for 30 min) and oxidation (dry air for 30 min) at 1073 K. The two ALD-prepared samples were used for the thermodynamic measurements that will be discussed later and were exposed to many oxidation and reduction cycles over a period of several weeks, at temperatures between 873 and 1073 K. Redox cycling significantly narrowed and increased the intensity of the peak at approximately 28 degrees 2θ on the CeO_2(IMP)/Al_2O_3 sample. Using the width at half height of the (220) diffraction peak, the ceria crystallite size on the CeO_2(IMP)/Al_2O_3 sample increased from 7 to 18 nm. Redox aging also caused changes in the XRD pattern for the $20CeO_2$-Al_2O_3 in that the fluorite phase now clearly evident, implying that the film had formed at least some crystallites. However, even after this harsh treatment, the CeO_2 crystallite size on the $20CeO_2$-Al_2O_3 sample was only 5 nm. Furthermore, the intensity of the CeO_2 diffraction peak remained much lower than that of the fresh CeO_2(IMP)/γ-Al_2O_3 sample. The 20CZ(ALD)-Al_2O_3 sample also exhibited a weak peak that can be associated with a $Ce_{0.5}Zr_{0.5}O_2$ phase; but, again, this feature is weak in intensity and very broad.

Thermodynamic measurements were performed on the bulk $Ce_{0.5}Zr_{0.5}O_2$, the $20CeO_2$-Al_2O_3 with 0.24 g CeO_2/g Al_2O_3 and the 20CZ(ALD)-Al_2O_3 with 0.31 g $Ce_{0.5}Zr_{0.5}O_2$/g Al_2O_3 samples after each sample has been calcined to 1073 K for 2 hr. To determine the maximum extents of reduction in the $20CeO_2$-Al_2O_3 and the 20CZ(ALD)-

Al_2O_3 samples, the samples were initially exposed to dry, flowing H_2 at 973 K in the flow-titration system. Assuming that all the oxygen which could be reversibly removed was due to reduction of Ce^{4+} to Ce^{3+}, the calculated O: Ce ratio for both samples was 1.55 after reduction. This value did not change with repeated oxidation-reduction cycles and differs from the value expected for complete reduction by 10%. The probable reason for the discrepancy is the uncertainty in the ceria loading (e.g. Sample weights can be difficult to measure due to water adsorption upon exposure to laboratory air.). The result demonstrates that the ceria in the ALD films is fully reducible.

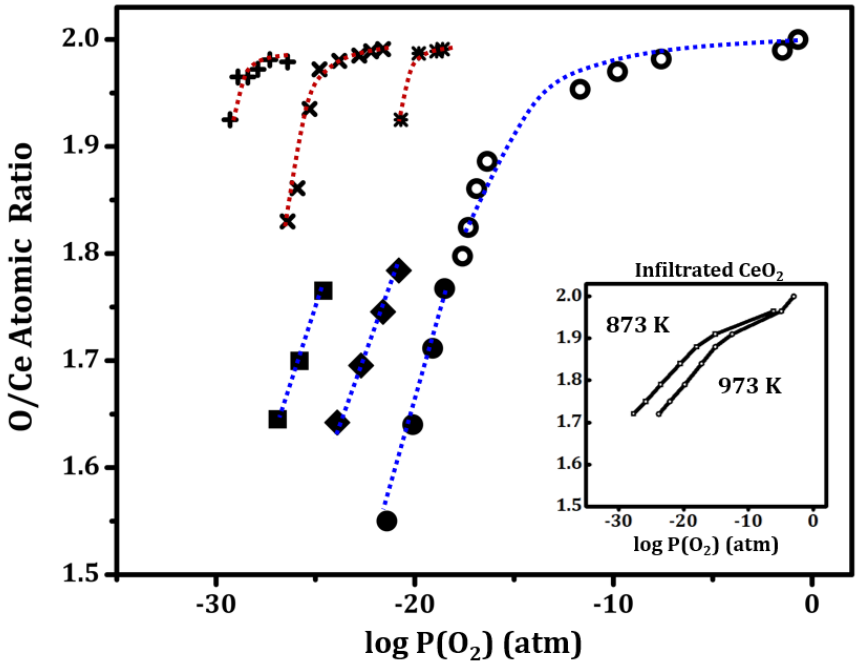

FIG. 5.7. Oxidation isotherms for $20CeO_2$-Al_2O_3 at selected temperatures (873K, 973 K, 1073 K). The results for pure ceria were obtained from a previous publication from our group [1], and were determined by flow titration at (+) – 873 K, (x) – 973 K, and (*) – 1073 K. The (■), (▲), and (●) symbols show the isotherms for $20CeO_2$-Al_2O_3 determined by flow titration at 873K, 973 K and 1073 K respectively. The (○) symbol shows the isotherm for $20CeO_2$-Al_2O_3 determined by coulometric titration at 1073 K. For comparison, previous results for infiltrated ceria on alumina-based support obtained from coulometric titration at 873 K and 973 K are shown [1].

The thermodynamic, redox properties of the $20CeO_2$-Al_2O_3 sample were measured using both flow-titration (the solid data points) and coulometric-titration (the unfilled points) measurements; and a plot of the cerium oxygen stoichiometry as a function of P_{O_2} is shown in Figure 5.7. For comparison purposes, the figure also includes data from earlier work on bulk ceria and from an impregnated, 30-wt% ceria on La-treated Al_2O_3 (shown in the inset) [1]. Flow-titration measurements were performed at 873, 973, and 1073 K but coulometric-titration was performed only at 1073 K on this sample. The data at 1073 K showed that there was good agreement between the two techniques in the P_{O_2} range where the measurements overlapped. The redox thermodynamics for the $20CeO_2$-Al_2O_3 sample differ dramatically from that for bulk ceria. As noted in previous publications, bulk ceria is very difficult to reduce [1]. Of equal interest, the thermodynamic data for the $20CeO_2$-Al_2O_3 sample are remarkably similar to the previously published data for impregnated ceria on La-doped alumina in regions where the P_{O_2}values overlap. For example, at 973 K and a $P_{O_2}$of 10^{-20} atm, the O: Ce ratio was close to 1.75 on both samples. Similarly, at 873 K and a $P_{O_2}$of 10^{-25} atm, the O: Ce ratio was close to 1.78 on both samples. The fact that the thermodynamic data did not change would suggest that equilibrium data is not a strong function of crystallite size, at least over the range of crystallite sizes investigated here.

The oxidation isotherms for bulk $Ce_{0.5}Zr_{0.5}O_2$ and for $20Ce_{0.5}Zr_{0.5}O_2$-Al_2O_3 are shown in Figure 5.8. Results for the bulk $Ce_{0.5}Zr_{0.5}O_2$ were only measured at 1073 K but the data again agree well with previously published data for a sample with this composition in regions where measurements were previously performed [8]. Similar to results for bulk

CeO_2 and $20CeO_2$-Al_2O_3, the equilibrium oxygen stoichiometry in the bulk $Ce_{0.5}Zr_{0.5}O_2$ sample varied gradually with the P_{O_2}. The data for the $20Ce_{0.5}Zr_{0.5}O_2$-Al_2O_3 sample were significantly different. First, flow titration was not useful in measuring the properties for the $20Ce_{0.5}Zr_{0.5}O_2$-Al_2O_3 sample because the sample was completely reduced at all

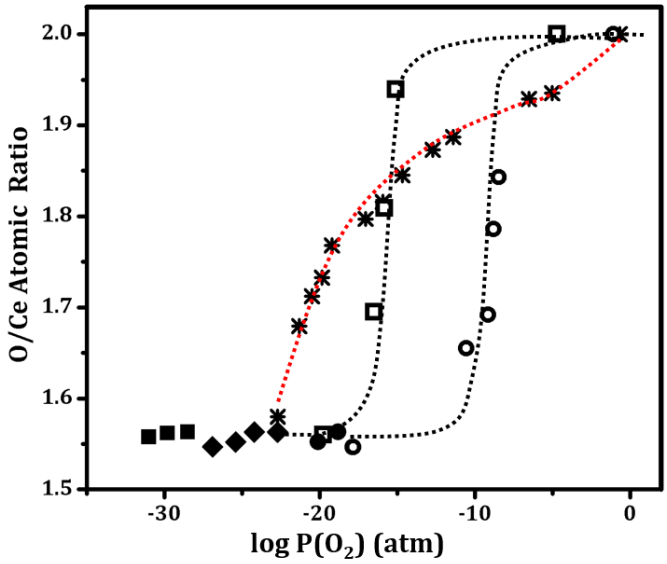

FIG. 5.8. O/Ce ratio as a function of $P(O_2)$ for $20CZ(ALD)$-Al_2O_3, determined by flow titration, at temperatures (♦) – 773K, (■) – 873 K, and (●) – 1073 K. The (○) symbol shows the isotherm for $20CZ(ALD)$-Al_2O_3 determined by coulometric titration at 1073 K. Oxidation isotherm result for pure ceria-zirconia ($Ce_{0.5}Zr_{0.5}O_2$) are obtained by flow titration at (*) – 1073 K, and the result is consistent with previous literature [8].

experimentally accessible H_2O:H_2 ratios between 873 K and 1073 K. It was therefore necessary to measure the equilibrium isotherms at 873 and 1073 K using coulometric titration. Interestingly, the isotherms at both temperatures were nearly vertical lines, which is an indication that there is equilibrium between two well-defined compounds. The transitions for reduction of Ce^{4+} to the Ce^{3+} states occur at P_{O_2} of approximately 10^{-9} atm at

1073 K and 10^{-15} atm at 873 K. These values are much higher than the equilibrium P_{O_2} for the $20CeO_2$-Al_2O_3 sample, showing that the mixed oxide is much easier to reduce.

Heats of oxidation can be calculated from the temperature dependence of the isotherm using Equation 1:

$$-\Delta H = R\frac{\partial \ln P(O_2)}{\partial {}^{1}/_{T}} \quad \textbf{(Equation 5.1)}$$

The heats, $-\Delta H$, calculated from this equation and the data in Figures 5.7 and 5.8 are plotted in Figure 5.9, together with previously reported numbers for CeO_2 supported on La-Al_2O_3 [1] and for bulk $Ce_{0.5}Zr_{0.5}O_2$ [8]. The heats of oxidation for both the $20CeO_2$-Al_2O_3 and 20CZ(ALD)-Al_2O_3 samples were between 550 and 600 kJ/mol O_2, independent of the extent of reduction. This is much lower than the reported heat of oxidation for bulk

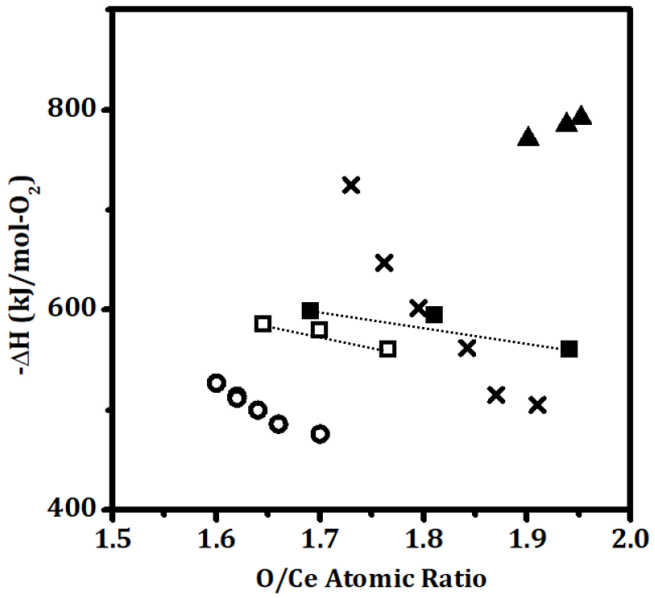

FIG. 5.9. -ΔH of oxidation as a function of O/Ce ratio for (■) – 20CZ(ALD)-Al_2O_3 and (□) – $20CeO_2$-Al_2O_3. Results for (▲) – bulk CeO_2, (○) – bulk $Ce_{0.5}Zr_{0.5}O_2$, and (x) – infiltrated CeO_2 on alumina-based support are obtained from previous work for comparison [1,8].

CeO_2, 760 kJ/mol O_2. In the previous study of impregnated CeO_2 on La-doped Al_2O_3, $-\Delta H$ was reported to vary with stoichiometry, increasing from 500 kJ/mol O_2 at low extents of reduction and to a value close to that of the bulk oxide at high reduction levels. $-\Delta H$ for $Ce_{0.5}Zr_{0.5}O_2$ were reported to be in the range of 500 kJ/mol O_2. The uncertainty in the calculated $-\Delta H$ is relatively high, perhaps ~50 kJ/mol, when the oxide stoichiometry varies with P_{O_2}, as it does for the 20CeO_2-Al_2O_3 sample. However, when the isotherm is a vertical line, as with the 20CZ(ALD)-Al_2O_3 sample, the uncertainty is much less. Therefore, we suggest that the oxidation enthalpies for all of these catalysts may be similar, at least for low extents of reduction.

5.4 Discussion

The results in this paper demonstrate that novel ceria and ceria-zirconia supports can be prepared by ALD onto stable supports. In particular, the thin films grown on γ-Al_2O_3 are shown to be stable to high temperature sintering and relatively immune to redox cycling. The ALD-grown materials are structurally very different from materials having the same compositions but prepared by conventional impregnation. Not only do the ALD films form a more uniform coverage over the γ-Al_2O_3 support but one can more easily form mixed oxides like $Ce_{0.5}Zr_{0.5}O_2$ without the use of chelating agents, like citric acid.

Since there was no loss in reducibility upon redox cycling on any of the samples, $CeAlO_3$ formation does not appear to be a serious issue with these materials. However, there was evidence of CeO_2 crystallite growth on the ALD CeO_2 prepared sample under redox cycling. This may be partly due to differences in the "wetting" properties of CeO_2

and Ce_2O_3 on γ-Al_2O_3 or it may be due to the expansion and contraction that must occur in the film upon oxidation and reduction. If wetting issues dominate, it may be possible to stabilize the CeO_2 films by using something other than γ-Al_2O_3 as the underlying support; if expansion-contraction issue are responsible, the underlying support will probably not matter. It is interesting that the ceria-zirconia film in the ALD prepared sample appears to be more stable but the reasons for this are still uncertain.

The thin $Ce_{0.5}Zr_{0.5}O_2$ film on the 20CZ(ALD)-Al_2O_3 sample appears to exhibit different equilibrium P_{O_2} from that of bulk $Ce_{0.5}Zr_{0.5}O_2$. While this could be due to surface energies, we suggest that it may also due to the confined geometry of the film. In previous work with bulk ceria-zirconia mixed oxides [8], it was argued that the shape of the isotherm results primarily from changes in the entropy of oxidation, rather than changes in the heats of oxidation. This conclusion was based on the fact that $-\Delta H$ was found to be independent of the extent of reduction. To explain how the oxidation entropy would change with the extent of reduction while the enthalpy was constant, it was suggested that each lattice oxygen that is adjacent to a pair of Ce^{4+} ions is energetically equivalent. However, since it should be energetically difficult to remove a lattice oxygen that is next to a vacancy, the number of possible oxygens that can be removed next to each set of adjacent Ce^{4+} ions will decrease as the solid becomes progressively reduced. In a film that is less than one unit cell in thickness, there is no possibility for adjacent vacancies and $-\Delta G$ could be independent of the extent of reduction. According to this hypothesis, the equilibrium properties of ceria-

zirconia films should change with thickness, a possibility that would be interesting to test in future work.

Obviously, there is still much to learn about the properties of thin ceria and ceria-zirconia films prepared by ALD. The materials clearly show interesting properties as catalyst supports. Studying their redox properties may help to elucidate how surfaces and interfaces with other oxides affect thermodynamic equilibria.

5.5 Conclusion

In summary, ALD offers a very promising approach for the preparation of complex oxide supports. By alternating precursors, formation of $Ce_{0.5}Zr_{0.5}O_2$ solid solutions can be achieved at modest temperatures. Unlike supported oxides prepared by infiltration and precipitation methods, which tend to form crystallites on the support, $Ce_{0.5}Zr_{0.5}O_2$ prepared by ALD formed uniform films that completely coat the underlying support. The catalysts prepared by ALD promote CO oxidation on supported Pd similarly to bulk, ceria-zirconia solid solutions and maintain their surface areas and catalytic activity to higher temperatures. The films are also reasonably stable to redox cycling. The thermodynamic, redox properties of the CeO_2 and $Ce_{0.5}Zr_{0.5}O_2$ films were also investigated. Although CeO_2 film prepared by ALD were similar to those of a sample prepared by impregnation, the ALD samples showed better catalytic properties as supports for Pd due to improved contact between the ceria and the Pd. Thermodynamic measurements on the mixed-oxide film indicated that solid solutions were formed and these were much more easily reduced than normal ceria.

5.6 References

1. Zhou G.; Shah P.R.; Montini T.; Fornasiero P.; Gorte R. J.; *Surf. Sci.* **2007**, 601, 2512-2519.

2. He B.J.J; Wang C.X.; Zheng T.T.; Zhao Y.K.; *Johns. Matthey Technol. Rev*, **2016**, 60, 196-203

3. Morikawa A.; Suzuki T.; Kanazawa T.; Kikuta K.; Suda A.; Shinjo H.; *Appl. Catal. B*, **2008**, 78:210-221.

4. Montini T.; Melchionna M.; Monai M.; Fornasiero P.; *Chem. Rev.*, **2016**, 116, 5987-6041.

5. Fornasiero P.; Dimonte R.; Rao G.R.; Kaspar J.; Meriani S.; Trovarelli A.; Graziani M.; *J. Catal.*, **1995**, 151, 168-177.

6. Shah P.R.; Kim T.; Zhou G.; Fornasiero P.; Gorte R.J.; *Chem. Mater.* **2006**, 18, 5363-5369.

7. Kim T.; Vohs J.M.; Gorte R.J.; *Ind. Eng. Chem. Res.* **2006**, 45, 5561-5565.

8. Zhou, G.; Shah, P.R.; Kim, T.; Fornasiero, P.; Gorte, R.J.; *Catal. Today*, **2007**, *123*, 86-93.

9. Putkonen M.; Niinistö L.; *J. Mater. Chem.* **2001**, 11, 3141-3147.

10. Coll M.; Gazquez J.; Palau A.; Varela M.; Obradors X.; Puig T.; *Chem. Mater.* **2012**, 24, 3732-3737.

11. Bozo C.; Gaillard F.; Guilhaume N.; *Appl. Catal. A*, **2001**, 220, 69-77.

12. Kaspar, J.; Fornasiero, P.; Balducci, G.; Di Monte, R.; Hickey, N.; Sergo, V.; *Inorg. Chim. Acta* **2003**, *349*, 217-226.

13. Bunluesin T.; Gorte R. J.; Graham G.W.; *Appl. Catal. B*, **1997**, 14, 105-115

14. Cargnello M.; Doan-Nguyen V.V.; Gordon T.R.; Diaz R.E.; Stach E.A.; Gorte R.J.; Fornasiero P.; Murray C.B.; *Science* **2013**, 341, 771-773.

CHAPTER 6. SMART PALLADIUM CATALYST WITH IMPROVED THERMAL STABILITY SUPPORTED ON HIGH-SURFACE-AREA LANTHANUM FERITE PREPARED BY ALD

Summary:

The concept of self-regenerating or "smart" catalysts, developed to mitigate the problem of supported metal particle coarsening in high-temperature applications, involves redispersing large metal particles by incorporating them into a perovskite-structured support under oxidizing conditions and then exsolving them as small metal particles under reducing conditions. Unfortunately, the redispersion process does not appear to work in practice because the surface areas of the perovskite supports are too low and the diffusion lengths for the metal ions within the bulk perovskite too short. Here, we demonstrate reversible activation upon redox cycling for CH_4 oxidation and CO oxidation on Pd supported on high-surface-area $LaFeO_3$ prepared as a thin conformal coating on a porous $MgAl_2O_4$ support using Atomic Layer Deposition (ALD). The $LaFeO_3$ film, less than 1.5-nm thick, was shown to be initially stable to at least 1173 K. The activated catalysts exhibit stable catalytic performance for methane oxidation after high-temperature treatment.

6.1 Introduction

Most transition-metal catalysts are prepared as small metal particles on high-surface-area oxide supports in order to maximize the metal surface area, where reactions occur, with relatively small amounts of the expensive metal [1-4]. However, in high-temperature applications, such as automotive-emissions control catalysis and catalytic combustion, catalyst deactivation due to lost metal surface area caused by coarsening of the metal particles is a serious problem [5].[10] An exciting development in this regard was the discovery of so-called "smart" catalysts [6],[11] in which coarsened particles of the catalytic metal can be redispersed by reaction with a perovskite-structured support under oxidizing conditions and then exsolution as small metal particles under reducing conditions [6-8].[11-13] Under oxidizing conditions, the metal cations become part of the perovskite lattice. This concept was first demonstrated with Pd on $LaFeO_3$ but has since been shown to be applicable with various transition metals on a number of perovskite oxides [9-11]

Unfortunately, the redispersion process appears to have limited effectiveness in practical applications. Most perovskite-structured oxides have much lower specific surface areas compared to the oxides most commonly used as catalyst supports. The low surface area comes from the fact that the perovskites exist as relatively large crystallites, particularly after exposure to the high temperatures needed to form the perovskite structure or those experienced in use. This has important consequences. First, there is limited area available for the dispersed metal particles at the surface of the perovskite since the surface area of the metal catalyst cannot be higher than the area of the support. Second, the

diffusion of metal cations within the perovskite lattice is slow and the diffusion distance will be much less than the crystallite size. Consequently, the exsolution process for perovskites that have been uniformly doped with metal cations initially occurs within the bulk oxide [12,13], eventually followed by emission of relatively large particles from the oxide in order to minimize the strain energy [14].

One way to increase the perovskite surface area is to deposit it on a more stable support. For example, Tian et al. crystallized $LaFeO_3$ within a mesoporous, silica foam. The resulting material consisted of 10- to 12-nm $LaFeO_3$ crystallites supported on silica [10]. Most of the exposed surface in this 17-wt% $LaFeO_3$ composite was silica, based on the fact that a 10-nm film of $LaFeO_3$ with a density of 6.65 g/cm^3 would cover only 2.6 m^2/g of the 736 m^2/g of the silica surface. For smart-catalyst applications, it is important to ensure high and homogeneous dispersion of the active/protective phase, e.g. the present perovskite phase.

The ideal configuration for this application would have the perovskite phase exist as a conformal film on a stable oxide support [15]. Because a 1-nm film of $LaFeO_3$ on a suitable 100-m^2/g support would be 40-wt% $LaFeO_3$, film dimensions can be very small, even for relatively high perovskite loadings. Recent work has shown that such conformal oxide films can be formed by ALD. In ALD, the solid substrate is first allowed to react with an organometallic precursor. Because the precursor is unreactive with itself, reaction is limited to no more than one monolayer. After removing the excess, the adsorbed surface layer is oxidized and the cycle is repeated. Growth rates depend on various factors,

including ligand size, but are typically 0.01 to 0.04 nm per cycle for all but the smallest precursor molecules [16]. Mixed oxides, including perovskites, can be grown by alternating the specific organometallic precursors [17,18]. In this paper, we demonstrate the deposition of uniform thin films of $LaFeO_3$ on a high-surface area support by ALD. The materials after the addition of palladium have interesting catalytic and regenerative properties, and remarkably they maintain their high surface areas up to very high temperatures.

6.2 Experimental Methods

The substrate used in the present study was the high-surface area $MgAl_2O_4$ spinel prepared by the synthesis procedure described in Chapter 2. The BET surface area of the support was around 100 m^2/g, and XRD confirmed the structure of the material. High-surface-area, thin-film of lanthanum ferrite ($LaFeO_3$) was deposited on the spinel support by Atomic Layer Deposition (ALD). The conditions used for depositing the precursors, $La(TMHD)_3$ (Strem Chemicals, Inc.) and ferrocene ($Fe(Cp)_2$, Sigma Aldrich), were adopted, with slight modification, from previous publications [19-21]. The $La(TMHD)_3$ precursor was heated to 483 K, while the $Fe(Cp)_2$ precursor was heated to 433 K. During the deposition cycle, the $La(TMHD)_3$ or $Fe(Cp)_2$ vapor was introduced to the evacuated substrate chamber, which contained approximately 0.5 g of substrate. In a typical experiment, the substrate was exposed to the vapor of one of the precursors multiple times at 523 K for 300 s to ensure that reaction with the surface was complete, then the substrate was evacuated to remove excess precursor.

The $Fe(Cp)_2$ was oxidized by oxygen, while $La(TMHD)_3$ precursor was oxidized using NO_2, since the TMHD ligands cannot be completely oxidized by O_2 at 523 K and our system did not allow heating the substrate to higher temperatures. In dedicated experiments, the oxidation part of the ALD cycle was carried out by placing the samples in a muffle furnace at 873 K for 60 s, obtaining equivalent results. The TMHD lanthanum precursor was chosen in this study because the precursor molecules were less likely to thermally decompose to give CVD-like characteristics. 1-wt.% $Pd/MgAl_2O_4$ support was synthesized by incipient wetness using aqueous solutions of tetraaminepalladium(II) nitrate (Sigma Aldrich). $LaFeO_3$ ALD-modified samples containing Pd were prepared using 1-wt.% $Pd/MgAl_2O_4$ as substrate. 1-wt.% Pd on bulk $LaFeO_3$ support was prepared by the citrate sol-gel method or the Pechini method.

The ALD growth rates of La_2O_3, Fe_2O_3, and $LaFeO_3$ were determined gravimetrically as a function of the number of ALD cycles. Elemental analysis of the solid samples for individual elements were confirmed by Inductively Coupled Plasma-Optical Emission spectrometry (ICP-OES) (See Chapter 2 for full procedure). BET surface-area measurements, CO chemisorption, STEM and EDS, EXAFS, and XANES were used to characterize the samples.

Steady-state, methane-oxidation rates were determined in the same flow reactor equipped with GC described in Chapter 2 using 100 mg of catalyst. Helium was used as a carrier gas with the partial pressures of CH_4 and O_2 fixed at 3.8 Torr (0.5%) and 38 Torr (5%) respectively. The total flow rate was kept at 120 mL/min. All rates in this study were normalized to the mass of Pd of each sample, and differential conversions were maintained

in all cases. CO oxidation rates were measured in the same setup with He as the carrier gas and partial pressures of CO and O_2 being 25 and 12.5 Torr respectively. The total flow rate was maintained at 120 mL/min. In order to investigate the effects of the support, the Pd catalysts were either oxidized at 1073 K for 1 hour or reduced at 1073 K for 1 hour prior to any catalytic testing. For the oxidation pretreatment, He was used as the carrier gas, and the total flow rate was kept at 160 mL/min with 20% of O_2. Conditions for the reduction pretreatment were similar with the total flow rate kept at 160 mL/min with 20% of H_2.

6.3 Results

In the present work, we deposited $LaFeO_3$ on a porous $MgAl_2O_4$ support that had been stabilized by calcination at 1173 K to have a surface area of 100 m^2/g. The ALD precursors used were $La(TMHD)_3$ (Tris(2,2,6,6-tetramethyl-3,5-heptanedionato) lanthanum, Strem Chemicals.) and ferrocene ($Fe(Cp)_2$, Sigma Aldrich) and the samples were exposed to the precursor vapors for 300 s. Excess precursor was removed by evacuation. The oxidation cycle used oxygen to oxidize adsorbed $Fe(Cp)_2$. Because TMHD ligands cannot be oxidized by O_2 at the deposition temperature, adsorbed $La(TMHD)_3$ was oxidized by exposure to NO_2. For some samples, adsorbed $La(TMHD)_3$ was oxidized by placing the samples in a muffle furnace at 873 K for 60 s but the materials produced were indistinguishable from those oxidized by NO_2 at the deposition temperature [22].

The growth rates of the individual and the mixed-oxide films were measured by weighing the samples after every five ALD cycles. As shown in Figure 6.1(a) and 6.1(b), the sample mass increased linearly with the number cycles for both precursors, with growth

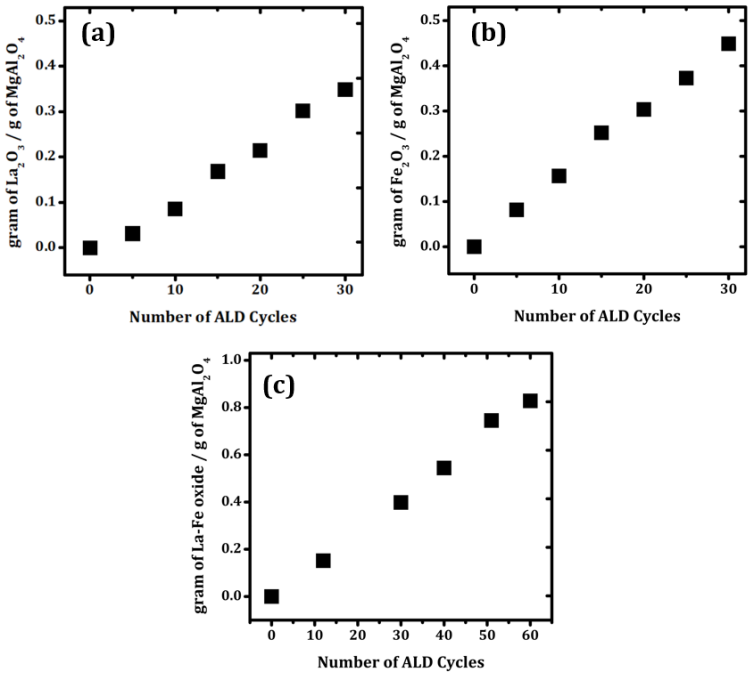

FIG. 6.1. The mass gain of (a) La_2O_3, (b) Fe_2O_3, and (c) $LaFeO_3$ per gram of $MgAl_2O_4$ support as a function of the number of ALD cycles. The mole ratio for the individual growth of La to Fe was approximately 1: 3. $LaFeO_3$ ALD was carried out by alternating 3 La_2O_3 ALD cycles to 1 Fe_2O_3 ALD cycle up to a grand total of 60 cycles.

rates of 11.2 mg La_2O_3/g $MgAl_2O_4$ per cycle (6.9 x 10^{-5} mole La/ g $MgAl_2O_4$ per cycle) and 16.2 mg Fe_2O_3/ g $MgAl_2O_4$ per cycle (2.0 x 10^{-4} mole Fe/ g $MgAl_2O_4$ per cycle). Assuming that both oxides formed uniform dense films on the 100-m^2/g, $MgAl_2O_4$ support, the growth rates for the individual oxides are 0.017 nm/cycle for La_2O_3 and 0.030 nm/cycle for Fe_2O_3. Although growth rates depend on substrate and growth conditions, these values are similar to growth rates reported in the literature for these precursors on flat samples and are reasonable considering the size of the precursor molecules [19-21].

Because the molar growth rate for Fe_2O_3 is approximately three times that for La_2O_3, the stoichiometric $LaFeO_3$ was grown using an alternating sequence of three La_2O_3

ALD cycles followed by one Fe_2O_3 ALD cycle to ensure proper mixing between the metal oxides. Figure 6.1(c) shows that the growth rate using this sequence was again linear with the number of cycles and the final mass after a total of 60 ALD cycles (45 cycles of La_2O_3 and 15 cycles of Fe_2O_3) was 0.79 g La_2O_3-Fe_2O_3/g $MgAl_2O_4$, close to what would be expected based on the linear addition of the individual oxides (0.756 g La_2O_3-Fe_2O_3/g $MgAl_2O_4$). The small difference between the actual mass gained and the calculated mass gained may be due to the different interaction of the La_2O_3 on the Fe_2O_3 or vice versa. Assuming the mixed oxide has the density of $LaFeO_3$, 6.65 g/cm^3, the film thickness after 60 cycles is calculated to be 1.2 nm. The BET surface area of this coated sample was determined by N_2 adsorption to be 49 m^2/g. This decrease in surface area per mass from that of the starting $MgAl_2O_4$ is primarily due to the added mass of the $LaFeO_3$, with a small additional change associate with a decrease in average pore size.

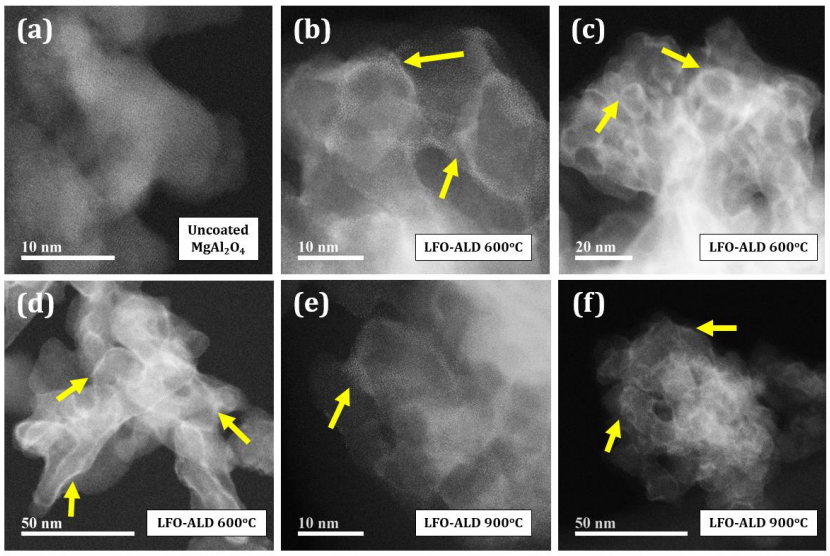

FIG. 6.2. STEM images for (a) unmodified $MgAl_2O_4$ and ALD $LaFeO_3$ modified $MgAl_2O_4$ after calcination to (b)-(d) 873 K and (e)-(f) 1173 K. Arrows indicate regions of high contrast due to the $LaFeO_3$ layer.

High Angle Annular Dark Field (HAADF), Scanning Transmission Electron Microscopy (STEM) imaging demonstrated that the La and Fe oxides were uniformly deposited on the sample with 0.79 g $LaFeO_3$/g $MgAl_2O_4$, as shown in Figures 6.2(a) through 6.2(d). An image of the unmodified $MgAl_2O_4$, shown in Figure 6.2(a), indicates that the support has features that are about 10 nm in size. The images in Figure 6.2(b) and 6.2(c) were obtained on the same batch of $MgAl_2O_4$ after depositing the $LaFeO_3$, followed by calcination at 873 K for 2 h. The images, which show the same sample at two magnifications, now indicate higher contrast at the particle edges, consistent with an oxide film, similar in thickness to 1.2 nm, composed of high-atomic-number atoms. A high magnification image of the sample after calcination at 1173 K for 2 h, Figure 6.2(d), demonstrates that there were minimal changes in the sample appearance following this treatment. The EDS elemental maps for Mg, Al, Fe and La in Figure 6.3 confirm that the bright features found along the edges of the $MgAl_2O_4$ support in the sample calcined to 873 K are due to La and Fe. The La and Fe elemental maps overlap with one another.

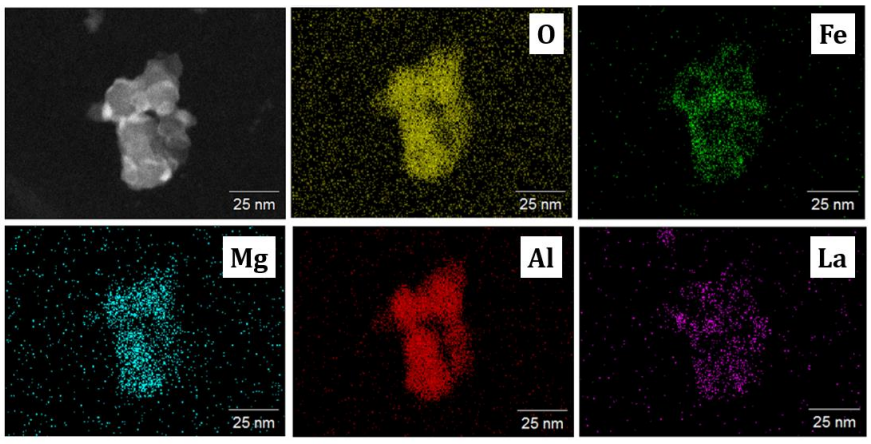

FIG. 6.3. STEM results for ALD $LaFeO_3$ modified $MgAl_2O_4$ with EDS mapping of Mg, Al, O, La, and Fe.

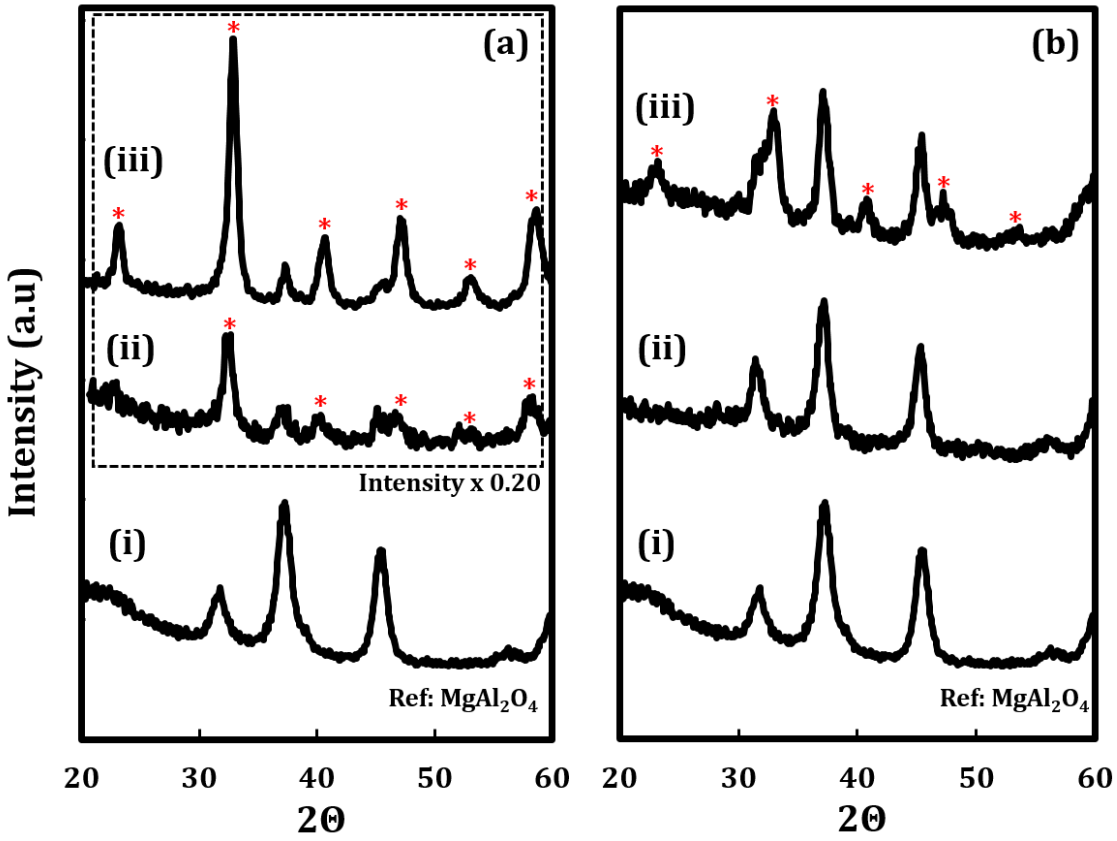

FIG. 6.4. XRD patterns of $MgAl_2O_4$ after ALD of $LaFeO_3$ with (a) higher coverage (0.79 g $LaFeO_3$/g $MgAl_2O_4$) and (b) lower coverage (0.25 g $LaFeO_3$/g $MgAl_2O_4$). For the ALD-modified support with higher coverage (a), the pattern for (i) unmodified $MgAl_2O_4$ was compared against the ALD-modified $MgAl_2O_4$ after calcination to (ii) 873 K and (iii) 1073 K in air. The intensities for (ii) and (iii) were reduced by 0.20. For (b), the XRD pattern for (i) unmodified $MgAl_2O_4$ was compared against the ALD-modified $MgAl_2O_4$ with lower coverages after heated to (ii) 1073 K and (iii) 1173 K in air. Characteristic peaks for $LaFeO_3$ are marked by *.

Formation of the perovskite structure was demonstrated using X-Ray Diffraction (XRD), as shown in Figure 6.4. Results here are reported for two different $LaFeO_3$ coverages, 0.79 g $LaFeO_3$/g $MgAl_2O_4$ in Figure 6.4(a) and 0.25 g $LaFeO_3$/g $MgAl_2O_4$ (15 ALD cycles of La_2O_3 and 5 of Fe_2O_3, average thickness of 0.37 nm) in Figure 6.4(b). The pattern in Figure 6.4(a, i) is that of the unmodified $MgAl_2O_4$, with peaks at approximately

31.7, 37.2, and 45.2 degrees 2θ consistent with cubic spinel-structured $MgAl_2O_4$ (JCPDS: 75-1796). Following deposition of 0.79 g $LaFeO_3$/g $MgAl_2O_4$ and calcination to 873 K for 2 h, the pattern in Figure 6.4(a, ii) indicates that peaks associated with $MgAl_2O_4$ remain but new peaks at 22, 32, 40, 46, 52 and 58 degrees 2θ, associated with a perovskite phase, are clearly visible (JCPDS: 74-2203). The fact that a perovskite phase can be formed at this low temperature implies that there must be good mixing of the La and Fe cations during deposition. Figure 6.4(a, iii) is the diffraction pattern of the same sample after heating in air to 1073 K for 2 h. Peaks due to $MgAl_2O_4$ remain but diffraction at 23.1, 32.8, 40.6, 47.0, 53.0, 58.5 degrees 2θ from the perovskite lattice clearly dominate. Reflections related to any possible solid state reaction products between $MgAl_2O_4$ and $LaFeO_3$ are not observed. Rietveld fitting indicates partial contraction of the cell parameter along the *c* axis suggesting the formation of a distorted structure (Table 6.1). It is interesting to note that an estimate of the crystallite size using the Scherrer Equation and the peak width at half height for the diffraction peak at 40.5 degrees 2θ indicates that the characteristic crystallite size was 4.7 nm at 873 K and 7.8 nm after heating to 1073 K. These values might be viewed in terms of the two-dimensional nature of the films, but they more likely reflect some fraction of the film that has become three-dimensional via coalescence.

To determine the effect of $LaFeO_3$ loading, XRD patterns were measured on the sample with 0.25 g $LaFeO_3$/g $MgAl_2O_4$ and are shown in Figure 6.4(b). Figure 6.4(b, i) is again that of the unmodified $MgAl_2O_4$; but the addition of 0.25 g $LaFeO_3$ to $MgAl_2O_4$, followed by calcination at 1073 K for 2 h, had no effect on the diffraction pattern, Figure

6.4(b, ii). After calcination at 1173 K for 2 h, Figure 6.4(b, iii), small features associated with a perovskite phase begin to appear; but the diffraction features are very weak compared to the intensities in Figure 6.4(a, iii). The highly non-linear dependence between XRD peak intensities and $LaFeO_3$ loading is again consistent with uniform deposition of the film. The failure to observe perovskite diffraction features at this lower coverage, except at the highest temperature, probably reflects the longer length scale required for partial film coalescence into a three-dimensional form.

Table 6.1: Results from Rietveld refinement of 0.79 $LaFeO_3$/g $MgAl_2O_4$ samples ($LaFeO_3$ deposited on 1-wt% Pd/$MgAl_2O_4$) calcined at 1073 K and variation with respect to theoretical cell parameters.

Cell parameter	Theoretical	Experimental	Variation
A (nm)	0.5565	0.5539	- 0.46%
B (nm)	0.7855	0.7809	- 0.59%
C (nm)	0.5556	0.5451	- 1.89%

To compare the catalytic performance of the ALD-modified support and bulk $LaFeO_3$, we introduced Pd into both samples. For the bulk $LaFeO_3$ support, 1-wt% of Pd was added during perovskite synthesis using the Pechini method where the salt solutions of Pd, La and Fe were initially mixed prior to heating in air. This method is known to incorporate Pd into the perovskite lattice [23]. Because it was necessary to calcine this sample at 1173 K to form the perovskite structure, its BET surface area was only 5 m^2/g. For the thin-film sample, 60 ALD cycles (0.79 g $LaFeO_3$/g $MgAl_2O_4$) were deposited onto

a $MgAl_2O_4$ that had 1-wt% Pd added by infiltration, prior to ALD, to a final loading of 0.53-wt% Pd. This sample was then calcined at 1073 K. Both samples were reduced in dry H_2 for 1 h at different temperatures and the presence of surface Pd was probed in methane oxidation experiments carried out under differential conditions in 0.5% CH_4 and 5.0% O_2, with helium as the carrier gas.

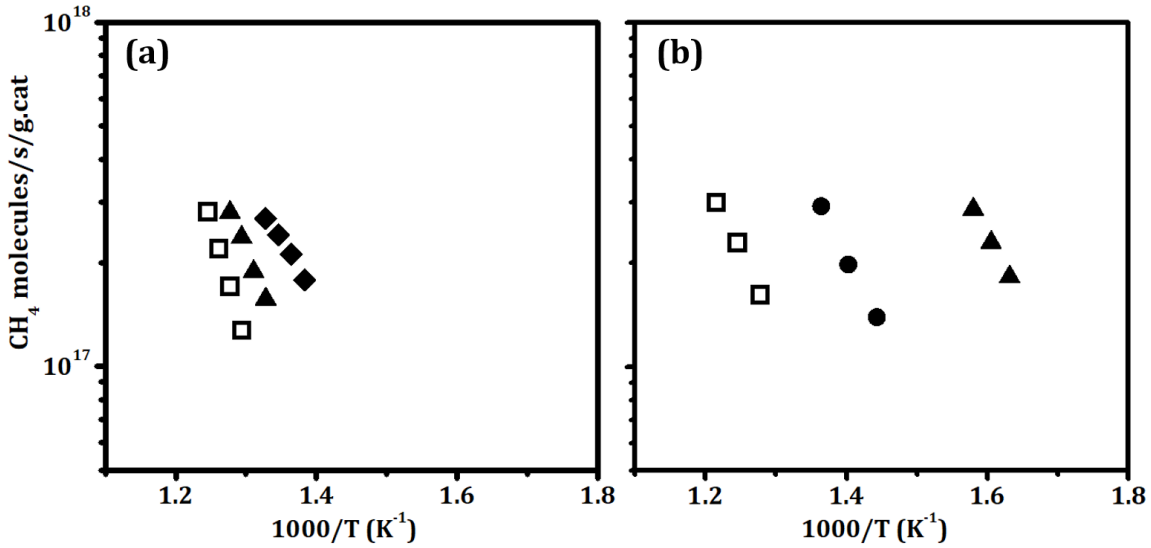

FIG. 6.5. Steady-state, differential reaction rates for methane oxidation in 0.5% CH_4 and 5% O_2. (a) Rates on bulk $LaFe_{0.97}Pd_{0.03}O_3$ (1-wt% Pd) (□) – as prepared and after reduction in 20% H_2 under flowing He at (▲) – 1073 K and (■) – 1173 K. The rates were compared against (b) ALD-modified catalyst (0.79 g $LaFeO_3$ on 1-wt% Pd/$MgAl_2O_4$) (□) – as prepared and after reduction at (●) – 773 K and (▲) – 1073 K.

Arrhenius plots of the rates over the bulk $LaFeO_3$ sample with the Pd incorporated into the lattice structure (designated here in a molar basis as $LaFe_{0.97}Pd_{0.03}O_3$) are shown in Figure 6.5(a). Significant increases in the rates were only observed after reduction at 1173 K. Interestingly, the activation energies for the reaction, determined from the slopes of the lines in the figure, decreased from 110 kJ/mol to 65 kJ/mol following this reduction

treatment, a result that is likely due to a change in going from a $LaFeO_3$-catalyzed reaction to a Pd-catalyzed reaction. This was confirmed by the fact that reaction rates on a $LaFeO_3$ which had no Pd were the same as those on the unreduced $LaFe_{0.97}Pd_{0.03}O_3$. The analogous results for the ALD-prepared samples are shown in Figure 6.5(b). There was already some increase in the rates after reduction at 773 K, but reduction at 1073 K had a very dramatic effect. Since the activation energies determined from the slopes of the lines in Figure 6.5(a) were similar at 75 kJ/mol, the rates in each case are likely due to exposed Pd metal. Assuming that rates are proportional to the exposed Pd metal surface area, extrapolation of the rates to the same temperatures would suggest the sample reduced at 1073 K had approximately 10 times as much Pd on the surface as the sample reduced at 773 K.

In order to demonstrate that the effects of oxidation and reduction were reversible, methane oxidation rates were measured on the sample in which 0.79 g $LaFeO_3$ was deposited on 1-wt% $Pd/MgAl_2O_4$ after reduction at 1073 K for 1 h and after oxidation at 1073 K for 1 h. The differential reaction rates are presented in an Arrhenius plot in Figure 6.6. The rates were very low following high-temperature oxidation, suggesting that the Pd metal is inaccessible following this catalyst pretreatment. Reduction at 1073 K increased the rates to the level observed earlier in Figure 6.5(b). The sample could be repeatedly placed in the inactive or active form by oxidation or reduction at 1073 K.

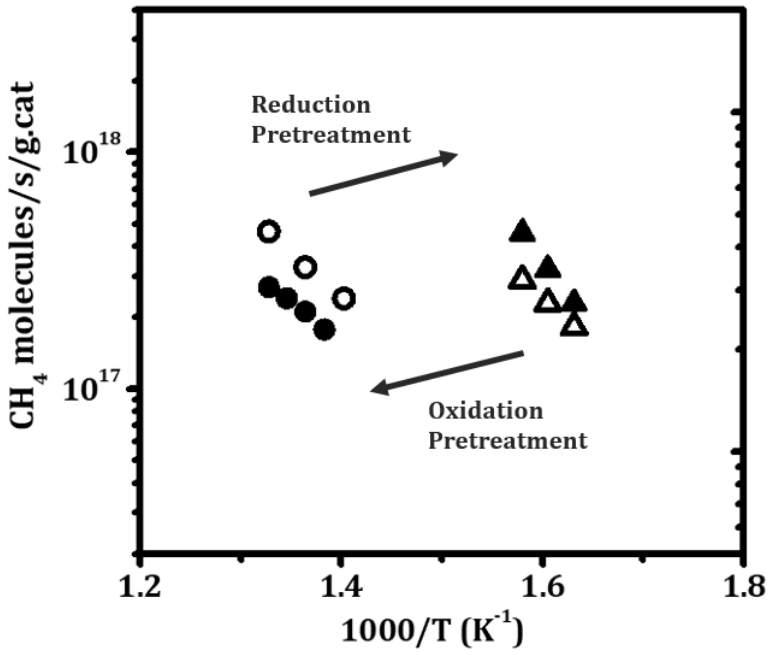

FIG. 6.6. Steady-state methane oxidation rates in 0.5% CH_4 and 5% O_2. The rates of ALD-modified catalyst (0.79 g $LaFeO_3$ on 1-wt% $Pd/MgAl_2O_4$) were compared after the following conditions: (▲) – reduction in 20% H_2 under flowing He at 1073 K, and (■) –oxidation in 20% O_2 under flowing He at 1073 K. Closed symbols denote the first oxidation-reduction cycle, while open symbols represent the second cycle.

CO oxidation rates were also measured on the 0.53-wt% Pd on 0.79 g $LaFeO_3$/g $MgAl_2O_4$ samples ($LaFeO_3$ deposited on 1-wt% $Pd/MgAl_2O_4$) catalyst and a 1-wt% $Pd/MgAl_2O_4$ sample following cyclic oxidation and reduction at 1073 K, with results shown in Figure 6.7. Figure 6.7(a) demonstrates that the ALD-modified catalyst could again be cycled between the active and inactive states by oxidation at 1073 K for 1 h or reduction at 1073 K for 1 h. The changes in the rates are consistent with changes in the Pd dispersion measured by CO chemisorption, reported in Table 6.2. After oxidation at 1073

K, adsorption was negligible; following reduction, the Pd dispersion was ~7%. Rates on the 1-wt% Pd/$MgAl_2O_4$ sample, reported in Figure 6.7(b), were initially high and similar to that on the reduced $LaFeO_3$ deposited on 1-wt% Pd/$MgAl_2O_4$ on a rate per Pd basis. The rates on Pd/$MgAl_2O_4$ sample decreased significantly following calcination at 1073 K probably due to sintering of the Pd particles; however, unlike the case for the perovskite-containing catalyst, activity was not restored by high-temperature reduction.

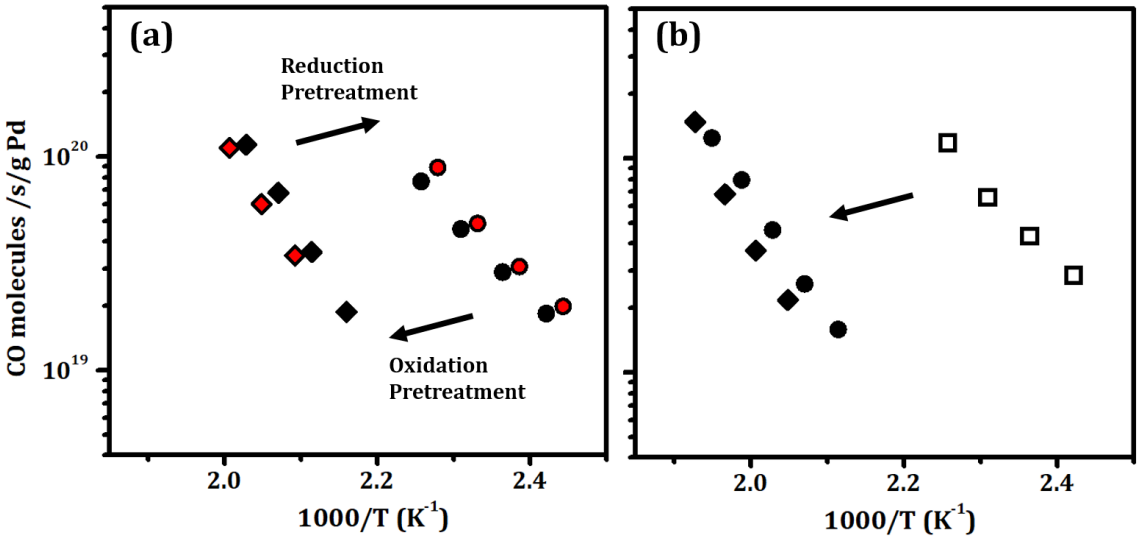

FIG. 6.7. Steady-state, differential reaction rates for CO oxidation reaction with partial pressure of CO and O_2 at 25 Torr and 12.5 Torr, respectively. The rates of (a) ALD-modified catalyst (0.79 g $LaFeO_3$ on 1-wt% Pd/$MgAl_2O_4$) were compared after the following conditions: (●) – reduction in 20% H_2 under flowing He at 1073 K, and (♦) – oxidation in 20% O_2 under flowing He at 1073 K. Black symbols denote the first oxidation-reduction cycle, while red symbols represent the second cycle. The rates of (b) Pd/$MgAl_2O_4$ were compared after the following conditions: (□) – freshly prepared, (●) – reduction in 20% H_2 under flowing He at 1073 K, and (♦) – oxidation in 20% O_2 under flowing He at 1073 K.

Table 6.2: Summary of Pd dispersion (%) based on CO chemisorption results for catalysts after reduction and oxidation pretreatments at 1073 K**.**

	Pd Dispersion (%)				
	Freshly Prepared	**(1) 1073 K Oxidation**	**(1) 1073 K Reduction**	**(2) 1073 K Oxidation**	**(2) 1073 K Reduction**
$Pd/MgAl_2O_4$	12	6	3	1	1
0.79 g $LaFeO_3$-$Pd/MgAl_2O_4$	3	0	7	0	6
$Pd/LaFeO_3$	0.2	0.5	0.4	0.3	0.5

Figure 6.8 displays STEM and EDS results for the $Pd/MgAl_2O_4$ catalyst reduced at 1073 K for 1 h and for the freshly-prepared 0.53-wt% Pd in 0.79 g $LaFeO_3$/g $MgAl_2O_4$ ($LaFeO_3$ deposited on 1-wt% $Pd/MgAl_2O_4$). On the $Pd/MgAl_2O_4$ sample, very large Pd particles, ~10 nm, are clearly visible in Figure 6.8(a). The Pd particles are large because of the high reduction temperature, though only slightly smaller Pd particles were observed in the freshly-prepared $Pd/MgAl_2O_4$ sample. The distribution of Pd in the ALD-modified samples is difficult to characterize by Z-contrast imaging alone since it is effectively masked by the presence of La, as shown in Figure 6.8(b). Never-the-less, EDS provides evidence for large (5-10 nm) Pd particles in its freshly-prepared state, the reduced state, and the reoxidized state. Interestingly, there was some correlation observed between the EDS signals from these Pd particles and Fe in the reduced sample. It is also worth noting that the $LaFeO_3$ film appears to have lost some of its integrity in the Pd-containing samples, *i.e.*, compared with the samples shown in Figures 6.2 and 6.3. The reason for this is still

under investigation though XRD measurements after reduction at 1073 K indicate that the $LaFeO_3$ phase remains unchanged.

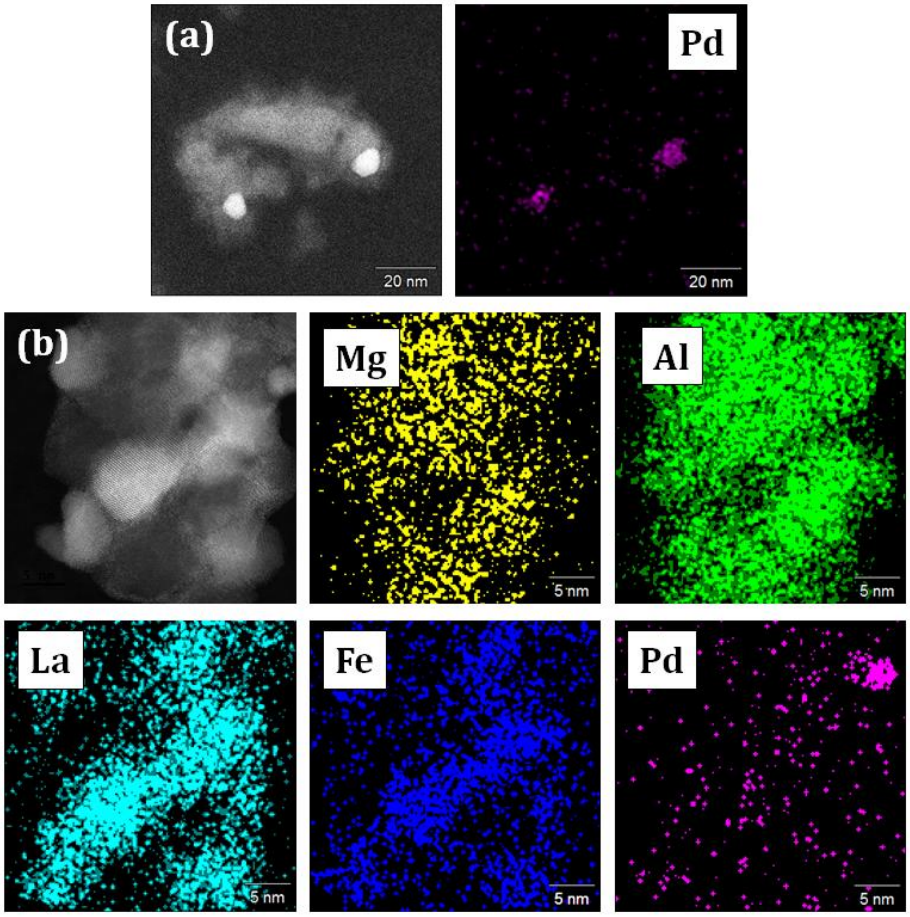

FIG. 6.8. Representative HAADF-STEM images with EDS mapping for (a) $Pd/MgAl_2O_4$ and for (b) ALD-modified catalyst (0.79 g $LaFeO_3$ on 1-wt% $Pd/MgAl_2O_4$)

The nature of the Pd in these samples was also investigated using *ex-situ* Extended X-Ray Absorption Fine Structure (EXAFS) and X-ray Absorption Near Edge Structure (XANES) measurements. These were performed at the Pd K edge on the $Pd/MgAl_2O_4$ and on the 0.53-wt% Pd in 0.79 $LaFeO_3$/g $MgAl_2O_4$ samples ($LaFeO_3$ deposited on 1-wt%

Pd/$MgAl_2O_4$), with the results summarized in Table 6.3. Each of the samples was initially reduced at 1073 K for 1 h. The reduced Pd/$MgAl_2O_4$ sample showed a nearly bulk Pd-Pd bond distance (0.2736 nm). The coordination number (8.7) was significantly smaller, typical of nano-particles of diameters comprised between 1 and 2 nm; but, since this value depends on size distribution and shape, it cannot be used here to precisely determine the particle size. The total coordination number on the ALD-prepared sample is lower and consistent with particles close to 1 nm [24,25]. EXAFS analysis suggests that the reduced ALD-prepared sample contains metallic nanoparticles that may also contain Fe, with Pd-Pd and Fe-Pd distances, as shown in Figure 6.9, close to those reported by Kuroda et al. for Pd-Fe catalysts on SiO_2 [26].

Table 6.3: Pd K edge *ex-situ* EXAFS fitting results for 1073 K pre-reduced samples.

	Pd-Pd CN[a]	**Pd-Pd distance (Å)**	**Pd-Fe CN[a]**	**Pd-Fe distance (Å)**	**σ^{2} [b]**	**E_0**	**S_0^{2} [c]**
Pd (Reference)	12	2.743(8)	-	-	0.0059(2)	2.2(4)	0.86
Pd/$MgAl_2O_4$	8.7(6)	2.736(2)	-	-	0.0063(3)	0.6(7)	0.86
0.79 g $LaFeO_3$-Pd/$MgAl_2O_4$	5.6(7)	2.714(5)	2.0(4)	2.63(1)	0.0077(5)	-1(1)	0.86

[a] Coordination Number; [b] σ^2 term accounts for the mean square variation in path length due to thermal or structural disorder; [c] passive electron reduction factor

To better understand the interaction of Pd with the $LaFeO_3$, we also measured the Fe K edge XANES as shown in Figure 6.10 and 6.11. Consistent with the structural distortion observed by XRD, the ALD-modified sample, prior to reduction, had a different

structure from bulk $LaFeO_3$; however, the shape of XANES of the ALD-prepared sample approaches that of $LaFeO_3$ after reduction, as shown in Figure 6.10. There may also be some metallic iron formed (indicated by an arrow at 7121eV in Figure 6.10) as previously observed *Nishihata et al* [27].

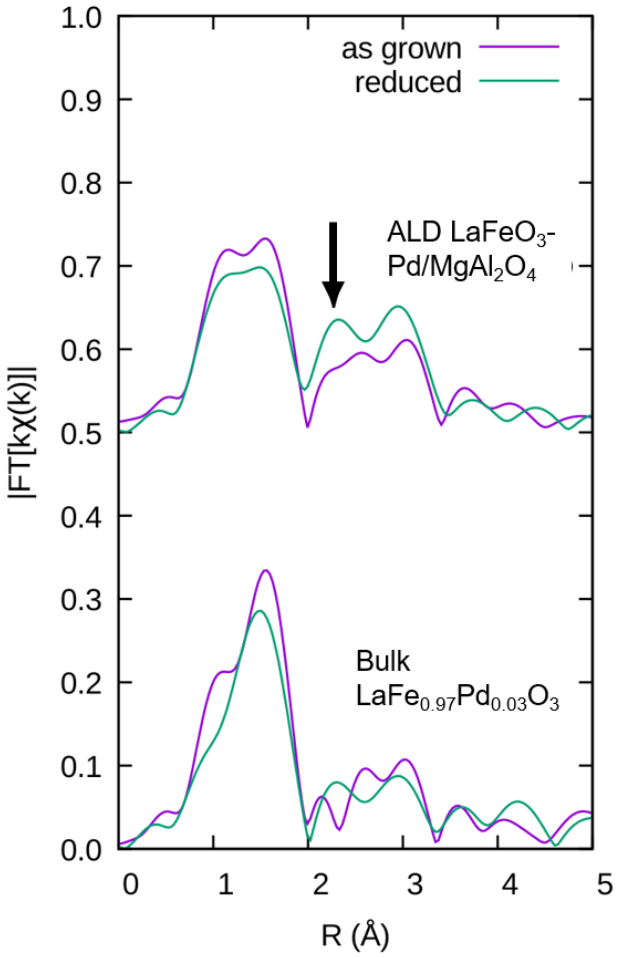

FIG. 6.9. Fourier transforms (moduli) of EXAFS signals at the K edge of Fe of samples, 0.53-wt% Pd on 0.79 $LaFeO_3$/g $MgAl_2O_4$ samples ($LaFeO_3$ deposited on 1-wt% $Pd/MgAl_2O_4$), and bulk $LaFe_{0.97}Pd_{0.03}O_3$ (1-wt% Pd). The black arrow indicates the apparent distance where we expect a metallic Fe-Fe or Fe-Pd bond to appear. The signals are not phase corrected, and it is important to note that the R value is not an actual distance value.

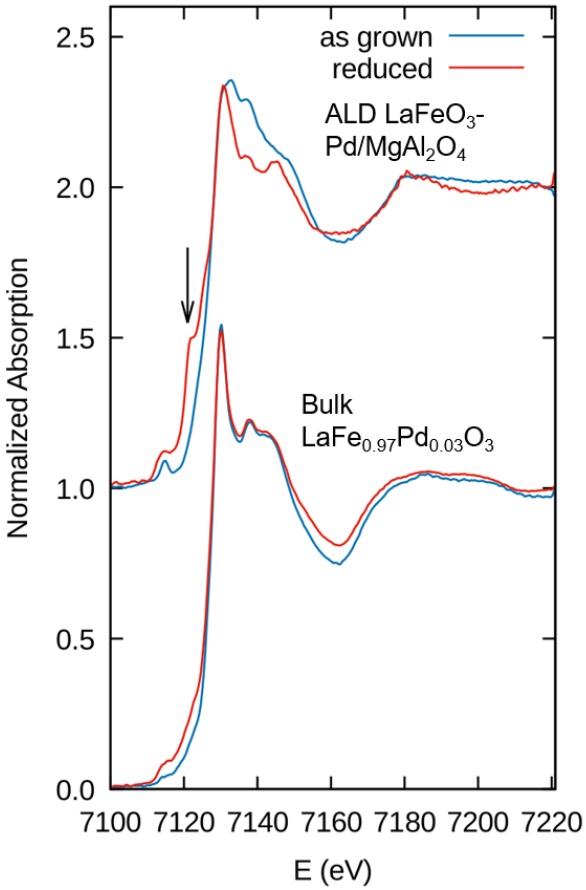

FIG. 6.10. XANES spectra at the Fe K edge of samples, 0.53-wt% Pd on 0.79 $LaFeO_3$/g $MgAl_2O_4$ samples ($LaFeO_3$ deposited on 1-wt% Pd/$MgAl_2O_4$) and bulk $LaFe_{0.97}Pd_{0.03}O_3$ (1-wt% Pd), for freshly prepared samples and reduction at 1073 K.

6.4 Discussion

While stability of the perovskite film remains an issue, the present results demonstrate that perovskite films can be deposited onto high-surface-area supports by ALD. Furthermore, when used as a support for Pd, these materials show evidence for reversible exsolution of the Pd following redox cycling. Following high-temperature

oxidation and reduction, the catalysts modified by ALD also showed superior catalytic activity compared to the unmodified $Pd/MgAl_2O_4$ catalyst.

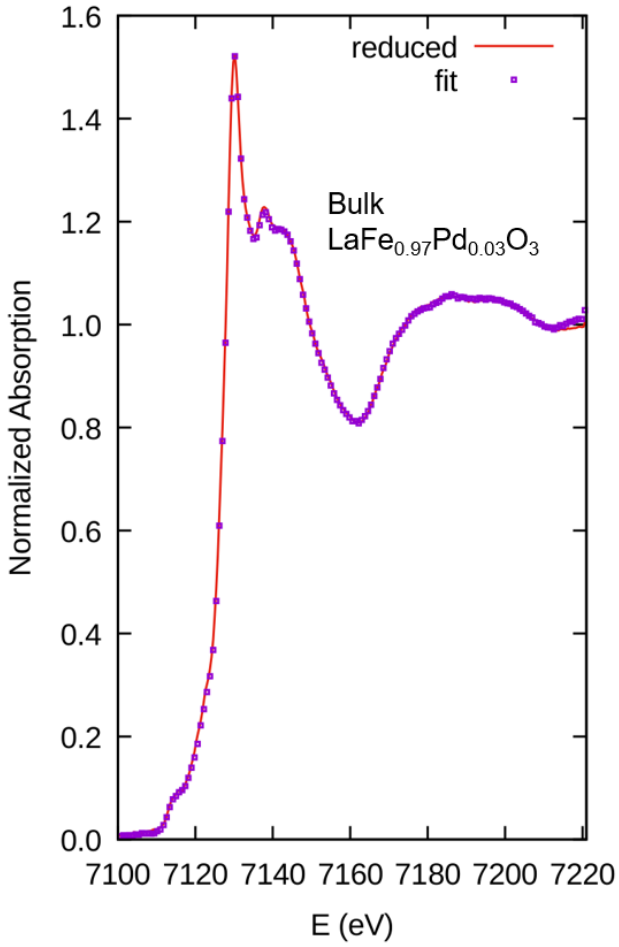

FIG. 6.11. XANES spectra at the Fe K edge of bulk $LaFe_{0.97}Pd_{0.03}O_3$ (1-wt% Pd) after reduction, and the linear combination of 10% bcc-Fe and 90% and 1-wt% (bulk $LaFeO_3$) before reduction (Fit), thus 10% of Fe of bulk $LaFeO_3$ is transformed to Fe^0 after reduction at 1073 K and without appreciably affecting the initial $LaFeO_3$ structure.

An investigation of model planar forms of the Pd-$LaFeO_3$ system previously showed that reduction of a 100-nm-thick, single crystal of $LaFe_{0.95}Pd_{0.05}O_{3-\delta}$ in 10% H_2 for

1 h at 1073 K can induce exsolution of the Pd from within 1 nm of the surface, producing a low density (of order 100 per square micrometer) of small (averaging 3 nm in diameter) Pd particles on the free surface [28]. The depth of exsolution and amount of Pd exsolved are thus comparable with the thickness of the $LaFeO_3$ conformal film and amount of Pd loaded onto the $MgAl_2O_4$ powder in the present study. The two forms of this system might be expected to perform similarly if most of the Pd that was loaded onto the porous catalyst could be incorporated into the $LaFeO_3$ film during catalyst preparation or subsequent oxidative treatment. The reverse process, dissolution of Pd particles into a 100-nm-thick, single crystal of $LaFeO_3$ was found to be much more difficult, however. Specifically, Pd particles that were 5-10 nm in diameter showed signs of localized reaction with the $LaFeO_3$ surface after oxidation in air for 1 h at 1073 K, but they did not disappear [28,29]. We hypothesize that the ability of the $LaFeO_3$ film in the present study to absorb Pd particles, many of which may have been smaller than 5-10 nm based on the reasonable expectation of a high dispersion in the freshly-prepared sample as well as the EXAFS results from the reduced samples, could have been enhanced by a more defective structure, including a possible Fe deficiency, since defects also appeared to facilitate Pd diffusion into bulk $LaFeO_3$ [28]. According to EDS, however, some large Pd particles were present in all the film samples, regardless of oxidation or reduction treatment. The possibility of a broad distribution of Pd particle sizes, ranging from 1-10 nm, seems likely given the fact that the CO chemisorption results, indicative of relatively low dispersions, are never-the-less not in quantitative agreement with the Pd particle sizes observed by HAADF-STEM or inferred from EXAFS results.

The likelihood that small Pd particles were reversibly exsolved and redissolved into the $LaFeO_3$ films upon reduction and reoxidation is supported by the CO-oxidation and methane-oxidation results, which roughly reproduce the previously observed rates and distinctive activation energy for this reaction on high-surface-area Pd-doped and Pd-impregnated $LaFeO_3$ [30]. In particular, the difference in activity between the oxidized (inactive) and reduced (active) states of the $LaFeO_3$ ALD-prepared $Pd/MgAl_2O_4$ samples shown in Figure 6.7(a) is consistent with the shift in light-off by at least 50 K to higher temperature for Pd-doped $LaFeO_3$ than Pd-impregnated $LaFeO_3$.

6.5 Conclusion

We have successfully deposited a thin conformal coating of $LaFeO_3$ on porous $MgAl_2O_4$ powder using ALD. We demonstrated that $LaFeO_3$ ALD-modified $MgAl_2O_4$ can function as a high-surface-area support for Pd, enabling a more practical form of self-regenerating catalyst than traditional bulk perovskite oxide supports can provide. This "smart" catalyst clearly opens perspectives for the employment of ALD also for incorporating Pd into the $LaFeO_3$ film in order to obtain a more uniform initial Pd distribution than was possible with the simple impregnation process used in the present study, which would allow a comprehensive evaluation of the full potential of this approach for improving metal utilization and increasing thermal stability.

6.6 References

1. Burch, R.; Loader, P. *Appl. Catal. B: Environ*. **1994,** *5*, 149-164.

2. Fornasiero, P.; Rao, G. R.; Kašpar, J.; L'erario, F.; Graziani, M. *J. Catal.* **1998,** *175*, 269-279.

3. Fornasiero, P.; Kašpar, J.; Sergo, V.; Graziani, M. *J. Catal.* **1999,** *182*, 56-69.

4. Sekizawa, K.; Widjaja, H.; Maeda, S.; Ozawa, Y.; Eguchi, K. *Catal. Today* **2000,** *59*, 69-74.

5. Farrauto, R. J. *Science* **2012,** *337*, 659-660.

6. Nishihata, Y.; Mizuki, J.; Akao, T.; Tanaka, H.; Uenishi, M.; Kimura, M.; Okamoto, T.; Hamada, N., *Nature* **2002,** *418*, 164-167.

7. Tanaka, H. *Catal. Surv. Asia* **2005,** *9*, 63-74.

8. Tanaka, H.; Uenishi, M.; Taniguchi, M.; Tan, I.; Narita, K.; Kimura, M.; Kaneko, K.; Nishihata, Y.; Mizuki, J. I. *Catal. Today* **2006,** *117*, 321-328.

9. Adijanto, L.; Padmanabhan, V. B.; Küngas, R.; Gorte, R. J.; Vohs, J. M. *J. Mater. Chem.* **2012,** *22*, 11396-11402.

10. Tian, C.; Zhu, X.; Abney, C. W.; Liu, X.; Foo, G. S.; Wu, Z.; Li, M.; Meyer III, H. M.; Brown, S.; Mahurin, S. M. *ACS Catal.* **2017,** *7*, 3388-3393.

11. Kwon, O.; Sengodan, S.; Kim, K.; Kim, G.; Jeong, H. Y.; Shin, J.; Ju, Y.-W.; Han, J. W.; Kim, G. *Nat. Commun.* **2017,** *8*, ncomms15967.

12. Katz, M. B.; Zhang, S.; Duan, Y.; Wang, H.; Fang, M.; Zhang, K.; Li, B.; Graham, G. W.; Pan, X. *J. Catal.* **2012**, *293*, 145-148.

13. Neagu, D.; Oh, T.-S.; Miller, D. N.; Ménard, H.; Bukhari, S. M.; Gamble, S. R.; Gorte, R. J.; Vohs, J. M.; Irvine, J. T. *Nat. Commun.* **2015,** *6*, 8120.

14. Oh, T.-S.; Rahani, E. K.; Neagu, D.; Irvine, J. T.; Shenoy, V. B.; Gorte, R. J.; Vohs, J. M. *J. Phys. Chem. Lett.* **2015,** *6*, 5106-5110.

15. Li, B.; Katz, M. B.; Duan, Y.; Du, X.; Zhang, K.; Chen, L.; Van der Ven, A.; Graham, G. W.; Pan, X. *Chem. Mater.* **2014,** *27*, 18-28.

16. Utriainen, M.; Kröger-Laukkanen, M.; Johansson, L.-S.; Niinistö, L. *Appl. Surf. Sci.* **2000,** *157*, 151-158.

17. Nieminen, M.; Sajavaara, T.; Rauhala, E.; Putkonen, M.; Niinistö, L. *J. Mater. Chem.* **2001,** *11*, 2340-2345.

18. Lee, S. W.; Kwon, O. S.; Han, J. H.; Hwang, C. S. *Appl. Phys. Lett.* **2008,** *92*, 222903.

19. Lie, M.; Nilsen, O.; Fjellvåg, H.; Kjekshus, A. *Dalton Trans.* **2009,** *3*, 481-489.

20. Nielsch, K.; Bachmann, J.; Daub, M.; Jing, J.; Knez, M.; Gösele, U.; Barth, S.; Mathur, S.; Escrig, J.; Altbir, D. *ECS Trans.***2007,** *11*, 139-148.

21. Rooth, M.; Johansson, A.; Kukli, K.; Aarik, J.; Boman, M.; Hårsta, A. *Chem. Vap. Deposition* **2008,** *14*, 67-70.

22. Rahmanipour, M.; Cheng, Y.; Onn, T.M; Donazzi, A.; Vohs, J.; Gorte, R. *J. Electrochem. Soc.* **2017,** *164*, F879-F884

23. Gosavi, P. V.; Biniwale, R. B. *Mater. Chem. Phys.* **2010,** *119*, 324-329.

24. A Borowski, M. *J. Phys. IV* **1997,** *7*, C2-259-C2-260.

25. Jentys, A. *Phys. Chem. Chem. Phys.* **1999,** *1*, 4059-4063.

26. Kuroda, H.; Yokoyama, T.; Kosugi, N.; Ichikawa, M.; Fukushima, T. *J. Phys., Colloq.* **1986,** *47*, C8-301-C8-304

27. Nishihata, Y.; Mizuki, J.; Tanaka, H.; Uenishi, M.; Kimura, M., *J. Phys. Chem. Solids* **2005,** *66*, 274-282.

28. Katz, M. B.; Graham, G. W.; Duan, Y.; Liu, H.; Adamo, C.; Schlom, D. G.; Pan, X. *J. Am. Chem. Soc.* **2011,** *133*, 18090-18093.

29. Li, B.; Katz, M. B.; Zhang, Q.; Chen, L.; Graham, G. W.; Pan, X. *J. Chem. Phys.* **2013,** *138*, 144705.

30. Malamis, S. A.; Harrington, R. J.; Katz, M. B.; Koerschner, D. S.; Zhang, S.; Cheng, Y.; Xu, L.; Jen, H.-W.; McCabe, R. W.; Graham, G. W. *Catal. Today* **2015,** *258*, 535-542.

CHAPTER 7. STABILIZATION OF PALLADIUM AND CERIA CATALYSTS BY ZIRCONIA OVERLAYERS PREPARED BY ALD FOR METHANE OXIDATION

Summary:

The effects of modifying Pd/Al_2O_3 and Pd/CeO_2 catalysts by ALD of ZrO_2 films were studied. For deposition on Pd/Al_2O_3 catalysts, TEM imaging, EDS mapping, and metal-dispersion measurements confirmed the presence of the thin 0.40-nm ZrO_2 film over both the Al_2O_3 support and the metal particles. The ZrO_2 films were surprisingly stable, only forming a well-crystallized phase above 1173 K. The ZrO_2 overcoating over the PdO particles created a semi-core-shell structure that stabilized the metal against sintering at 1073 K. Methane-oxidation rates on Pd/Al_2O_3 decreased with increasing catalyst calcination temperature but rates on the ZrO_2-covered surfaces increased with calcination temperature. For deposition on Pd/CeO_2, XPS was used to characterize the presence of the thin ZrO_2 film on the catalyst. Calcination of the unmodified CeO_2 caused a large decrease in surface area and increase in crystallite size between 673 and 1073 K; however, catalysts modified by 0.4-nm ZrO_2 films showed no change in surface area and CeO_2 crystallite size upon calcination to 1073 K. Methane-oxidation rates were slightly lower on the ZrO_2-covered catalyst when both materials were heated at 673 K but the activity of the ZrO_2-modified catalyst did not decrease with calcination temperature. Both catalysts showed good activity for the water-gas-shift reaction but the ZrO_2 film improved sulfur tolerance by preventing formation of cerium sulfates.

7.1 Introduction

Stability issues are of great importance in emissions-control catalysis, where high temperatures, susceptibility to poisons such as SO_2, and redox cycling can lead to severe deactivation due to sintering of metal catalyst particles and rare-earth supports [1]. At the same time, there is an increasing need for these catalysts to have low-temperature activity for methane oxidation because of the increasing concern for the global-warming properties of this pollutant [2]. Supported Pd is the material of choice for methane oxidation and contact between Pd and some oxides, such as ceria [3,4], is known to promote the reaction [5-7]. However, as noted above and in previous chapters, sintering of the Pd particles and CeO_2 at high temperatures is a problem. Another issue is the high susceptibility of ceria to sulfur poisoning. CeO_2 reacts with SO_2 to form sulfates under oxidizing conditions and cerium sulfates transform to an oxysulfide (Ce_2O_2S) under reducing conditions [8]. The oxysulfide prevents oxygen-transfer to the metal and effectively poisons reactions that require participation of both the CeO_2 and the metal phases [9].

A relevant approach to stabilizing metals involves depositing overlayers of an oxide by Atomic Layer Deposition (ALD) [10]. This approach has been used to stabilize Co catalysts against leaching for solution-phase reactions by covering the active component with an insoluble oxide, titania [11]. In another case, sintering of Pd/Al_2O_3 and Ni/Al_2O_3 catalysts was suppressed by depositing a relatively thick alumina coating, then heating the overlayers to introduce pores in the ALD overlayers [12,13]. It is noteworthy that the deposited material in these two examples, along with most of the examples reported in the literature, was an inert oxide similar to the support oxide. An example which deposited a

dissimilar, functionally active oxide involved the use of zirconia overlayers for stabilizing the surface area of perovskite cathodes in solid oxide fuel cells (SOFC) [14]. Gong, et al showed that deposition of zirconia overlayers onto the perovskite cathode prevented degradation of electrode performance, presumably by maintaining the initial high surface area of the perovskite.

The SOFC-electrode example is particularly interesting for emissions-control catalysis since ZrO_2 is already an important component in modern three-way catalysts. The high methane oxidation activity and good thermal stability from a previous study with core-shell catalysts, Pd@ZrO_2, suggests that ZrO_2 may act as a promoter for Pd when there is contact between the phases [15]. Also, discussed in previous chapters, zirconia is able to form solid solutions with ceria and stabilize the redox properties of ceria. Zirconia is a good oxygen-ion conductor but much less reactive than ceria with sulfur-containing molecules. It seems possible that zirconia could allow the transfer of oxygen from the gas phase, to and from ceria, while suppressing formation of cerium sulfates and oxysulfides.

Therefore, the present study was carried out to test the idea that thin zirconia films could enhance the catalytic properties of Pd-supported catalysts and CeO_2 catalysts. We will demonstrate that the ZrO_2 films create a 'semi-core-shell'-like structure on the oxidized PdO/Al_2O_3 catalyst while reducing the catalyst prior to ALD of ZrO_2 does not create this structure. Modification of the PdO/Al_2O_3 catalysts by ALD of ZrO_2 reduced the amount of Pd sintering observed after high temperature calcination and stabilized methane-oxidation rates. In addition, we will show that the same thickness of ZrO_2 film will improve the structural and thermal stability of a CeO_2 support by suppressing the sintering of the

CeO_2 crystallites upon calcination at elevated temperatures. ALD-modified, Pd/CeO_2 catalysts remained catalytically active for methane oxidation and water-gas-shift reaction. Finally, the ALD-modified catalyst was much more easily regenerated after SO_2 and CO poisoning.

7.2 Experimental Methods

The Pd/Al_2O_3 catalysts were prepared by incipient wetness onto a γ-Al_2O_3 (Strem Chemicals, Inc.). The ceria, zirconia, and ceria-zirconia solid solution powder used in this study was prepared by precipitating an aqueous solution of cerium salt and/or zirconium salt with excess ammonium hydroxide (NH_4OH, Fisher Scientific). The full procedures of the incipient wetness method and precipitation by NH_4OH method are described in Chapter 2. ALD of ZrO_2 was performed using the same customized setup described in Chapter 2. The ZrO_2 precursor chosen for the present study is tetrakis(dimethyl amino)-zirconium (TDMZ, Sigma Aldrich) as it has a high vapor pressure at room temperature. It should be noted that this precursor can decompose upon exposure to air or moisture. In a typical ALD cycle, the TDMZ precursor was heated to 363 K to produce a vapor pressure of approximately 2 Torr. The TDMZ vapor was then allowed to flow into the evacuated sample chamber, which was held at 453 K, for 300 s. The sample chamber was then evacuated and exposed to water vapor (~100 Torr) for 300 s. The procedure was repeated as often as desired.

The amount of ZrO_2 deposited on the sample was determined gravimetrically as a function of ALD cycles. CO Chemisorption, BET surface-area measurements, XRD, FTIR,

XPS, STEM and EDS, and in-situ TEM were used to characterize the samples. Steady-state, CH_4 oxidation reaction was used to probe the catalysts. CH_4 and O_2 fixed at 3.8 Torr (0.5-vol.%) and 38 Torr (5-vol.%) respectively were carried to the sample by a He carrier gas. The total flow rate of He was kept at 110 mL/min. The steady-state WGS rates were also determined in the same flow reactor with partial pressures of CO and H_2O both at 25 Torr (3.3%). The total flow rate of He, in this case, was kept at 60 mL/min. The mass of catalysts used in every rate measurements were 0.10 g, and differential conversions were maintained in all cases. SO_2 poisoning was accomplished by passing 5 mmols of SO_2, generated by reacting sodium bisulfite ($NaHSO_3$, Sigma Aldrich) with sulfuric acid (H_2SO_4, Fisher Scientific), over the catalyst using He in the same flow reactor used for CH_4 oxidation and WGS reactions. The catalysts were then oxidized at various temperatures before again being tested for WGS activity.

7.3 Results

7.3.1 Stabilization of Pd Catalysts by ALD ZrO_2

The growth rate of the ZrO_2 films on PdO/Al_2O_3 was determined by measuring the weight of the catalyst as a function of the number of TDMZ-H_2O cycles, with the results shown in Figure 7.1. The mass increased linearly with the number cycles in this coverage range, increasing by 21-wt.% after 50 cycles. Assuming that the ZrO_2 film deposits uniformly and with a density equal to that of tetragonal ZrO_2, the film growth was 0.02 nm/cycle (10 Zr atoms/nm^2 after 50 cycles), similar to other literature reports. Finally, the growth curve here was measured with Pd left in the oxidized state prior to ALD-ZrO_2 but

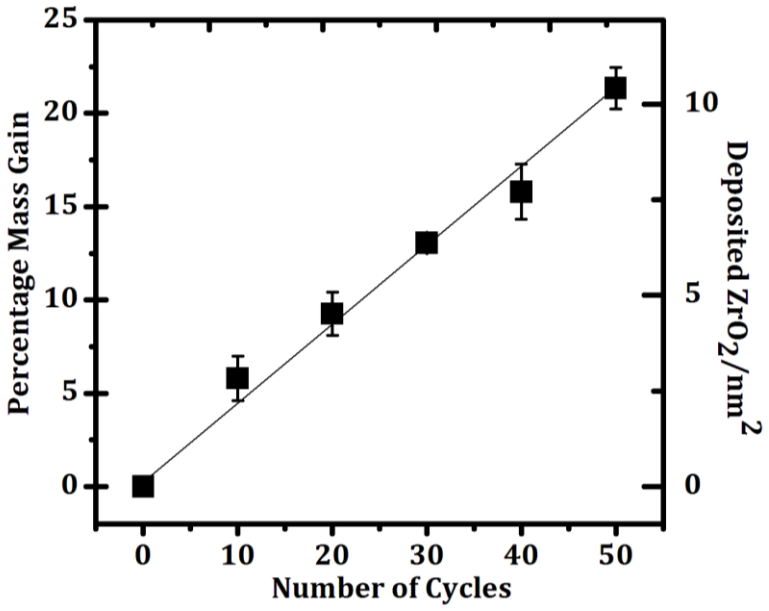

FIG. 7.1. Mass change as a function of the number of ALD cycles on a PdO/Al_2O_3 catalyst which had an initial surface area of 100 m^2/g.

similar ZrO_2 loadings were obtained after 50 cycles when ZrO_2 was grown on a reduced sample. The samples were also characterized using BET. As shown in Table 7.1, the surface area decreased from 100 m^2/g to 66 m^2/g after 50 deposition cycles. The addition of 0.21 g ZrO_2/g catalyst would be expected to decrease the specific surface area to 83 m^2/g simply due to the change in mass of the sample. An additional loss in specific surface area would come from changing the average pore size of the support. The surface area was essentially unaffected by increasing the calcination temperature from 773 to 1073 K.

Scanning transmission electron microscopy (STEM) and EDS mapping also offered insights into the surface coverage of ZrO_2 on PdO/Al_2O_3. A comparison of the ALD-coated and uncoated sample after 773 K and 1073 K calcination is shown in Figure 7.2 (a)-(d) The PdO particles are of comparable sizes, about 5 nm in diameter, in both the

ZrO_2-coated (Figure 7.2(a)) and uncoated (Figure 7.2(c)) samples after 773 K calcination. However, the sizes of PdO particles with the ZrO_2 protective layer remained unaffected after heating to 1073 K in air (Figure 7.2(b)). In contrast, the size of particles almost doubled in the uncoated PdO/Al_2O_3 sample after the same treatment. This observation is consistent with previous TEM analysis after ALD of a metal oxide was carried out [11]. In addition, sintering or signs of aggregation were frequently observed by the TEM for PdO/Al_2O_3 calcined at 1073 K while these events were rarely observed with $50ZrO_2$-PdO/Al_2O_3.

Using high angle annular dark field (HAADF) imaging, the ZrO_2 surface layer may be distinguished from Al_2O_3 due to the atomic number differences between Zr and Al, as shown in Figure 7.2(e)-(f). Here, the Al_2O_3 support appears to be covered by a uniform ZrO_2 surface layer with thickness of around 1 nm in the fresh sample without calcination. EDS elemental maps, including Pd, Zr and O, on the same sample, shown in Figure 7.3, confirm that the brightness variation on Al_2O_3 is due to the presence of Zr; and they further confirm that the PdO particles are fully covered by the ZrO_2 layer, due to the coincidence of Zr and Pd in the spectra. It should be noted that Zr species, when observed under the TEM, appeared in three different forms: a thin ZrO_2 layer on the Al_2O_3 surface, a thin layer around the PdO particle, and sometimes small chunks.

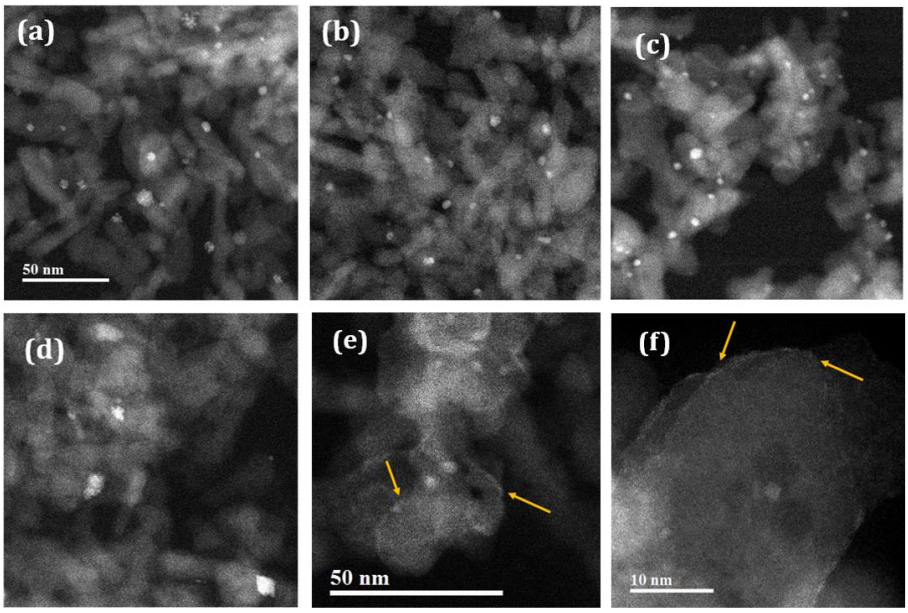

FIG. 7.2. STEM results for PdO/Al_2O_3 and $50ZrO_2$-PdO/Al_2O_3 catalysts after various pretreatments: (a) $50ZrO_2$-PdO/Al_2O_3 calcined at 773 K; (b) $50ZrO_2$-PdO/Al_2O_3 calcined at 1073 K; (c) PdO/Al_2O_3 calcined at 773 K; (d) PdO/Al_2O_3 calcined at 1073 K; (e) and (f) $50ZrO_2$-PdO/Al_2O_3 uncalcined (fresh). Arrows in (e) and (f) indicate regions of high contrast due to the ZrO_2 overlayer.

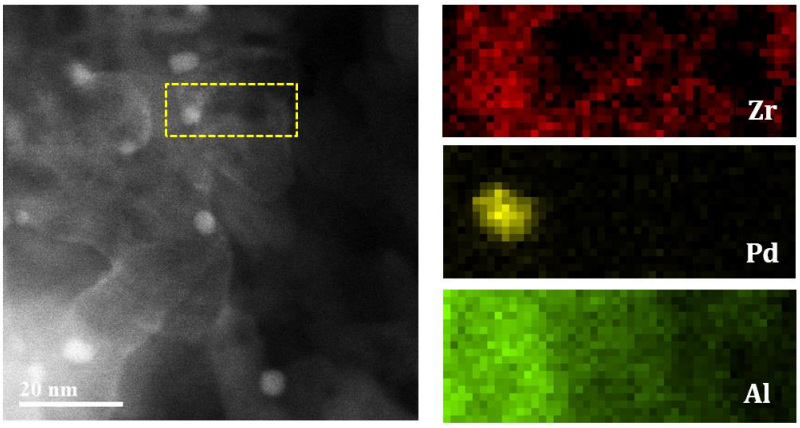

FIG. 7.3. STEM results for uncalcined (fresh) $50ZrO_2$-PdO/Al_2O_3 catalysts with EDS mapping of Al, Zr, and Pd.

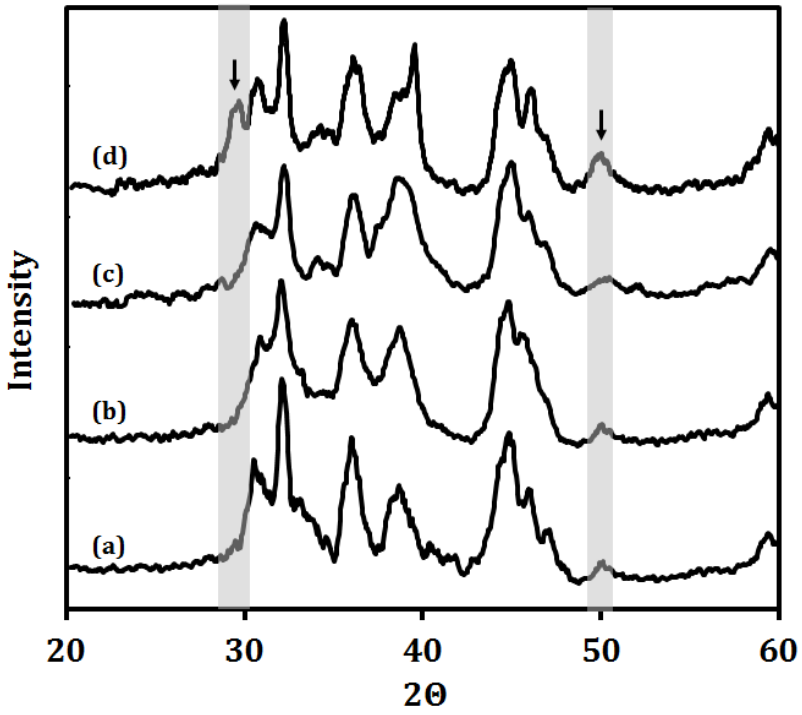

FIG. 7.4. XRD patterns of the ALD-coated, $50ZrO_2$-PdO/Al_2O_3 sample after calcination to various temperatures: (a) as deposited; (b) 773 K; (c) 1073 K; (d) 1173 K. Characteristic peaks for tetragonal ZrO_2 are marked by the grey lines.

XRD patterns from Figure 7.4 confirmed that the ZrO_2 layers were initially amorphous and not crystalline. We observe that, upon heating to 773 K and 1073 K (Figure 7.4(b) and 7.4(c) respectively), there were no observable features due to crystalline ZrO_2 from the ALD ZrO_2 samples. However, when the sample was heated to 1173 K in air (Figure 7.4(d)), we observe small peaks around 30 and 50 degrees 2θ, aligned with the characteristic diffraction patterns of a tetragonal ZrO_2 phase. The corresponding size of ZrO_2 crystallites was calculated to be around 5 nm based on the width of the peak at around 30 degrees at half maximum from the Scherrer equation. This result is consistent with the formation of thin ZrO_2 layer that forms particles upon high temperature calcination. *In-situ*

TEM observations revealed that the thin ZrO_2 layer on the Al_2O_3 surface actually begins to migrate and form into nano-particles at much lower temperature, 773 K, as shown in Figure 7.5. Here, since the area imaged clearly contains no PdO particles initially, the particles that are observed to form with increasing time and temperature are certainly zirconia. These observations provide direct evidence for the effect of calcination temperature on catalytic activity, presented below. Finally, we also note that the ZrO_2 surface layer was not observed in many areas examined by TEM, presumably because it was too thin to detect by either HAADF imaging or EDS.

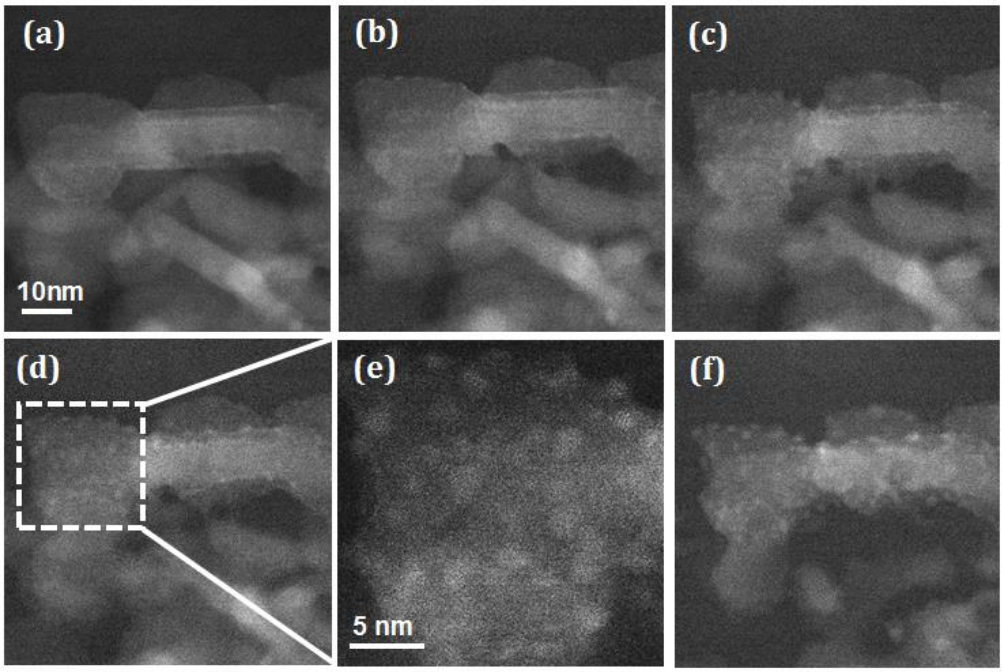

FIG. 7.5. Sequential STEM images of uncalcined (fresh) $50ZrO_2$-PdO/Al_2O_3 catalysts obtained in-situ under 150 Torr O_2 in the TEM gas cell at a temperature of: (a) 573 K, (b)-(c) 773 K for 0 and 3 min respectively, (d)-(e) 873 K, and (f) 973 K.

Methane oxidation was used to probe the effect of ZrO_2 films on the catalytic performance of Pd/Al_2O_3 catalysts. Figure 7.6(a) is an Arrhenius plot showing rates for the unmodified PdO/Al_2O_3 sample following calcination at 773 K, 973 K, and 1073 K. The activation energies are roughly the same, 90 kJ/mol, but the rates decrease noticeably as the calcination temperature increased. The catalyst calcined at 773 K exhibited rates that were approximately five times higher than the catalyst calcined at 1073 K. This decrease in rates is at least partially explained by the increase in Pd particle size with calcination temperature observed in the TEM measurements discussed earlier. Dispersion measurements, reported in Table 7.2, also indicate a decrease in the available Pd surface area, decreasing from 33% to 24% after heating the catalyst from 773 K to 1073 K. Clearly, the decrease in rates was significantly greater than the decrease in dispersion, implying that other factors must also be involved. Methane-oxidation rates have been reported to depend on Pd crystallite size and the presence of support hydroxyls on Al_2O_3, but increased calcination temperature appears to influence rates by changing more than just the metal surface area [16-21].

Table 7.1: BET surface-areas of samples used in this study as a function of calcination temperature.

	BET Surface Area (m^2/g)	
Calcination Temp. (K)	**PdO/Al_2O_3**	**$50ZrO_2$-PdO/Al_2O_3**
773	100	66
973	100	66
1073	100	70

Rates for the sample prepared with 50 ALD cycles of ZrO_2 deposited onto the oxidized PdO/Al_2O_3 catalyst are shown in Figure 7.6(b). The catalyst calcined at 773 K, designated $50ZrO_2$-PdO/Al_2O_3 (773), showed very low rates. Whereas the unmodified PdO/Al_2O_3 catalyst calcined at 773 K exhibited a rate of 10^{19} CH_4/(s·g Pd) at a temperature of 500 K, the $50ZrO_2$-PdO/Al_2O_3 (773) sample was only able to achieve this rate at 530 K through extrapolation. However, the activity of this catalyst increased dramatically with increasing calcination temperature. After heating to 1073 K, the temperature at which the rate was 10^{19} CH_4/(s·g Pd) was 485 K, indicating that $50ZrO_2$-PdO/Al_2O_3(1073) catalyst was more active than even fresh PdO/Al_2O_3. Since the STEM results indicated that the Pd particles were covered by the ZrO_2 film following ALD, it is likely the increased rates are due to breaking up of that ZrO_2 film. Again, changes in the rates were not reflected by changes in the dispersions measured by CO adsorption, shown in Table 7.2. The relatively high activity of the $50ZrO_2$-PdO/Al_2O_3 (1073) catalyst must be due in part to interactions with ZrO_2.

Table 7.2: Pd metal dispersions of samples used in this study as a function of calcination temperature.

	Pd Dispersion (%)		
Calcination Temp. (K)	**PdO/Al_2O_3**	**$50ZrO_2$-PdO/Al_2O_3**	**$50ZrO_2$-Pd/Al_2O_3**
773	32.9	10.6	18.5
973	29.8	10.8	-
1073	24.2	13.2	18.6

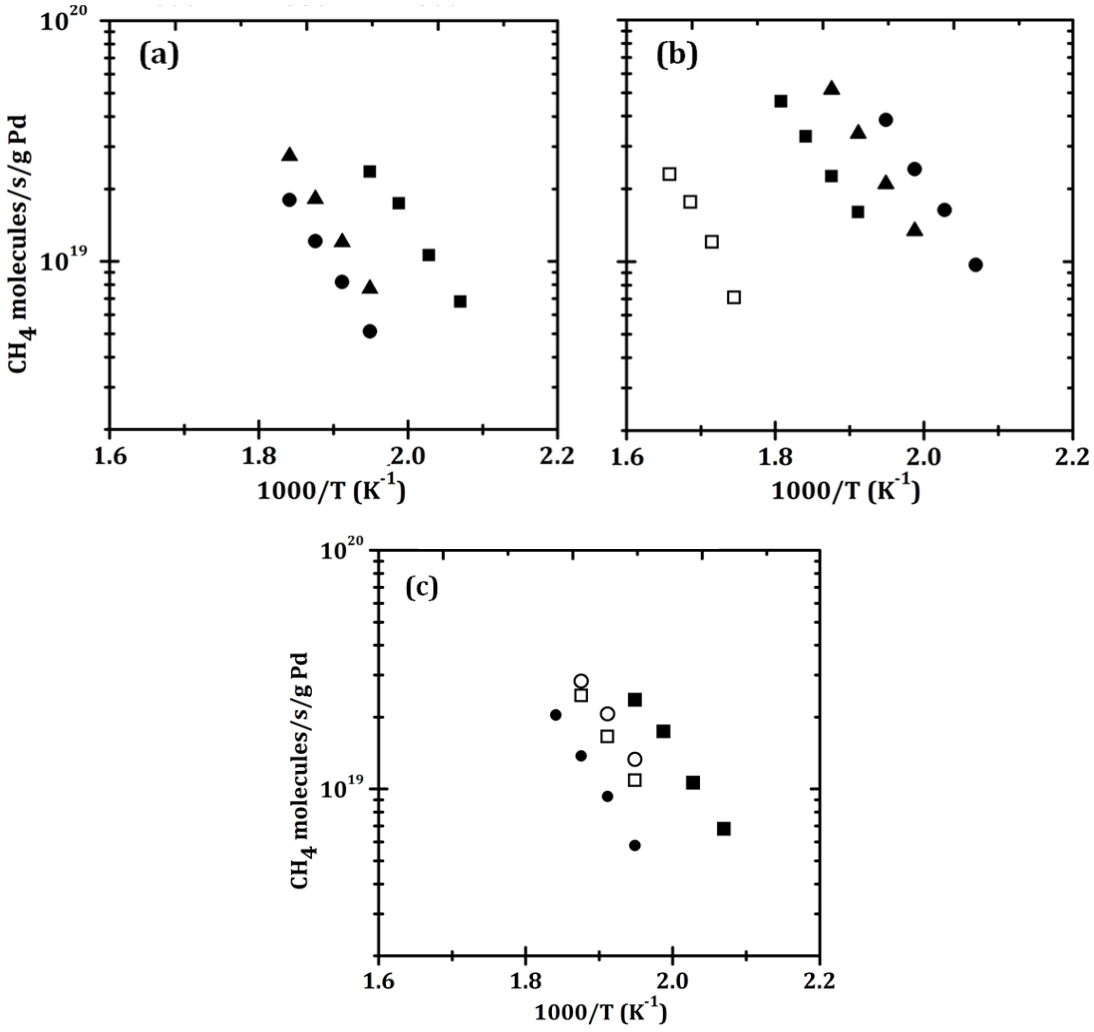

FIG. 7.6. Steady-state, differential reaction rates for methane oxidation in 0.5% CH_4 and 5% O_2. (a) Rates on PdO/Al_2O_3 after calcination to the following temperatures: (■) – 773 K, (▲) – 973 K, and (●) – 1073 K. (b) Rates on $50ZrO_2$-PdO/Al_2O_3 after calcination to the following temperatures: (□) – uncalcined, (■) – 773 K, (▲) – 973 K, and (●) – 1073 K. (c) Rates on $50ZrO_2$-Pd/Al_2O_3, in which ZrO_2 was deposited on the reduced catalysts by ALD, after calcination at (□) – 773 K and (○) – 1073 K. Data for PdO/Al_2O_3 calcined (■) – 773 K and (●) – 1073 K are shown for comparison.

Methane-oxidation rates for a catalyst prepared by 50 ALD cycles of ZrO_2 onto reduced Pd/Al_2O_3 are shown in Figure 7.6(c). Rates for the unmodified PdO/Al_2O_3 after calcination at 773 and 1073 K are shown for comparison. Interestingly, rates on the

$50ZrO_2$-Pd/Al_2O_3 samples were the same when calcined at either 773 or 1073 K. Rates were somewhat lower than for the unmodified Pd/Al_2O_3 calcined at 773 K but were stable. The measured dispersions on this catalyst were higher than that measured on $50ZrO_2$-PdO/Al_2O_3 catalysts and did not change with calcination temperature. We suggest that, in this case, the ZrO_2 film did not grow on the metallic Pd, so that there was no need to "break up" the oxide film. However, the presence of the ZrO_2 film on the Al_2O_3 does appear to thermally stabilize the metallic Pd particles.

7.3.2 Stabilization of Ceria Support by ALD ZrO_2

In this study, 20 ALD cycles of ZrO_2 (11-wt%) was deposited on Pd/CeO_2 catalyst (hereby designated as $20ZrO_2$-Pd/CeO_2), which initially has a surface area of 47 m^2/g. The weight gained corresponds to a film growth rate of 0.02 nm/cycle, the same value determined in the study above on Pd/Al_2O_3 catalyst. Various techniques were then used to characterize the Pd/ceria catalyst before and after the ALD. First, the presence of ZrO_2 on the ALD-treated sample was demonstrated by XPS. Figure 7.7 shows the Ce 3d and Zr 3d XPS spectra of this sample after calcination to 673 K. The Ce 3d spectra are indicative of a completely oxidized sample, with all of the Ce present in the +4 oxidation state [24]. The Zr 3d doublet shows the typical binding energy of ZrO_2 and a broadening of the signal probably due to differential charging of the powdered sample [25,26].

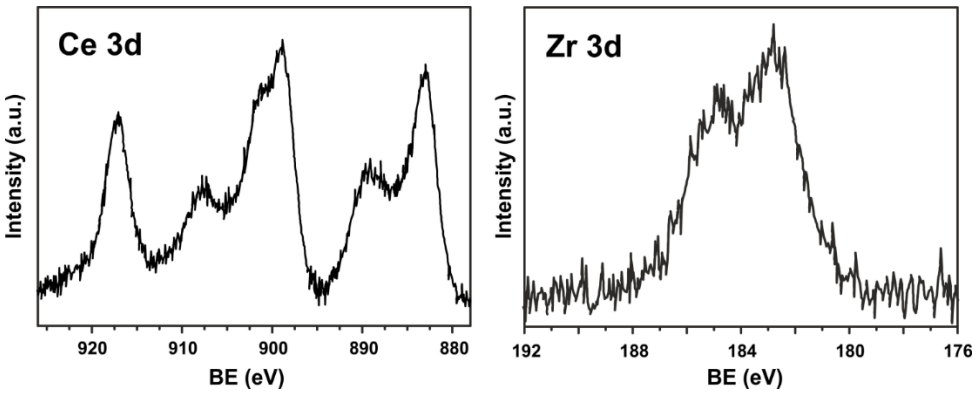

FIG. 7.7. XPS spectra of Ce 3d and Zr 3d for 20ZrO_2-Pd/CeO_2 after calcination to 673 K.

BET surface areas were measured on the Pd/ceria, Pd/ceria-zirconia, and ZrO_2-modified Pd/ceria samples as a function of calcination temperature, with results shown in Table 7.3. The surface area of the fresh catalyst after calcination at 673 K was 47 m^2/g. The surface area after ALD ZrO_2 was 38 m^2/g after calcination to 673 K to remove the ligands. Most of the lost specific surface area is accounted for by the increase in sample mass (47 m^2/1.11 g = 42 m^2/g). The effect of the 0.4-nm ZrO_2 film on the evolution of the Pd/ceria surface area with increasing calcination temperature was surprisingly large. As demonstrated in Table 7.3, the specific surface area of the unmodified Pd/CeO_2 catalyst declined steadily with increasing calcination temperature, to a value of 18 m^2/g after heating to 1073 K. On a percentage basis, the loss in surface area of the Pd/ceria-zirconia sample was similar, decreasing from 70 to 30 m^2/g after heating to 1073 K, demonstrating that the solid solution is not qualitatively different from CeO_2 with regards to its sintering resistance. However, the ZrO_2-covered Pd/ceria showed no change in surface area with increasing calcination temperature, remaining 39 m^2/g after heating to 1073 K.

Table 7.3: Surface areas of the samples as a function of calcination temperature

	BET Surface Area (m^2/g)		
Calcination Temp (K)	**Pd/CZ**	**Pd/CeO_2**	**20ZrO_2-Pd/CeO_2**
673	70	47	38
773	63	42	41
873	48	36	42
973	40	30	40
1073	30	18	39

A further indication of the stabilizing effect of the 0.4-nm ZrO_2 film is shown by the XRD data in Figure 7.8. The XRD patterns of the unmodified and ZrO_2-covered Pd/ceria after calcination at 673 K were indistinguishable. The patterns showed only broad peaks associated with the fluorite structure of ceria and no evidence for either Pd or ZrO_2. For this Pd loading, no peaks associated with Pd are expected. The absence of ZrO_2 peaks implies that the ZrO_2 remains amorphous or is present as a thin film. Figure 7.8 is a plot of the width at half maximum for the (111) peak at 28 degrees 2θ, along with the corresponding crystallite size calculated from that peak width using the Scherrer Equation, for both samples as a function of calcination temperature. Not surprisingly, the XRD patterns of the unmodified Pd/ceria sharpened with increasing calcination temperature, implying that sintering caused an increase in the crystallite size from an initial value of 18 nm to 32 nm after calcination at 1073 K. This is in agreement with the loss in surface area this sample experienced. However, within experimental uncertainty, the XRD patterns of the ZrO_2-modified Pd/ceria were unaffected by increasing calcination temperature.

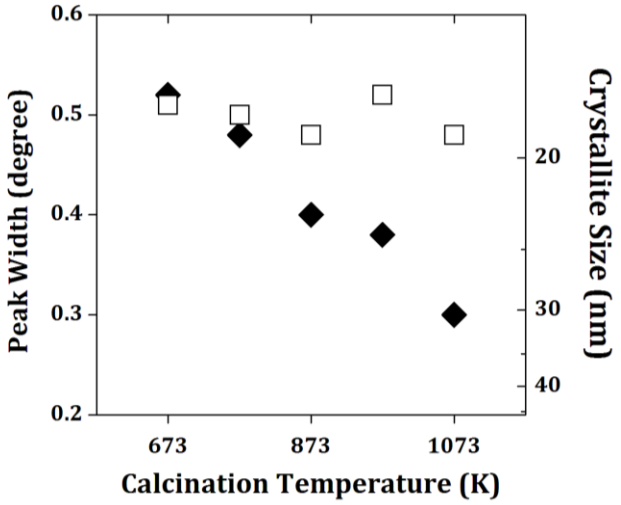

FIG. 7.8. Peak width at half maximum height and crystallite size obtained from XRD patterns of (□) – 20ZrO_2-Pd/CeO_2 and (♦) – Pd/CeO_2 sample at 2Θ = 28.54° as a function of calcination temperature.

Since the ZrO_2 coatings will also affect the Pd, dispersion measurements were performed on the Pd/ceria and ALD-modified Pd/ceria catalysts as a function of calcination temperature using CO chemisorption at room temperature, with results shown in Table 7.4. The catalysts were first reduced in H_2 at 673 K before cooling to room temperature and measuring CO uptakes. The reduction step is necessary to reduce PdO to Pd and therefore to prevent reaction of CO to CO_2, which could then adsorb on the reduced ceria surface. The Pd dispersion was initially 50% on the unmodified catalyst but this reduced steadily to 30% after calcination 1073 K. On the ALD prepared catalyst, the initial dispersion was only 23% but this increased to 28% after calcination to 773 K and remained constant at this value. We suggest that the dispersions were lower on the modified catalyst because the

Pd was partially covered by ZrO_2. The small increase with increasing calcination temperature was likely due to partial removal of the ZrO_2 film.

Table 7.4: Pd dispersions as a function of sample calcination temperature.

	Pd Dispersion (%)	
Calcination Temp (K)	**Pd/CeO_2**	**$20ZrO_2$-Pd/CeO_2**
673	50	23
773	40	28
873	35	30
1073	30	28

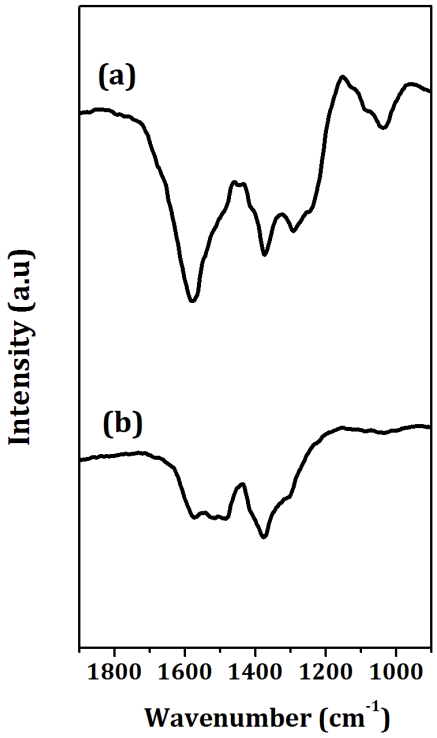

FIG. 7.9. DRIFTS spectra obtained for (a) $20ZrO_2$-Pd/CeO_2 and (b) Pd/CeO_2, after exposure to 10% CO in flowing He at 573 K for 10 minutes.

To determine how the presence of the ZrO_2 film might affect the surface properties of the Pd/ceria catalyst, we performed FTIR measurements following catalyst reductions in CO. The Pd/ceria and ZrO_2-modified Pd/ceria catalysts were first calcined in air at 673 K to ensure that they were completely oxidized, then placed in the FTIR cell and reduced in 10% CO-He mixtures. Spectra were collected after flushing in dry He. For unmodified Pd/ceria, reduction of PdO and CeO_2 in CO produces CO_2, which in turn reacts with the reduced ceria to form carbonates [27]. This is shown in spectrum of Figure 7.9(a), which exhibits broad features between 1300 and 1700 cm^{-1}. In the analogous spectrum of the ZrO_2-modified catalyst, Figure 7.9(b), these peaks are significantly reduced in intensity. Since we will later show that the ZrO_2-modified catalyst is catalytically active, we suggest that the ZrO_2 film prevents formation of cerium carbonates by covering a significant fraction of the ceria surface.

The effect of modifying the catalyst by ALD of ZrO_2 was examined using methane oxidation with 0.5% CH_4 and 5% O_2. Differential rates for the unmodified and ZrO_2-modified catalysts are shown in Figure 7.10 following catalyst calcination to either 673, 973, or 1073 K. Considering the results on unmodified Pd/ceria, Figure 7.10(a), there is a progressive decline in activity with calcination temperature, as indicated by the need to go to increasingly higher temperatures to achieve the same rates. The sample calcined at 1073 K required temperatures that were approximately 100 K higher in order to achieve a particular rate compared to the catalyst calcined at 673 K. At a given temperature, the rate decreased by more than an order of magnitude. Since the decrease in rates was much greater than the decrease in ceria surface area or the decrease in Pd dispersion, other factors must

also be involved. Interestingly, the activation energy remained 90±10 kJ/mol and did not change with calcination temperature. Methane-oxidation rates have been reported to depend on Pd crystallite size, support reducibility, and support-metal interfacial contact area [28-31]. Apparently, increasing the calcination temperature changed more than just the surface area and dispersion and these changes dramatically reduced the methane oxidation activity.

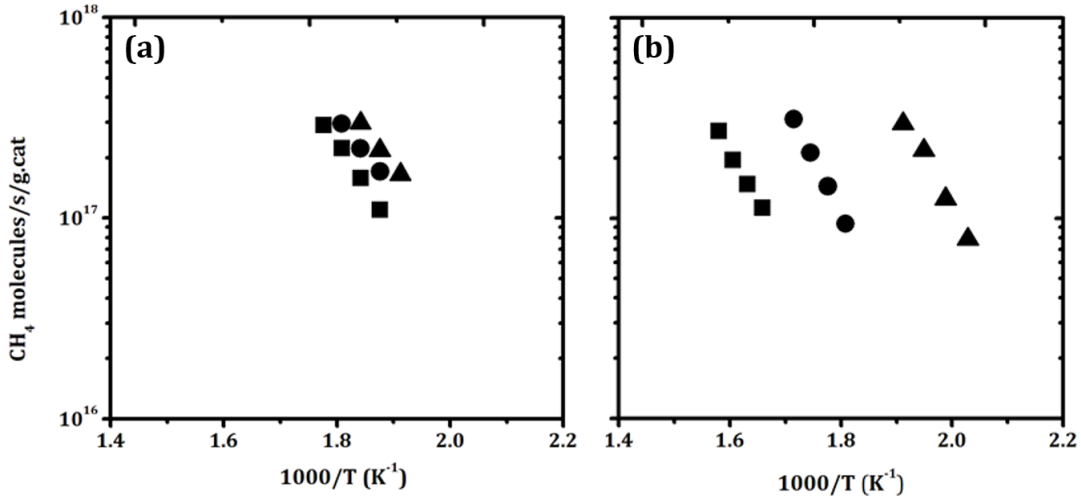

FIG. 7.10. Steady-state, differential methane oxidation rates in 0.5% CH_4 and 5% O_2. (a) CH_4 oxidation rates on $20ZrO_2$-Pd/CeO_2 after calcination to the following temperatures: (▲) – 673 K, (●) – 973 K, and (■) – 1073 K. (b) Rates on Pd/CeO_2 after calcination to the following temperatures: (▲) – 673 K, (●) – 973 K, and (■) – 1073 K.

The activity of the ALD-prepared catalyst is somewhat lower than that of the fresh Pd/ceria, as shown in Figure 7.10(b). For catalysts calcined at 673 K, the rates were a factor of about two lower than that of the unmodified catalyst; the activation energy, 65 kJ/mol, was also lower. However, the rates on the modified catalyst did not change significantly with calcination temperature. Because of this, the ALD prepared catalyst exhibited rates

that were almost an order of magnitude higher after the two catalysts were calcined at 1073 K, even though the Pd dispersion on the ALD prepared catalyst was lower. Again, other factors must be important for determining the activity of these materials.

Table 7.5: Steady-state, water-gas-shift activity for the unmodified and ZrO_2-modified Pd/ceria and after SO_2 poisoning and oxidative regeneration.

Water Gas Shift Activity at 573 k (10^{16} CO molecules/s/g.cat)

	Fresh Activity	**After SO_2 Poisoning**	**Regeneration**
$20ZrO_2$-Pd/CeO_2	99	17	80
Pd/CeO_2	100	1.3	2.8

The earlier observation that carbonate formation is suppressed on the ZrO_2-modified catalyst led us to consider whether the ZrO_2 layer might also reduce the effects of sulfur poisoning. Sulfur poisoning has previously been shown to have a very large effect on the WGS activity of Pd/ceria [9] and it has been suggested that this decrease in activity is related to the loss in OSC in working catalysts. Therefore, we measured WGS rates on unmodified and ZrO_2-modified Pd/ceria, before and after exposure to SO_2. Rates were measured at 573 K in 25 torr each of H_2O and CO and the catalysts were poisoned by simply exposing them to a 5 mmol "slug" of SO_2 at 573 K. Because Pd can also be poisoned by sulfur but regenerated by oxidation treatments, the poisoned catalysts were oxidized in flowing, 5% O_2 at 973 K for 30 min. The WGS rates on the two catalysts after these pretreatments are reported in Table 7.5. Prior to SO_2 exposures, the two catalysts exhibited

nearly identical WGS rates. After SO_2 exposure, both catalysts lost most of their activity. However, the ZrO_2-modified sample was nearly completely restored after oxidation at 973 K, while the unmodified Pd/ceria remained inactive.

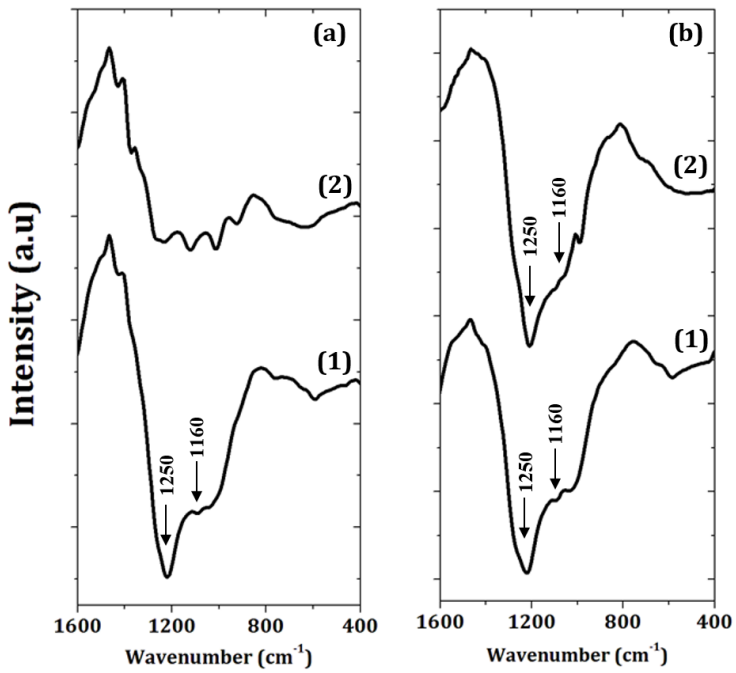

FIG. 7.11. DRIFTS spectra of (a) $20ZrO_2$-Pd/CeO_2 and (b) Pd/CeO_2 after (1) exposure to a slug of SO_2 at 573 K for 30 minutes and (2) heating in 5% O_2 at 973 K for 30 minutes.

To better understand the differences, we performed FTIR measurements on the two catalysts after the above pretreatments, with results shown in Figure 7.11. After SO_2 poisoning at 573 K, the FTIR spectrum of Pd/ceria showed intense bands at 1160 and 1250 cm^{-1}. These can be identified as being due to sulfates on the ceria. Heating in 5% O_2 at 973 K for 30 min did not significantly change the spectrum. The ZrO_2-modified catalyst also showed strong bands due to sulfate formation after SO_2 exposure; however, the intensity

of these bands decreased dramatically upon oxidation at 973 K. While it was not possible for us to quantify the SO_2 coverages based on the FTIR results, it appears that sulfates can be formed on the ZrO_2 but that these decompose much more readily.

7.4 Discussion

Atomic Layer Deposition is receiving an increasing amount of attention as a way of preparing and modifying catalysts. The structure of the oxide films prepared by ALD is clearly very different from what could be achieved by adding an oxide promoter using infiltration or co-precipitation methods. Firstly, most other methods of adding oxides tend to form particles or are limited to forming a single oxide monolayer while ALD allows formation of thin films of varying thicknesses. An added advantage is that it is a convenient technique of preparing materials in which the active metal and oxide promoters are in close contact. This is observed in the present work where the ZrO_2 films formed on PdO and promoted methane oxidation activity. The inability of ZrO_2 film to deposit on Pd also suggests that ALD may be possible to deposit promoters over only selected parts of the catalyst. The present study did not explore compositional changes, but ALD clearly allows deposition of a wide range of materials.

The reason for the enhanced methane oxidation rates on the zirconia-promoted catalysts is uncertain. The literature shows that methane oxidation on Pd is a complex reaction that likely involves C-H activation on sites in the vicinity of both metallic Pd and PdO.[27] Although there is strong evidence that C-H bond activation is structure sensitive in Pd, there is controversy over whether or not particle size influences reaction rates, with

some reporting that larger particles exhibit higher specific rates and others reporting that rates are strictly proportional to the surface area of the Pd or PdO. There is agreement that PdO must be present in the active phase; but the stability of PdO, along with the reaction rate for methane, can be influenced the oxide support.[24-26] In past work on Pd@ZrO_2 core-shell catalysts, evidence was presented that the ZrO_2 in contact with the Pd is reducible and that this reducibility is somehow responsible for stabilizing PdO and enhancing reaction rates.[11]

The work then extends that idea in that the deposited ZrO_2 film can also interact with the oxide phase, CeO_2 in this case. Ceria-zirconia mixed oxides are well known to exhibit enhanced reducibility. Therefore, some of the enhanced rates in the present study may result from the contact between CeO_2 and ZrO_2. The fact that a ZrO_2 film, only one unit cell in thickness, can so dramatically stabilize the surface area and crystallite size of polycrystalline CeO_2 was a surprise. Previous reports that SOFC cathode performance could be stabilized by ZrO_2 overlayers used much thicker films, on the order of 5 nm, and only inferred stabilization of the surface area based electrode performance [14]. It seems unlikely that the ZrO_2 film has significant mechanical strength, so that the mechanism by which ZrO_2 stabilizes CeO_2 is likely associated with changing the surface energy of the system. Sintering results from a material minimizing its free energy by decreasing the surface energy. However, if the surface energy is already low, the driving force for sintering will decrease. We suggest a mechanism of this type must be involved in the surface stabilization of CeO_2 by ZrO_2. The ZrO_2 must be decreasing the surface energy of the ceria.

The present study also demonstrated that thin oxide films deposited by ALD can provide a very effective chemical barrier to prevent poisoning of a catalyst, without significantly affecting catalytic activity for the desired reaction. Here, we demonstrated that the ZrO_2 film improved the sulfur tolerance of CeO_2 but the concept may apply in other cases as well. The ability of ALD to form a uniform, continuous film over the entire catalyst surface makes it uniquely capable of preparing materials with these properties. Clearly, the field of designing high-surface area catalysts by ALD is still in its infancy, with many more advantages waiting to be found.

7.5 Conclusion

Modification of PdO/Al_2O_3 catalyst and Pd/CeO_2 catalyst by thin, ALD-deposited ZrO_2 films leads to several improvements in the catalyst performance. The ZrO_2 films forms a semi-core shell structure around PdO particles and stabilize PdO against sintering at high temperatures and enhance the methane-oxidation activity of these catalysts following high-temperature calcination. The ZrO_2 films also stabilize the surface area and crystallite size of CeO_2, and they improve the sulfur tolerance of the catalysts by preventing formation of cerium sulfates. The work further demonstrates that ALD is an important tool for catalyst synthesis.

7.6 References

1. McCarty, J. G.; Malukhin, G.; Poojary, D. M.; Datye, A. K. *J. Phys. Chem. B*, **2005**, 109, 2387-2391.

2. Farrauto, R. J. *Science*, **2012**, 337, 659-660.

3. Colussi, S.; Gayen, A.; Camellone, M.F.; Boaro, M.; Llorca, J.; Fabris, S.; Trovarelli, *A. Angew. Chem. Int. Edit.*, **2009**, 48, 8481.

4. Cargnello, M.; Jaen, J. J. D.; Garrido, J. C. H.; Bakhmutsky, K.; Montini, T.; Gamez, J. J. C.; Gorte, R. J.; Fornasiero, *P. Science*, **2012**, 337, 713-717.

5. Forzatti, P.; Groppi, *G. Catal Today*, **1999**, 54, 165-180.

6. Ciuparu, D.; Lyubovsky, M. R.; Altman, E.; Pfefferle, L. D.; Datye, *A. Catal. Rev.*, **2002**, 44, 593-649.

7. Kucharczyk, B.; Tylus, W.; Kepinski, L. *Appl. Catal. B*, **2004**, 49, 27-37.

8. Luo. T; Vohs J.M; Gorte R. J; *J. Catal.*, **2002**, 210, 397-404.

9. Luo. T; Gorte R. J.; *Catal. Lett.* **2003**, 85, 139-146.

10. O'Neill, B. J.; Jackson, D. H. K.; Lee, J. Canlas, C.; Stair, P. C.; Marshall, C. L.; Elam, J. W.; Kuech, T. F.; Dumesic, J. A.; Huber, G. W. *ACS Catal*, **2015**, 5, 1804-1825.

11. O'Neill, B. J.; Jackson, D. H. K.; Crisci, A. J.; Farberow, C. A.; Shi, F.; Alba-Rubio, A. C.; Lu, J.; Dietrich, P. J.; Gu, X.; Marshall, C. L.; Stair, P. C.; Elam, J. W.; Miller, J. T.; Ribeiro, F. H.; Voyles, P. M.; Greeley, J.; Mavrikakis, M.; Scott, S. L.; Kuech, T. F.; Dumesic, J. A. *Angewandte Chemie*, **2013**, 125, 14053-14057.

12. Lu, J.; Fu, B.; Kung, M. C.; Xiao, G.; Elam, J. W.; Kung, H. H.; Stair, P. C. *Science* **2012**, 335, 1205-1208.

13. Gould, T. D.; Izar, A.; Weimer, A. W.; Falconer, J. L.; Medlin, J. W. *ACS Catalysis*, **2014**, 8, 2714-2717.

14. Gong, Y.; Palacio, D.; Song, X.; Patel, R. L.; Liang, X.; Zhao, X.; Goodenough, J. B.; Huang, K. *Nanoletters*, **2013**, 13, 4340-4345.

15. Chen, C.; Yeh, Y.-H.; Cargnello, M.; Murray, C.B.; Fornasiero, P.; Gorte, R. J. *ACS Catal.*, **2014**, 4, 3902-09.

16. Briot, P.; Primet, M. *Appl. Catal*. **1991**, 68, 301.

17. Stakheev, A. Y.; Batkin, A. M.; Teleguina, N. S.; Bragina, G. O.; Zaikovsky, V. I.; Prosvirin, I. P.; Khudorozhkov, A. K.; Bukhtiyarov, V. I. *Topics in Catal.*, **2013,** 56, 306.

18. Muller, C. A.; Maciejewski, M.; Koeppel, R. A.; Baiker, A. *Catal. Today, 1999*, 47, 245.

19. Schwartz, W. R.; Ciuparu, D.; Pfefferle, L. D. *J. Phys. Chem. C*, **2012**, 116, 8587-8593.

20. Ciuparu, D.; Perkins, E.; Pfefferle, L. *Appl. Catal. A.*, **2004**, 263, 145-153.

21. Farrauto, R. J.; Lampert, J. K.; Hobson, M. C.; Waterman, E. M. *Appl. Catal. B*, **1995**, 6, 263-270.

22. Fujimoto, K. I.; Ribeiro, F. H.; Avalos-Borja, M.; Iglesia, E. *J. Catal.*, **1998**, 179, 431.

23. Zhu, G.; Han, Y.; Zemlyanov, D; Ribeiro, F. J. *Amer. Chem. Soc.*, **2004**, 126, 9896.

24. Skála, T; Šutara, F; Prince, K; Matolín, V; *J. Elect. Spec. Phenom.* **2009**, 169, 20-25.

25. Mi Y; Wang J; Yang Z; Wang Z; Wang H; Yang S; *RSC Adv.* **2014**, 4, 6060-6067.

26. Kuratani, K; Uemura; Mizuhata, M; Deki, S; *J. Am. Ceram. Soc.* **2005**, 88, 2923-2927

27. Hilaire, S; Wang, X; Luo, T; Gorte, R.J; Wagner, J; *Appl. Catal. A*, **2001**, 215, 271-278

28. Briot, P; Primet, M; *Appl. Catal.* **1991**, 68, 301-314.

29. Schwartz, W.R; Ciuparu, D; Pfefferle, L.D; *J. Phys. Chem. C.* **2012**, 116, 8587-8593.

30. Ciuparu, D; Perkins, E; Pfefferle L; *Appl. Catal. A.* **2004**, 263, 145-153.

31. Gong, Y; Palacio, D; Song, X; Patel, R. L; Liang, X; Zhao, X; Goodenough, J.B; Huang, K; *Nano Letters*, **2013**, 13, 4340-4345.

CHAPTER 8. CONCLUDING REMARKS AND SUMMARY

Conclusion:

Stability issues are of great concern in heterogeneous catalyst applications, where high temperature operations, exposure to poisons such as SO_2, and redox cycling can lead to severe deactivation due to loss of active surface area. The routine strategy is to introduce the catalytic components and promoters onto inert, high-surface area supports, which are less susceptible to sintering. However, as demonstrated in this thesis, the conventional introduction of these materials via aqueous salt impregnation onto the supports tend to introduce large crystallites and lead to poor mixing which lead to the inability to take advantage of any promotional effects.

As of today, there are various nanotechnology tools that have allowed materials to be designed to be in close proximity, and one of the most interesting tools is ALD. While ALD allows materials to be prepared in a hierarchically structured manner, the conventional ALD approach is largely catered to the semi-conductor industry, where materials are cycled rapidly with a carrier gas. This leads to serious issues associated with diffusion limitation of materials into the catalyst samples. In this thesis, a static ALD system was designed to address these issues so that the advantages of this layer-by-layer approach can be utilized to design catalyst.

Successful deposition of thin film of Fe_2O_3 on high-surface area γ-Al_2O_3 by our home-built static ALD system was first demonstrated in Chapter 3. Gravimetric analysis

as a function of ALD cycles, surface-area and pore-size-distribution measurements, along with TEM-EDS mapping, were consistent with formation of dense, uniform thin films on Al_2O_3. However, the relevant film thicknesses were found to be limited to 0.3 to 1.5-nm as thicker films led to a significant decrease in specific surface area presumably due to blockage to the nanopore entrances of the catalyst. The catalytic properties of the high-surface area 0.3-nm Fe_2O_3 film for the water-gas-shift reaction were then found to be different from that of bulk Fe_2O_3. The films were reducible and could be promoted to provide high activity by addition of Pd. The results in this study demonstrated that ALD, when carried out in the right approach, could be used to fabricate novel catalytic materials.

Another example successfully demonstrated in Chapter 4 was the use of ALD to prepare high-surface area CeO_2 film with excellent catalytic properties and thermal stability. While pure CeO_2 is the material of choice as promoters and catalysts in many applications, it has serious stability issues with loss of active surface area and increased crystallite size after treated to temperatures of around 1073 K. Based on TEM and XRD, thin film of CeO_2 was uniformly deposited on porous Al_2O_3 by ALD, and the composites formed in this way was used as catalyst supports for Pd. When heated to 1073 K, the supported-Pd catalysts on the ALD-modified supports exhibit better water-gas-shift and CO oxidation rates compared to those obtained on conventionally prepared catalysts, implying two facts. First, the ALD-prepared catalysts have much better thermal stability than conventional CeO_2 supports. Second, the hierarchical structuring by ALD enables excellent contact between the Pd and the CeO_2 so the promotional properties could be fully taken advantage of.

While the Pd-supported on the high-surface area CeO_2 film prepared by ALD had many excellent catalytic properties, practical applications usually demand that CeO_2 is stabilized by the addition of ZrO_2 to form ceria-zirconia solid solution, which has been shown to have better reducibility than pure CeO_2. In Chapter 5, the preparation of high-surface area $CeZrO_4$ film was successfully achieved by ALD under moderate conditions due to the precise layer-by-layer addition of Ce and Zr. This was confirmed by TEM/EDS and XRD. Conventional impregnation of Ce and Zr salt resulted in poor mixing based on the segregated phases formed as observed in the XRD patterns. When used as a support for Pd, the ALD-modified catalysts had excellent thermal stability up to 1273 K. The thermodynamic, redox properties of the CeO_2 and $CeZrO_4$ films were also investigated with $CeZrO_4$ film being more reducible and more stable to redox cycling than the CeO_2 films.

Another interesting example, where compositional control is critical, was the successful preparation of $LaFeO_3$ film by ALD as shown in Chapter 6. Coarsening of metal particles is a serious issue in high-temperature applications such as automotive-emissions control catalysis and catalytic combustion. Pd supported on $LaFeO_3$ is of interests as it is the classical example of a “smart” catalyst capable of redispersing sintered metal particles following redox cycling conditions. Unfortunately, the redispersion process does not appear to work in practice because the surface areas of the perovskite supports are too low and the diffusion lengths for the metal ions within the bulk perovskite too short. Here, we demonstrated reversible activation upon redox cycling for CH_4 oxidation and CO oxidation on Pd supported on the ALD prepared high-surface-area $LaFeO_3$ film. The $LaFeO_3$ film, less than 1.5-nm thick, was shown to be thermally stable to at least 1173 K. The activated

catalysts exhibited stable catalytic performance for methane oxidation after high-temperature treatment.

Sintering of metal particles was also found to be suppressed by overcoating with metal oxide films prepared by ALD. The thermal stability of Pd particles was greatly improved up to 1073 K after ZrO_2 thin film was deposited by ALD over the metal particles to form a semi 'core-shell' structure. An interesting observation from this work was that ZrO_2 films could grow only on pre-oxidized PdO but not on pre-reduced Pd catalyst samples. This suggests that it may be possible to deposit materials over only selected parts of the catalyst by ALD. An extension to this work was the modification of the ZrO_2 film over metal oxide supports such as CeO_2. CeO_2 loses surface areas after harsh redox cycling conditions, and surface ceria is sensitive to poisoning by SO_2. The ZrO_2 films stabilized the surface area and crystallite size of CeO_2, and they improved the sulfur tolerance of the catalysts by preventing formation of cerium sulfates.

In conclusion, ALD could be used as a major tool in preparing nanostructured catalysts with unique properties, as demonstrated in this thesis. The approach utilized in the present work differed significantly from the majority of work in that a static ALD system was used to prepare films of functional oxides that are very thin compared to the pore dimensions of high-surface-area catalysts, typically around or less than 1 nm thick. This thesis successfully achieved two primary objectives, which was to demonstrate that it was possible to use ALD to (1) prepare high-surface area films with excellent thermal stability and unique thermodynamic properties, and (b) to stabilize precious metals and metal oxides by thin films with its excellent thermal stability.